ANALYSIS AND PREDICTION OF SPACE WEATHER EVENTS AND THEIR IMPACTS ON SATELLITE COMMUNICATION SYSTEMS

ARTHUR AMARAL FERREIRA

TESE DE DOUTORADO EM ENGENHARIA ELÉTRICA
DEPARTAMENTO DE ENGENHARIA ELÉTRICA

FACULDADE DE TECNOLOGIA

UNIVERSIDADE DE BRASÍLIA

UNIVERSIDADE DE BRASÍLIA
FACULDADE DE TECNOLOGIA
DEPARTAMENTO DE ENGENHARIA ELÉTRICA

ANALYSIS AND PREDICTION OF SPACE WEATHER EVENTS AND THEIR IMPACTS ON SATELLITE COMMUNICATION SYSTEMS

ARTHUR AMARAL FERREIRA

SUPERVISOR: RENATO ALVES BORGES, DR.
CO-SUPERVISOR: CLAUDIA BORRIES, DR.

TESE DE DOUTORADO EM ENGENHARIA
ELÉTRICA

PUBLICAÇÃO: PPGEE.TD-199/23

BRASÍLIA/DF: JULHO - 2023

UNIVERSIDADE DE BRASÍLIA
FACULDADE DE TECNOLOGIA
DEPARTAMENTO DE ENGENHARIA ELÉTRICA

ANALYSIS AND PREDICTION OF SPACE WEATHER EVENTS AND THEIR IMPACTS ON SATELLITE COMMUNICATION SYSTEMS

ARTHUR AMARAL FERREIRA

TESE DE DOUTORADO SUBMETIDA AO DEPARTAMENTO DE ENGENHARIA ELÉTRICA DA FACULDADE DE TECNOLOGIA DA UNIVERSIDADE DE BRASÍLIA COMO PARTE DOS REQUISITOS NECESSÁRIOS PARA A OBTENÇÃO DO GRAU DE DOUTOR.

APROVADA POR:

Prof. Dr. Renato Alves Borges
ENE/Universidade de Brasília
Orientador

Prof. Dr. Daniel Guerreiro e Silva
ENE/Universidade de Brasília
Membro Interno

Prof. Dr. João Francisco Galera Monico
FCT/Universidade Estadual Paulista Júlio de Mesquita Filho
Membro Externo

Dr. Norbert Jakowski
WWE-SO/German Aerospace Center
Membro Externo

BRASÍLIA, 7 DE JULHO DE 2023.

FICHA CATALOGRÁFICA

FERREIRA, ARTHUR AMARAL
Analysis and prediction of space weather events and their impacts on satellite communication systems [Distrito Federal] 2023.
xix, 131p., 210 x 297 mm (ENE/FT/UnB, Doutor, Engenharia Elétrica, 2023).
Tese de Doutorado – Universidade de Brasília, Faculdade de Tecnologia.
Departamento de Engenharia Elétrica

1. Comunicação por Satélite	2. Cintilação
3. Distúrbios ionosféricos	4. Clima Espacial
I. ENE/FT/UnB	II. Título (série)

REFERÊNCIA BIBLIOGRÁFICA

FERREIRA, A. A. (2023). Analysis and prediction of space weather events and their impacts on satellite communication systems . Tese de Doutorado em Engenharia Elétrica, Publicação PPGEE.TD-199/23, Departamento de Engenharia Elétrica, Universidade de Brasília, Brasília, DF, 131p.

CESSÃO DE DIREITOS

AUTOR: Arthur Amaral Ferreira
TÍTULO: Analysis and prediction of space weather events and their impacts on satellite communication systems .
GRAU: Doutor ANO: 2023

Arthur Amaral Ferreira

Departamento de Engenharia Elétrica (ENE) - FT
Universidade de Brasília (UnB)
Campus Darcy Ribeiro
CEP 70919-970 - Brasília - DF - Brasil

To my inspiring and beloved parents.

ACKNOWLEDGMENTS

I would like to thank the German Academic Exchange Service (DAAD) for the support to conduct this work through the DLR-DAAD Research Fellowship n° 301. I acknowledge the European Commission for supporting this work through the Horizon 2020 Project 776011 TechTIDE. I also would like to thank the Brazilian agencies CAPES, CNPq and FAPDF which partially supported this work, and also the Brazilian Space Agency (AEB) and the Brazilian National Telecommunications Agency (ANATEL) for technical support.

Especially, I would like to thank Dr. Renato Alves Borges and Dr. Claudia Borries for the trust in my work and for all the guidance provided during this period. For being open to hear and to discuss ideas, and for the support and encouragement throughout this journey. The valuable advises provided during those years contributed not only for the realization of this work, but also for my development as a scientist. I also thank Dr. Claudia Paparini for the support and encouragement during this period. I thank all colleagues from the DLR-SO and the ENE-UnB for the nice moments of ideas exchange and fruitful discussions.

I would like to thank all the parties that kindly provided data used in this work: the Massachusetts Institute of Technology, who provide access to GNSS TEC data products through the Cedar Madrigal database; the ACE and WIND teams for making their data publicly available; the NASA/GSFC's SPDF OMNIWeb CDAWeb service; the Ionosphere Monitoring Prediction Center (IMPC) and the Norwegian Mapping Authority (NMA) for providing ROTI data; the Universitat Politècnica de Catalunya for providing AATR data; the European Space Agency (ESA) for providing the SWARM data; the International GNSS Service (IGS) for providing TEC data; the SWARM data the DMSP, Boston College and CEDAR Madrigal teams for providing DMSP SSJ data and the FMI for providing IE index and 2D Equivalent currents data. In addition, I would like to thank Dr. Dmytro Vasylyev for his support on the Faraday rotation and ionospheric scintillation computations and discussions, Dr. Chao Xiong for providing the S-variable derived from SWARM data; Dr. Daniel Kouba and Jens Mielich for providing ionosonde data, Leandro Ribeiro Reis for the support on the link budget computation for the AlfaCrux mission and, Dr. Claudia Borries for providing the A_{TID} *index data.*

I thank my parents and siblings for inspiring and supporting me during my entire life. I also would like to thank my wife Aline for being always there encouraging and helping me to overcome the difficult moments. Lastly, I thank my daughter Cecília, who through a simple smile brings me joy and motivation to do my best.

RESUMO

Título: Análise e predição de eventos de clima espacial e seus impactos nos sistemas comunicação por satélite
Autor: Arthur Amaral Ferreira
Orientador: Renato Alves Borges, Dr.
Coorientador: Claudia Borries, Dr.
Programa de Pós-Graduação em Engenharia Elétrica
Brasília, 7 de julho de 2023

Os eventos de clima espacial podem afetar a operação de sistemas tecnológicos modernos dos quais a humanidade depende atualmente, incluindo redes de energia elétrica, veículos espaciais, comunicação por ondas de rádio e sistemas de navegação. Portanto, qualquer nova informação que nos ajude a prever e entender melhor os fenômenos do clima espacial e seus impactos em nossa infraestrutura e serviços é do maior interesse. Nesse contexto, este manuscrito apresenta os resultados da investigação de diferentes fenômenos do clima espacial, abordando principalmente os distúrbios ionosféricos propagantes de larga escala (*Large Scale Travelling Ionospheric Disturbances, LSTIDs*), as subtempestades (avaliadas aqui por meio do índice de eletrojato auroral (*Auroral Electrojet, AE*) e os efeitos da rotação de Faraday e da cintilação na comunicação por satélite na banda UHF. Na primeira parte deste manuscrito, é realizada uma análise estatística dos LSTIDs observados em médias latitudes na região Européia durante a fase descendente do ciclo solar 24. Além disso, é apresentada uma investigação sobre os possíveis índices derivados de dados de GNSS que podem servir como precursores para a ocorrência de LSTIDs. Os resultados indicam que o índice AATR (*Along Arc TEC Rate*) e os gradientes ionosféricos são candidatos promissores que podem auxiliar o monitoramento em tempo real de tais distúrbios. Esse manuscrito também apresenta metodologias para prever as subtempestades e os LSTIDs usando dados de vento solar coletados no Ponto Lagrangiano L1. Para prever o índice AE, é proposto um modelo de rede neural artificial *feed-forward*, e os resultados sugerem que a irradiância solar pode não influenciar as estimativas. Além disso, os resultados mostraram que as informações combinadas do campo magnético interplanetário (*Interplanetary Magnetic Field, IMF*) e da velocidade do vento solar fornecem as melhores estimativas do índice AE. As informações do IMF são, no entanto, dominantes quando comparadas à velocidade do vento solar. Com relação aos LSTIDs, diferentes metodologias são investigadas visando permitir a previsão de tais distúrbios sobre a região europeia usando dados de vento solar. Nesse caso, é proposto um novo modelo que, de acordo com o melhor conhecimendo do autor, é o primeiro modelo desenvolvido para a predição do nível de atividade dos LSTIDs. A última parte deste manuscrito é dedicada à investigação dos efeitos da rotação de Faraday e da cintilação ionosférica no planejamento da missão AlfaCrux, que é uma missão educacional e de rádio amador coordenada pelo Laboratório de Simulação e Controle de Sistemas Aeroespaciais da Universidade de Brasília, Brasil. Como o Brasil está localizado em uma região com alta ocorrência de bolhas e irregularidades no plasma ionosférico, a avaliação do risco de interrupção da comunicação devido à cintilação ionosférica é essencial para o planejamento e o uso eficiente do canal de comunicação. Nesse cenário, é proposta uma nova metodologia para avaliar o risco de interrupção da comunicação com base na análise de risco da teoria da decisão. A metodologia proposta pode ser útil não apenas para a missão AlfaCrux, mas para qualquer outra missão de comunicação por satélite que opere na faixa de frequência UHF. As principais contribuições da pesquisa apresentada neste manuscrito são, portanto, o aprimoramento da compreensão desses fenômenos de clima espacial e seus respectivos impactos, e o desenvolvimento de estratégias para prevê-los.

Palavras-chave: Comunicação por Satélite, Cintilação, Distúrbios ionosféricos, Clima Espacial.

ABSTRACT

Title: Analysis and prediction of space weather events and their impacts on satellite communication systems
Author: Arthur Amaral Ferreira
Supervisor: Renato Alves Borges, Dr.
Co-Supervisor: Claudia Borries, Dr.
Graduate Program in Electrical Engineering
Brasília, July 7th, 2023

Space weather events can affect the operation of modern technological systems that humankind currently relies on, including electric power grids, spaceborne vehicles, radio wave communication, and navigation systems. Therefore, any new information that helps us to predict and better understand the space weather phenomena and their impact on our infrastructure and services is of the highest interest. Hence, this manuscript presents the results of the investigation of different space weather phenomena, addressing primarily the large scale travelling ionospheric disturbances (LSTIDs), the substorms (assessed here via the Auroral Electrojet index, AE), and the effects of Faraday rotation and scintillation on UHF satellite communication. In the first part of this manuscript, an analysis of the LSTIDs observed over mid-latitude Europe during the descending phase of solar cycle 24 is performed. In addition, an investigation on potential GNSS based indices that can serve as precursors for the occurrence of LSTIDs is presented. The results indicate that the Along Arc TEC Rate (AATR) index and ionospheric gradients are promising candidates that may support real-time monitoring of such disturbances. This manuscript also presents methodologies for predicting the substorms and the LSTIDs using solar wind data from Lagrangian Point L1. For predicting the AE index, a feed-forward artificial neural network model is proposed, and the results suggest that the solar irradiance may not influence the estimates. In addition, the results have shown that the combined information of interplanetary magnetic field (IMF) and solar wind velocity provide better estimates of the AE index. The IMF information is, however, dominant when compared to the solar wind velocity. Regarding the LSTIDs, different methodologies for their prediction over the European region using solar wind are investigated, and a new model is proposed, which, to the best of the author's knowledge, is the first model for LSTIDs activity prediction. The last part of this manuscript is devoted to investigate the effects of the Faraday Rotation and the ionospheric scintillation in the planning of the AlfaCrux mission, which is an amateur radio and educational mission coordinated by the Laboratory of Simulation and Control of Aerospace Systems of the University of Brasília, Brazil. Since Brazil is located in a region with high occurrence of ionospheric plasma bubbles and irregularities, assessing the risk of communication outage due to ionospheric scintillation is essential for planning and efficient use of the communication channel. In this framework, a new methodology for assessing the risk of communication outage based on the risk analysis from decision theory is proposed. This proposed methodology may be useful not only for the AlfaCrux mission, but for any other satellite communication mission operating in the UHF frequency band. The main contributions of the investigation presented in this manuscript are, therefore, the improvement in understanding of these SWe phenomena and their impacts and the development of strategies to predict them.

Keywords: Satellite Communication, Scintillation, Ionospheric Disturbances, Space Weather.

CONTENTS

1 Introduction ... 1

1.1 Space Weather ... 1

1.1.1 The Sun ... 2

1.1.2 The Magnetosphere-Ionosphere-Thermosphere system ... 5

1.1.3 Geomagnetic and ionospheric disturbances ... 7

1.1.4 Large Scale AGWs/TIDs ... 8

1.1.5 Ionospheric irregularities ... 11

1.2 Impact of the ionosphere on the radio communication ... 13

1.3 Objectives ... 14

1.4 Justification ... 14

1.5 Description of the manuscript ... 15

2 Analysis of LSTIDs occurrence at mid-latitudes ... 17

2.1 Analysis of the occurrence of LSTIDs from 2015 to 2019 ... 18

2.1.1 Total Electron Content (TEC) ... 18

2.1.2 LSTIDs detection ... 19

2.1.3 Geomagnetic storms detection ... 20

2.1.4 LSTIDs statistics ... 23

2.2 Identification of potential precursors for the occurrence of LSTIDs: a case study 25

2.2.1 Dataset ... 26

2.2.1.1 IMAGE equivalent currents ... 26

2.2.1.2 Swarm field-aligned currents and auroral oval boundary estimation 27

2.2.1.3 MFACE field-aligned currents ... 27

2.2.1.4 Precipitation from DMSP ... 28

2.2.1.5 Ionosonde data ... 28

2.2.2 Investigation of precursors for LSTIDs occurrence ... 29

2.2.2.1 The AATR index ... 29

2.2.2.2 Rate of TEC index ... 30

2.2.2.3 TEC gradients ... 31

2.2.3 Space weather conditions on 8th September 2017 ... 33

2.2.3.1 LSTIDs and potential precursors ... 33

2.2.3.2 Dynamics in the thermosphere-ionosphere: Relation of TEC perturbations to FAC and the auroral electrojet activity ... 37

2.2.3.3 Dynamics in the thermosphere-ionosphere: Relation of TEC perturbations to particle precipitation ... 39

2.2.4 Discussion 40
2.2.4.1 Applicability of indices as precursors for LSTID occurrence 40
2.2.4.2 Dynamics contributing to the generation of LSTIDs 42
2.2.5 Summary 45

3 Prediction of Space Weather events based on Solar Wind measurements 48
3.1 Prediction of the Auroral Electrojet Index 49
3.1.1 The AE index 49
3.1.2 The neural network model 50
3.1.3 Inspected structures 52
3.1.4 Results and discussions 53
3.2 Prediction of the LSTIDs activities at mid-latitudes 59
3.2.1 Data and methods 59
3.2.1.1 TID activity index 59
3.2.1.2 Solar wind parameters and geomagnetic indices 61
3.2.1.3 Linear regression model 63
3.2.1.4 Persistence model 65
3.2.1.5 Neural network model 65
3.2.2 Results 66
3.2.2.1 LSTID activity detection performance 66
3.2.2.2 Multi-model ensemble 69
3.2.3 Discussion 71
3.2.3.1 TID index and geophysical parameters 71
3.2.3.2 LSTIDs prediction 72
3.2.4 Summary 74

4 Impact of Space Weather events on UHF satellite communications 76
4.1 Introduction 76
4.1.1 The CubeSat standard 77
4.1.2 Mission Description 78
4.2 Faraday rotation 79
4.2.1 Variability of Faraday rotation effect 81
4.2.2 Faraday rotation for slant propagation paths 83
4.2.3 Mitigation of polarization loss factor 85
4.3 Ionospheric scintillation 86
4.4 Scintillation and communication resilience 90
4.4.1 Risk Analysis 91
4.4.2 Link Budget 92
4.4.3 Risk of communication outage associated with scintillation 96
4.4.4 Scenarios evaluation 100

4.5 Summary 102

5 Conclusions and Recommendations 104

5.1 Conclusions 104

5.2 Recommendations 106

Bibliography 106

A List of Publications 124

A.1 Journal publications 124

A.2 Conference publications 124

A.2.1 Full-length papers 124

A.2.2 Abstracts 124

B List of Geomagnetic Storms 1 126

C List of Geomagnetic Storms 2 130

LIST OF FIGURES

1.1 Schematic of the Solar-Terrestrial environment (after a sketch by Hargreaves, 1992) 2

1.2 Structure and layers of the Sun (schematic after Goossens, 2003). 3

1.3 Typical ionospheric plasma density profile (schematic after Kelley, 2009). 6

1.4 Records of SYM-H and IMF Bz for the geomagnetic storm of 26 September 2011.......... 8

1.5 Schematic representation of the physical processes involved in the AGW-TID coupling (after Kirchengast, 1996).......... 10

1.6 Rayleigh Taylor instability formation (after Kirchengast, 1996).......... 12

2.1 Distribution of the GNSS stations provided by the Madrigal database for the European sector (left); two-dimensional map of the detrended TEC over the European region (right) (Ferreira et al., 2020).......... 19

2.2 Solar Radio Flux F10.7cm and R Sunspot number for Solar cycle (SC) 22 to 24. 21

2.3 Statistics of the detected geomagnetic storms from 2015 to 2019. Left panel: Daytime and nighttime distributions. Right panel: Histogram of the strength of the storms assessed by the SYM-H index. 21

2.4 Occurrence of the detected geomagnetic storms grouped by month (left panel) and year (right panel). 22

2.5 Smoothed detrended TEC map showing an LSTID over Europe on 17 March 2015 - 14:39:30 UT. 22

2.6 Detection of LSTIDs using the 2D FFT for the 17/03/2015 storm: (a) SYM-H index, (b) Time-series of the max amplitude derived from the 2D FFT analysis (green triangles indicate the maximum amplitude of each detected disturbance), (c) Time-Latitude Plot (TLP) of the detrended TEC indicating the LSTIDs with green triangles. 24

2.7 Statistics of the LSTIDs detected via the 2D FFT transform. Left panel: Histogram of the amplitude of the detected disturbances. Right panel: Daytime and nighttime LSTIDs distribution. 24

2.8 Statistics of the LSTIDs detected via the 2D FFT transform. Left panel: Histogram of the amplitude of the detected disturbances. Right panel: Daytime and nighttime LSTIDs distribution. 25

2.9 Example maps of TEC gradients (left), ROTI (center) and AATR index (right) in three different levels: AATR ≤ 0.5 (green); $0.5 < \text{AATR} \leq 1$ (yellow); AATR > 1 (red) (Ferreira et al., 2020). 32

2.10 Space weather conditions during 8th September 2017, shown with common parameters. Top panel: solid line is geomagnetic SYM-H index. Bars indicate occurrence of solar flares. Second panel: Auroral electrojet index derived from IMAGE magnetometers (IE). Third panel: solar wind speed (SW). Fourth panel: Y and Z-components of the interplanetary magnetic field (By, Bz) in the Geocentric Solar Magnetospheric (GSM) coordinates. Last panel: Solar wind flow pressure (SWfp). The solar wind data presented herein corresponds to the 1-min averaged values and involves the Earth's bow shock nose shifted ACE and WIND data available from the NASA'S OMNIWeb data service (http://omniweb.gsfc.nasa.gov/) (Ferreira et al., 2020). 32

2.11 Time-latitude-plots centered at 15 ° E of perturbations in the Total Electron Content (TEC) from 7th Sep 2017 (18:00 UT) to 8th Sep 2017 (23:59 UT), estimated with the different methods described in Section 2.2.1. First panel: Detrended TEC mostly reflecting TID amplitudes, where I corresponds to the group of fast LSTIDs in mid-latitudes, II corresponds to the group of slow LSTIDs, III corresponds to a significant strong wave-like TEC perturbation in high latitudes, IV corresponds to a strong LSTID in mid-latitudes generated in high-latitudes around 18 UT. Second panel: AATR index. Third panel: ROTI. Fourth panel: TEC gradients. Data gaps are presented in gray color (Ferreira et al., 2020)........ 34

2.12 Illustration of the linear fitting procedure used to estimate the LSTIDs propagation parameters on 8th Sep 2017, between 12:00 and 20:00 UT. White dots indicate the points for the linear fitting of crests and troughs, and the fitting results are indicated with white dashed-lines (Ferreira et al., 2020)....... 35

2.13 Upper panel: Ionosphere Equivalent Currents (IEC), which indicate auroral electrojet activity (positive: eastward electrojet, negative: westward electrojet). Middle Panel: Field Aligned Currents (FAC), derived from MFACE model. Lower panel: S variable obtained from the Field Aligned Currents derived from Swarm constellation. Latitude coordinates correspond to the coordinates of Swarm satellites (vertical projection to the ground). Estimates of equatorward auroral oval boundaries and their geographic latitudes are indicated as black horizontal lines (Ferreira et al., 2020). 37

2.14 Selected DMSP crossings over Europe on 8th September 2017 for DMSP satellites F16A, F17A and F18A. First panel: Geographic coordinates of the satellite during the passage (vertical projection to the ground, also known as satellite ground-track). Second panel: Integrated electron/ion energy flux. Third panel: Differential electron energy flux. Fourth panel: Differential ion energy flux (Ferreira et al., 2020)........ 39

2.15 Schematic representation of Zenith and Azimuth angles. 40

2.16 Ionosonde measurements on 8th September 2017, at Juliusruh (54.6° N, 13.4° E, left panels) and Pruhonice (50.0° N, 14.6° E, right panels). Top: Critical frequency of ionospheric F2 layer (foF2) and spread F parameter FF. Bottom: Height of F2-layer $hmF2$ and equivalent slabthickness τ (Ferreira et al., 2020)........ 43
2.17 Temporal change of geomagnetic magnetic field derived from different magnetometer stations (Ferreira et al., 2020)........ 45

3.1 AL, AU, and AE index profiles during the space weather events on the 24-25 October 2011 (Ferreira & Borges, 2021). 50
3.2 Neural Network model schematic (Ferreira & Borges, 2021). 51
3.3 Correlation coefficient and RMSE for the structures described in Table 3.1 (Ferreira & Borges, 2021). 55
3.4 RMSE and correlation coefficient (R) for the structures described in Table 3.1 with temporal information added in the ANN input (Ferreira & Borges, 2021)........ 56
3.5 ANN prediction and AE reference values for the quiet geomagnetic activity period (Ferreira & Borges, 2021)........ 56
3.6 ANN prediction and AE reference values for the moderate geomagnetic activity period (Ferreira & Borges, 2021). 57
3.7 ANN prediction and AE reference values for the severe geomagnetic activity period (Ferreira & Borges, 2021)........ 58
3.8 Total Electron Content (TEC) for the SULP station observed during the geomagnetic storm of 17 March 2015: geometry free TEC for all visible GNSS satellites (left panel), TEC_{bp} along each satellite-receiver link, illustrating TID amplitude (middle panel), TID activity index for each satellite-receiver link in colors and the weighted mean in black (right panel)........ 60
3.9 TID activity index for 7 GNSS stations (as listed in the legend) during 17 March 2015. The TID activity index for each station is multiplied by 10 and the latitude integer has been added to illustrate the temporal evolution of the TID activity index at different latitudes. A mean TID activity value and its standard deviation of the preceding 26 days is illustrated with error bars for each station. The two yellow almost vertical lines of asterisks indicate the sunrise and sunset times (Borries et al., 2023)........ 62
3.10 Scatter plots of the maximum TID activity index (y-axis) of the GNSS ground station GLSV during each of the 60 storm events versus the maximum geophysical parameter (x-axis) in the 18 hours ahead of the maximum TID activity index (minimum for IMF Bz). Left: Kan-Lee electric field EKL, right: AE index (adapted from Borries et al., 2023)........ 63

3.11 Scatter plot of the maximum TID activity index of the GNSS ground station GLSV during each of the 56 storm events versus: (a) the maximum Kan-Lee electric field E_{KL} in the 18 hours ahead of the maximum TID activity index (Borries et al., 2023) (b) the maximum AE index in the 18 hours ahead of the maximum TID activity index. Outliers indicated in Figure 3.10 are not included. 64

3.12 Schematic of the MLP model for the A$_{TID}$ prediction. 66

3.13 Prediction of the TID activity index during the geomagnetic storm event registered on the 20th of November 2003 using different models described in Sections 3.2.1.3 - 3.2.1.4: a) Linear Regression Model using EKL as input, b) Linear Regression model using NN AE index as input, c) the Persistence Model and d) Neural network based model. 67

3.14 True Skill Score for the predictions based on the linear regression (LR) and persistence model (PM) for different thresholds (in parenthesis) and different prediction times. The threshold determines the criterion to determine the occurrence or not of a LSTID activity event (Borries et al., 2023). 68

3.15 (a) TSS for the different models under investigation, i.e. regression (obtained from EKL and AE), Neural Network and the Persistence models and (b) the TSS obtained from the combination of some of such models using a weighted average scheme. 69

3.16 Statistics obtained from the different models for 60 minutes prediction: True Positive Rate (left), False Positive Rate (center) and True Skill Statistic (right). 71

4.1 Schematic representation of the Faraday rotation angle θ_F (after Suresh et al., 2020). 80

4.2 Communication schematics with a CubeSat satellite (a). Under the assumption of small zenith angle θ_o of the receiver, the geometry presented in (b) can be applied for the derivation of (4.2). Here the zenith angle θ_o is constant along the communication link and it is assumed that the angle ψ is formed between the signal propagation direction and the direction of the magnetic field $\boldsymbol{B}$ (Ferreira et al., 2022). 81

4.3 Polarization loss factor at 15°S and 45°W for 2015 (left panel) and 2018 (right panel) (Ferreira et al., 2022). 82

4.4 Left panel: Faraday rotation at 12 UT for a 437 MHz signal frequency for St. Patrick's day storm (March 17, 2015), Right panel: PLF associated with the FR presented in the left panel (Ferreira et al., 2022). 83

4.5 Upper panel: locations of the ground stations BOAV, BRAS, CUIB, and SALU. The possible trajectories of the communication satellite calculated using the Keplerian elements from Table 4.1. The instantaneous position of the satellite at 01:30 UT, 7th of September 2017, is shown as the red dot. The approximated location of the geomagnetic equator is indicated by the dashed blue line. Lower panel: sky map for the BOAV station showing the distribution of Faraday rotation angle due to ionosphere. The dotted lines and the dot show possible trajectories and instantaneous position of the communication satellite as shown in the upper panel (Ferreira et al., 2022)..... 84
4.6 Schematic representation of the ionospheric scintillation............................ 86
4.7 S_4 scintillation index (left panel) and estimated signal peak-to-peak fluctuations (right panel) for the CUIB station during the year 2017 for a 437 MHz signal (Ferreira et al., 2022)... 88
4.8 Percentage of occurrence of the signal fluctuation levels for the CUIB station for different seasons of the year 2017 (Ferreira et al., 2022)......................... 89
4.9 S_4 scintillation index (left panel) and estimated signal peak-to-peak fluctuations (right panel) for the BOAV station during the year 2017 and for a 437 MHz signal (Ferreira et al., 2022). 89
4.10 Percentage of occurrence of the signal fluctuation levels for the BOAV station for different seasons of the year 2017 (Ferreira et al., 2022).................. 90
4.11 Maximum S_4 index obtained from the ISMR Query Tool for the GPS frequencies for the period between 22-24 UT on September 7, 2017. 95
4.12 Scintillation S_4 indices (a), (c) and the associated communication outage maps (b), (d) mapped to the sky plots for the BOAV and CUIB ground stations. The maps are calculated for the period of high scintillation activity over the Brazilian region on 7th of September 2017 at 01:30 UT. The sample satellite passages during one day are also shown (dashed lines) with the instantaneous position of the satellite at 01:30 UT marked by a dot (Ferreira et al., 2022).. 97
4.13 Risk of communication outage due to scintillation for the AlfaCrux mission for the cases when the ground stations establish communication without (a) and with (b) applying the mask angle of 20°. The curves are calculated for the equivalent isotropic radiated power of 1 W and the required energy-per-bit to noise spectral density ratio $(E_b/N_o)_{req} = 8.4$ dB (Ferreira et al., 2022). . 99
4.14 Evolution in time of the communication risk estimates for various values of the required threshold ratio $(E_b/N_o)_{req}$ and the power of the transmitter antenna. The calculations are performed for the night from 6th to 7th of September 2017 using the solar radio flux daytime value of 140 sfu (Ferreira et al., 2022)..101

LIST OF TABLES

1.1 Typical vertical characteristics of the ionosphere during daytime. 6
1.2 Categorization of radio systems taking into account the role of the ionosphere. 13

3.1 Structures under investigation (adapted from Ferreira and Borges, 2021, © 2021 IEEE).. 53
3.2 Statistics of the ⋆F ANN model results (adapted from Ferreira and Borges, 2021, © 2021 IEEE). 57
3.3 Description of the combined predictions using the weight average approach. .. 70

4.1 Elements of the TLE used for the orbit calculations. Some parameters such as the epoch have been adjusted to correspond to time of ionospheric conditions considered in this investigation. 85
4.2 Parameters of the link budget calculation for an elevation angle of 30°.......... 93

B.1 List of the geomagnetic storms from which the LSTIDs amplitudes are extracted (Section 2.1.4). 127

C.1 List of the geomagnetic storm events used on the statistical analysis presented in Section 3.2. 131

LIST OF ACRONYMS AND ABBREVIATIONS

AATR	Along Arc TEC Rate. 26, 29
ACE	Advanced Composition Explorer. 53
AE	Auroral Electrojet. 8, 14, 48, 49, 104
AGW	Atmospheric Gravity Waves. 8–11, 17, 71, 73
ANN	Artificial Neural Network. 48, 49, 63, 75
ARE	Average Relative Error. 55
au	astronomical unit. 2

CIR	Corotating Interaction Region. 7
CME	Coronal Mass Ejection. 3, 7

DMSP	Defense Meteorological Satellite Program. 28
Dst	Disturbance Storm Time. 7, 57

EGNOS	European Geostationary Navigation Overlay Service. 29
EHF	Extremely High Frequency. 76
EPB	Equatorial Plasma Bubble. 61, 71

FAC	Field-aligned current. 26
FMI	Finnish Meteorological Institute. 27
foF2	Critical frequency of ionospheric F2 layer. xiii, 43
FPR	False Positive Rate. 70, 73

GGS	Global Geospace Science. 53
GIC	Geomagnetically Induced Current. 26, 44
GIRO	Global Ionospheric Radio Observatory. 28
GMSK	Gaussian Minimum Shift Keying. 78
GNSS	Global Navigation Satellite Systems. 26, 59, 71
GSM	Geocentric Solar Magnetospheric. xii, 32

HF	High Frequency. 13, 26
HSS	High Speed Solar Stream. 7

ICME	Interplanetary Coronal Mass Ejection. 66
IEC	IMAGE Equivalent Current. 26

IMAGE	International Monitor for Auroral Geomagnetic Effects. 26
IMF	Interplanetary Magnetic Field. 4, 7
IMPC	Ionosphere Monitoring Prediction Center. 30
IPP	Ionospheric Pierce-Point. 31
ITU	International Telecommunications Union. 76
LEO	Low Earth Orbit. 13, 79
LSTID	Large Scale Travelling Ionospheric Disturbance. 1, 8, 9, 11, 15–17, 71–73, 75, 104, 105
LSTM	Long Short-Term Memory. 65
MFACE	Model of Field-Aligned Currents through the Empirical orthogonal function analysis. 27
MLP	Multi-Layer Perceptron. 50, 65
MSE	Mean Square Error. 51
MSTID	Medium Scale Travelling Ionospheric Disturbance. 9, 17, 71, 72
NMA	Norwegian Mapping Authority. 30
PNT	Positioning, Navigation, and Timing. 94
PPEF	Prompt Penetration Electric Fields. 35
PPP	Precise Point Positioning. 9
ReLU	Rectified Linear Unit. 65
RMSE	Root Mean Square Error. 54
ROTI	Rate of change of TEC index. 26
RT	Rayleigh-Taylor instability. 11, 12
RTK	Real-Time Kinematic. 9
SATCOM	Satellite Communication. 76, 78, 79
SBAS	Space Based Augmentation Systems. 29
SDR	Software-Defined Radio hardware. 78
SEP	Solar Energetic Particle. 7
SHF	Super High Frequency. 76
SSC	Sudden Storm Commencement. 7
SSJ	Special Sensor J. 28
SWe	Space Weather. 1, 48
SWfp	Solar wind flow pressure. xii, 32

SYM-H	Longitudinally Symmetric Disturbance Field in Horizontal Direction. 7
SZA	Solar Zenith Angle. 65

TEC	Total Electron Content. xiii, 18, 26, 59, 60, 71
TechTIDE	Warning and Mitigation Technologies for Traveling Ionospheric Disturbances Effects. 25, 26
TID	Travelling Ionospheric Disturbance. 10, 11, 60, 61, 104
TLP	Time-latitude plot. 23
TPR	True Positive Rate. 70, 73, 74
TSS	True Skill Statistic. 70, 72, 73

UHF	Ultra High Frequency. 13, 76, 77
UPC	Universitat Politécnica Catalunya. 30
URSI	International Union of Radio Science. 28

VHF	Very High Frequency. 77

1 Introduction

Investigations on the Space Weather (SWe) have significantly increased during the last decades given its impact on modern technological systems. It is defined as an area of study that will provide us with a better understanding on the complex processes, influences and effects of the Sun and other cosmic sources on interplanetary space, on the Earth's magnetosphere-ionosphere-thermosphere system, on space- and ground-based technological systems, human life and health (Bothmer & Daglis, 2007). Since the mankind has become increasingly dependent on technological systems that are impacted by the SWe, the understanding and prediction of hazards associated to it have grown in importance (T. Pulkkinen, 2007).

This chapter presents a brief introduction on the SWe subject, including information of the Sun (its main driver), solar wind, Magnetosphere-Ionosphere-Thermosphere (MIT) system, geomagnetic and ionospheric disturbances. The ionospheric disturbances presented in this chapter are the Large Scale Travelling Ionospheric Disturbance (LSTID) and ionospheric irregularities. In the sequel, the objectives of this work are presented followed by a brief description of the organization of the manuscript.

1.1 Space Weather

Although the use of the term Space Weather is considered recent, there are different similar terms registered in the literature, being used since the middle of the 1800s. Terminologies such as *solar meteorology*, *magnetic weather* and *cosmic meteorology* can be found in this period (Cade & Chan-Park, 2015), evidencing that the interest and curiosity about SWe phenomena started even before the most common terminology becomes popular in the 1990s. Therefore, what we today refer to as Space Weather started as a collection of investigations on apparently different uncorrelated events, such as solar activity, the aurora and magnetic disturbances, which were latter being linked and associated (Cade, 2013; Cade & Chan-Park, 2015).

Throughout the years, pioneering scientists have investigated these phenomena and were able to make considerable advances in understanding some connection between them, and their insights allowed the first SWe predictions to be performed. Although formerly considered pure science and curiosity, prediction and forecasting of SWe events have become critically important as more technological systems susceptible to these events are used for commerce, science, exploration and even for national security activities (Cade, 2013).

The Solar-Terrestrial environment is a very complex system, which requires interdisci-

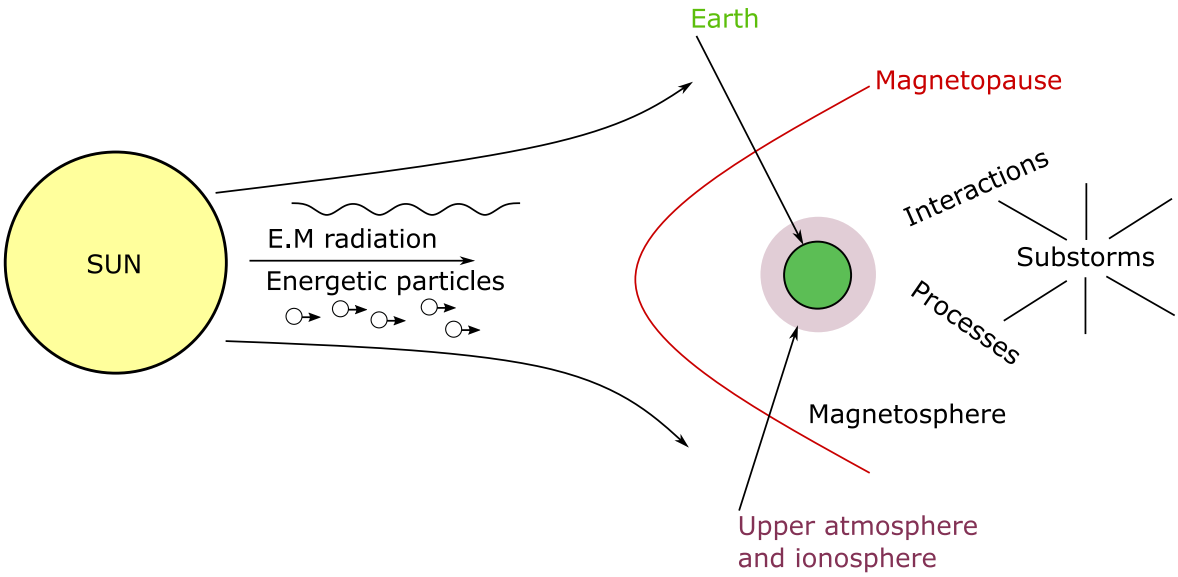

Figure 1.1 – Schematic of the Solar-Terrestrial environment (after a sketch by Hargreaves, 1992)

plinary scientific collaborations to be properly investigated. The processes in this system, ranging from magnetic field reconnection to the impact of geomagnetic storms on electrical power systems, cover different spatial and time scales (Cade, 2013). Understanding how the parts of the system interact with each other and how they behave during SWe events may be beneficial not only from the scientific point of view, but also for avoiding damages and losses. Figure 1.1 presents a simple schematic of the Solar-Terrestrial environment, illustrating the Sun (the main driver of SWe), some processes and regions affected by SWe.

1.1.1 The Sun

The Sun is located at a distance of around 1.5×10^{11} m (or 1 astronomical unit (au)) from the Earth and it is the main source of energy and energetic particles in the Solar-Terrestrial environment. It is not only the prime source of energy in our solar system, but also the main source of SWe (Bothmer & Daglis, 2007). Its radius of $\approx 6.96\times10^{8}$ m and mass of $\approx 1.989\times 10^{30}$ kg (Stix, 2002) are 109 and 3.32×10^{5} times the Earth's ones, respectively. Its main constituents are Hydrogen and Helium, with species such as Oxygen, Carbon, Nitrogen, and others accounting for less than 2% of the total constituents. Through proton-proton chain nuclear fusion reaction, hydrogen is turned into Helium, with this being the main source of energy of the Sun. The levels of the Sun's emissions received at the Earth is modulated by the solar rotation and include both electromagnetic radiation and corpuscular radiation in form of energetic particles. About $\approx 4 \times 10^{33}$ erg s^{-1} of electromagnetic radiation is emitted from the Sun (Cander, 2019). Figure 1.2 presents a schematic representation of the different layers of the Sun.

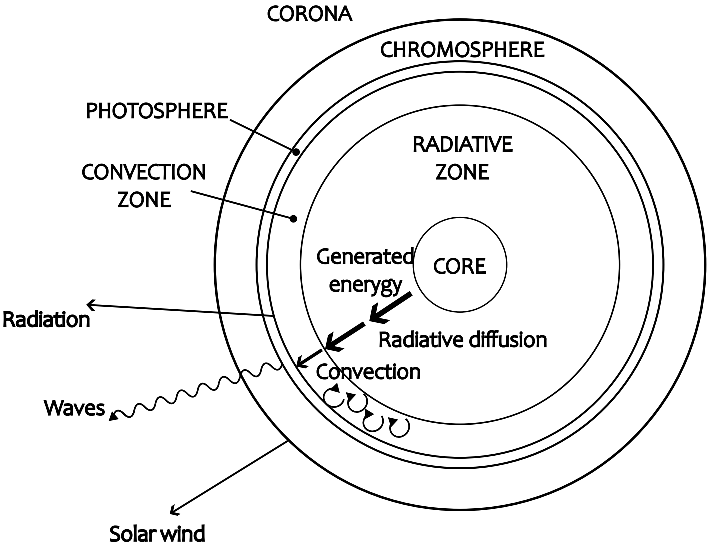

Figure 1.2 – Structure and layers of the Sun (schematic after Goossens, 2003).

The energy generated by this thermonuclear reactions in the Sun's core moves slowly outwards through the layer called radiative zone. It takes more than 170000 years for the energy radiate through this layer (ESA, 2023). In the next layer, the convection zone, the energy continues to move towards the Sun's surface though convection currents of heated and cooled gas. The next layer, known as photosphere, is considered the apparent surface of the Sun and it is one of the coolest layers, with temperatures varying from 8000 to 4500 K (ESA, 2023).

Located above the photosphere, the chromosphere is thicker than the photosphere and less dense. At this layer, unlike the lower ones, one can observe a temperature increase towards the surface rather than a decrease. A narrow transition region is located above the chromosphere. Its is around 100 km thick and it is a region in which the temperature rises abruptly, reaching up to around 100000 K. The outermost layer of the Sun is referred to as corona. This layer is the thickest and the least dense structure of the Sun. The material from this layer is then transported into the interplanetary medium by the solar wind (ESA, 2023).

Not only temperature and composition are different in each layer, but also distinct phenomena take place. Therefore, various processes and features can be observed. This features include the sunspots, prominences, Coronal Mass Ejections (CMEs) and flares. The sunspots are generated in the photosphere and correspond to dark areas observed on the Sun surface. The amount of sunspots varies with a period of approximately 11-years which is associated to the level of activity on the Sun. The prominences correspond to structure of plasma which is held up above the Sun's surface by the magnetic field lines. When the field lines holding up the plasma become unstable, a huge amount of energy can be released in form of solar flares and CMEs which correspond to of a huge amount of plasma ejected from the Sun that may reach speeds of up to 1000 km/s. This structures carry magnetic field that can interact with the Earth's magnetic field, being one of the sources of geomagnetic storms (ESA, 2023). In addition to these features, the coronal holes also play an important role. They correspond to areas of open, unipolar magnetic field lines from which high speed solar wind is streamed. The solar wind is a highly conducted plasma that is streamed radially out from the Sun at speeds about hundreds of meters per second into the interplanetary space. Due to the solar variability, such speeds can vary between 300 and 1500 km/s, even though such extremes occur relatively rarely. This streaming and expanding plasma consists mainly of protons and electrons, with a combination of around 5% Helium ions (Baumjohann & Treumann, 2012). The solar wind results from the supersonic expansion of the solar corona. The cause of such expansion is the heating of the solar corona by a not clearly specified process, which supplies such an amount of energy that a large number of particles in the solar corona can overcome the solar gravitational attraction and escape into the interplanetary space (Baumjohann & Treumann, 2012; Viall & Borovsky, 2020).

The solar wind is the medium through which larger space weather events from solar storms propagate, and therefore, understanding it is crucial for a good understanding of the space environment that surrounds the Earth (Viall & Borovsky, 2020). It reaches the Earth magnetic field at a supersonic speed, but instead of penetrating it, the solar wind is rather slowed down and mostly deflected around it (Baumjohann & Treumann, 2012). At this region, a considerable portion of the solar wind particles' kinetic energy is converted into heat/thermal energy (Baumjohann & Treumann, 2012).

Due to the considerably high conductivity of the solar wind, the solar magnetic field is *frozen* into the flowing solar wind and pulled outward by the expanding flow, gradually becoming the so called Interplanetary Magnetic Field (IMF). When the IMF has a southward directed component and encounters the northward directed terrestrial field lines at the dayside magnetopause, it allows both field lines to merge and transfer energy and momentum from the solar wind into the the geospace (Baumjohann & Treumann, 2012). This transfer of energy and momentum has long been attributed to two mechanisms: magnetic merging (Dungey, 1961) and viscous-like interaction, with merging being in general the most dominant (Lopez et al., 2012) corresponding to 100 to 30 times the efficiency of the viscous-like interaction, which has a typical efficiency of around 1.0×10^{-3} during intense northward direct IMF (Gonzales et al., 1994; Tsurutani & Gonzales, 1995).

Several advancements have been made in instrumentation, modeling and remote observations leading to an increased understanding of the solar wind and its fundamental physics. Nevertheless, there are still major outstanding questions regarding the solar wind formation and evolution (Viall & Borovsky, 2020). Investigations on such questions are, however, out of the scope of this work.

1.1.2 The Magnetosphere-Ionosphere-Thermosphere system

Among the parts of this very complex Solar-Terrestrial system, the ionosphere has attracted lots of interest from the scientific community given its impact on different technologies that rely on radio wave propagation. It can be considered as the part of the Earth's atmospheric region that presents enough amount of free electrons and ionized molecules to considerably affect the radio wave propagation. One of the main parameters used in ionospheric investigations is the electron density N_e, which corresponds to the number of free electrons per unit of volume. Its spatial and temporal distributions reveal the level of ionization of the ionosphere and such information can be adopted on the characterization of this layer (Hernández-Pajares et al., 2011).

The ionosphere extends from around 70 km up to 1000 km above sea level and in some sense it forms the interface between the Earth's atmosphere and the space (Kelley, 2009). The amount of ions and free electrons decreases above its F_2 layer (see Table 1.1), although traces of free electrons can be found at altitudes up to tens of thousands of kilometers at the plasmasphere (Hernández-Pajares et al., 2011).

The first ideas about electrified layers on the higher Earth's atmosphere date back to the 19th century, but it was the experiment conducted in 1901 by Guglielmo Marconi that attracted again interest on the subject. In this pioneer experiment, Marconi was able to transmit a radio wave signal from Cornwall in England to Newfoundland in Canada. Following this experiment, Arthur E. Kennelly and Oliver Heaviside, independently, suggested in 1902 that due to the Earth's curvature, the waves must have been reflected by an ionized layer (Hargreaves, 1992), which was then coined as *ionosphere* in 1926 by Robert Watson-Watt. Edward V. Appleton was the first to provide in the 1920s convincing evidence of its height and other properties (Brittain, 2010), which led him to to receive a Nobel Prize in 1947.

Following those pioneering investigations, several studies of the ionosphere have been conducted and most of its principal features (not all), have been understood with regard to the physical and chemical processes of the upper atmosphere (Hargreaves, 1992). One of the important results is the vertical structure of the layer, which is divided in regions (D, E, F_1 and F_2). The names for these regions have a curious history. The E-layer received its name from the electric-field in the radio-wave reflected by the *Heavyside* layer (which was the first name given to the ionosphere). The other layers were named from simply alphabetical extensions (Kelley, 2009). They have the basic daytime features described in Table 1.1 (Hargreaves, 1992).

During nighttime, the F_2 region tends to prevail at reduced N_e intensity, the D and F_1 regions vanish, and E region N_e is significantly reduced. Figure 1.3 presents the electron density distribution at the different regions for daytime and nighttime (Kelley, 2009).

The charged species that constitute the ionosphere are produced either directly by pho-

Table 1.1 – Typical vertical characteristics of the ionosphere during daytime.

Region	Height (km)	Electron density (cm^{-3})
D	60 - 90	10^2 - 10^4
E	105 - 160	10^5
F_1	160 - 180	10^5 - 10^6
F_2	max. variable around 300	several 10^6

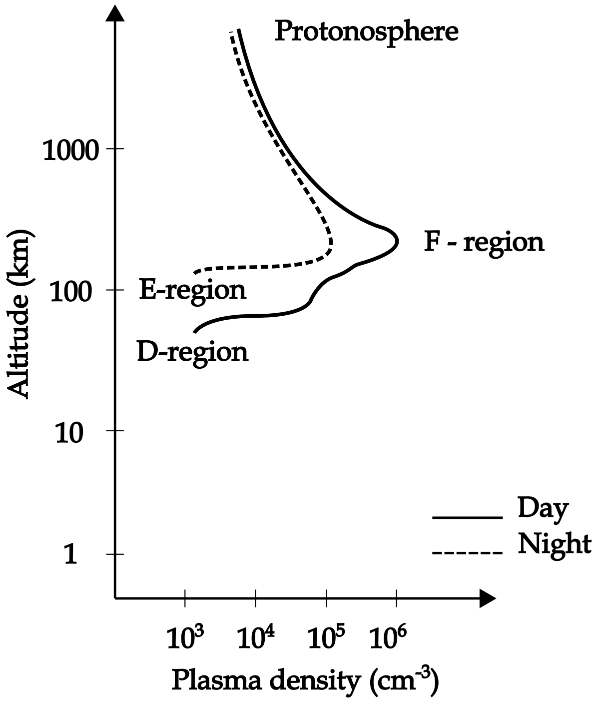

Figure 1.3 – Typical ionospheric plasma density profile (schematic after Kelley, 2009).

toionization due to the Sun UV radiation that impacts ionization of neutral atoms and molecules, or indirectly by subsequent ion-chemical reactions. Negative ions that may be formed in the region are rapidly neutralized by photodetachment and, therefore the ionic population consists of different species of positive ions, with an electron density equivalent to the sum of positive ion densities (Hargreaves, 1992). During certain geomagnetic events one can observe significant variations on the ionosphere state, such as the so called ionospheric storms which are observed in the Earth's upper atmosphere as increased/decreased electron density, total electron content, and thickness of the ionosphere (Cander, 2019). These geomagnetic events are briefly presented in the following section.

1.1.3 Geomagnetic and ionospheric disturbances

Among the phenomena observed in the Sun-Earth environment, the most significant, or geo-effective, are the CME, Solar Energetic Particle (SEP), solar X-ray flares and High Speed Solar Streams (HSSs) originated from the coronal holes and associated Corotating Interaction Region (CIR), which correspond to regions of compressed plasma and magnetic fields that occur due to the collision of HSS with a slower solar wind ahead of it (Cander, 2019; Gonzales et al., 1994). Different disturbances can be observed due to those events, such as the geomagnetic storms. These storms correspond to periods of time when an effective process of energy exchange occurs between the solar wind and the space environment around the Earth. In this case, the process is considered effective when there is a sustained period of high-speed solar wind, and more important, when the IMF is southwards (i.e. opposite to the direction of the Earth's magnetic field) when the solar wind reaches the Earth. During these periods, significant changes are observed in the currents and fields in the Earth's magnetosphere. A ring of westward current (also called *ring current*) produces magnetic disturbances on the ground, and the measurements of these disturbances have been used to quantify the magnitude of the storm by means of the Disturbance Storm Time (Dst) index and the Longitudinally Symmetric Disturbance Field in Horizontal Direction (SYM-H), which provides equivalent information of the Dst, but with a time resolution of 1 min instead of 1 hour, using different sets of stations and a slightly different coordinate system compared to Dst index (WDC KYOTO, 2009). An investigation of more than 20 years of data presented in Wanliss and Showalter (2006) has shown that the differences between both indices are lower than 10 nT for quiet times and small storms, slightly higher than 10 nT for moderate storms and usually lower than 20 nT for intense storms. These results suggest that the main difference between the 1 min SYM-H and the hourly Dst index is in the time resolution (Wanliss & Showalter, 2006).

In order to illustrate the behaviour of the SYM-H index during disturbed periods, Figure 1.4 presents the records of the SYM-H and Bz component of the interplanetary magnetic field for the geomagnetic storm of 26 September 2011. This was a strong geomagnetic storm caused by the arrival of a CME. This is an example of a geoeffective event, with long periods of negative IMF Bz component, in which the ring current was intensified and lead to a SYM-H minimum value of -116 nT. The figure also highlights the three main phases of the storm: the Sudden Storm Commencement (SSC), the storm main phase and its recovery phase.

During geomagnetic storms, one may also observe the enhancement of the so-called field-aligned currents, which correspond to currents produced in the magnetosphere that follow the magnetic field lines and are connected to intense currents in the auroral ionosphere. These currents in the auroral region, also called the auroral electrojets, produce large magnetic disturbances which are measured by chains of magnetometer stations located in high-latitudes (NOAA, 2021). One index that is derived from such measurements and that is

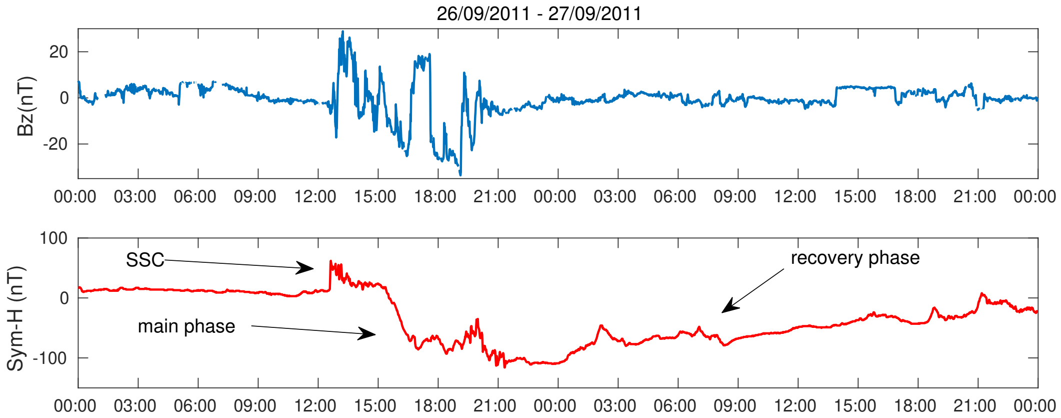

Figure 1.4 – Records of SYM-H and IMF Bz for the geomagnetic storm of 26 September 2011.

commonly used in order to evaluate the level of geomagnetic activity in the auroral region is the Auroral Electrojet (AE) index. The AE index is associated to investigations of substorms and will be presented in more details in Section 3.1.

The enhancement of currents and the precipitation of energetic particles during geoeffective events add energy in the form of momentum and heat that can modify the distribution of the density in the atmosphere (NOAA, 2021). These energy inputs can generate winds and LSTIDs, which are wave-like disturbances in the ionosphere that have been studied for decades. Their excitation mechanisms, however, are still not yet fully understood. In addition, the prediction of such disturbances are not yet well developed. The LSTIDs are under the scope of this work and are presented in more details in the following section.

1.1.4 Large Scale AGWs/TIDs

As already mentioned, during the occurrence of geomagnetic storms, one can often observe the presence of wave-like disturbances in the ionospheric electron density (N_e), which are generated at the high latitude regions and propagate towards low latitudes. These disturbances are the so-called LSTIDs and are the ionospheric signature of large scale Atmospheric Gravity Waves (AGW) in the thermosphere. These disturbances are generated by auroral sources and present horizontal velocities varying from 400 to 1000 m/s, periods in the range of 0.5 to 3 hours, and horizontal wavelengths greater than 1000 km. Their source mechanisms have been attributed to Lorentz forces and Joule heating originated from the intensification of ionospheric currents and particle precipitation (Borries et al., 2009, 2017a; Hunsucker, 1982). The source region of such disturbances is related to enhanced temporal/spatial gradients, strong uplift of the F_2 region, TEC depletion and strong aurora E layers (Borries et al., 2017a). Different techniques have been employed to investigate LSTIDs, including HF interferometry based on Digisonde measurements (Reinisch et al., 2018), incoherent scatter radar (Van der Kamp et al., 2014) and GNSS (Borries et al., 2009, 2016a; Jakowski et al., 2012), which allows to generate high-resolution 2-dimensional maps of the observed LSTIDs over continental areas (Zakharenkova et al., 2016), opening up a new opportunity to investigate LSTIDs' occurrence and evolution.

In addition to the large-scale AGWs/TIDs, one can also mention the medium-scale TIDs, which are assumed to propagate with horizontal velocities between 100 and 250 m/s, periods between 15 and 60 minutes and horizontal wavelengths of hundreds of kilometers. This type of AGW/TID is assumed to be generated due to meteorological activity in the lower atmosphere, that can reach the ionosphere heights and be detected as Medium Scale Travelling Ionospheric Disturbances (MSTIDs). Previous investigations using ray tracing of MSTIDs with a HF Doppler network, for example, have shown that this kind of disturbances might be excited by meteorological jet stream or their lower atmosphere sources (Hocke & Schlegel, 1996; Waldock & Jones, 1986). Other sources may include auroral activity (Hunsucker, 1982), tsunamis (Savastano et al., 2017), earthquakes (Calais & Minster, 1995) and flow over orography (Becker & Vadas, 2020). Investigations of the impact of MSTIDs over technological applications have shown that such disturbances can have negative effects in some precise positioning techniques, such as Real-Time Kinematic (RTK) (Hernández-Pajares et al., 2006) and Precise Point Positioning (PPP) (Poniatowski & Nykiel, 2020). Investigations in the low latitude regions have suggested that MSTIDs may also be one of the seeding mechanism for plasma bubbles in post-sunset hours in low latitudes (Chou et al., 2020; Eastes et al., 2019; Takahashi et al., 2018). This type of AGW/TID is, however, out of the scope of this work.

Investigations on the relation between AGWs and TIDs have been conducted by various researchers, since the paper of Hines (1960), which suggested this relationship. Following this suggestion different attempts to retrieve neutral gas properties from ionosphere measurements have been made. Two different approaches have been used in this case. In the first one, the hydrodynamic equations for the neutral and ion gases are coupled and solved together. This originates from the fact that there is a collisional interaction between neutrals and ions. Another frequently used approach considers the ionosphere as a passive tracer of the neutral gas with no feedback to the thermosphere. In this case, the hydrodynamic equations are solved alone, but including dissipation effects (e.g. ion drag, thermal conduction and viscosity, Hocke & Schlegel, 1996). The obtained gravity wave perturbations are then used as an input for the electron continuity equation that presents ion transport velocity formulated in terms of momentum equation, allowing to obtain the gravity-wave disturbances in the ion gas (Hocke & Schlegel, 1996; Kirchengast, 1996). Qualitatively, these relations are considered fairly well understood, in particular for the TIDs observed in the electron density. Figure 1.5 shows a schematic representation of such relation and the processes involved. When analysed bottom to top, the figure shows the natural embedding of AGW-TID relationship (bottom level) as a thermosphere-ionosphere coupling phenomenon (middle level) in the upper atmosphere (top level).

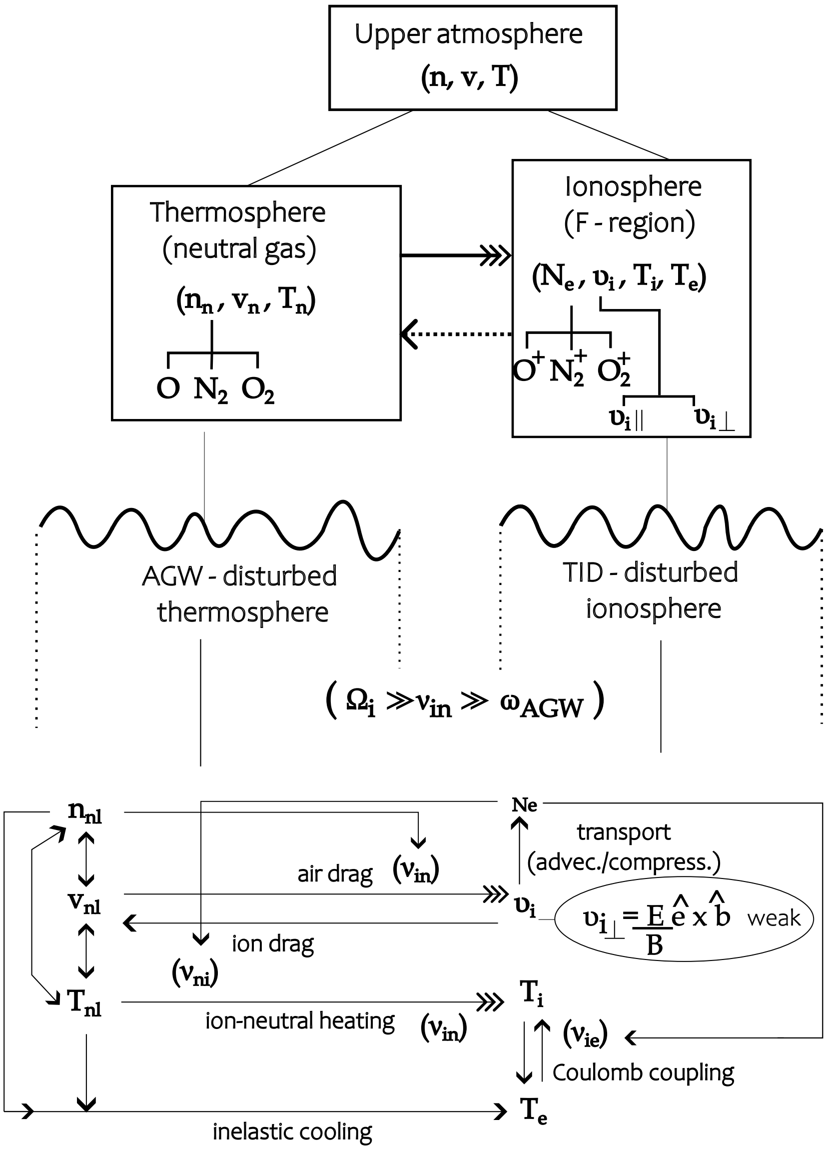

Figure 1.5 – Schematic representation of the physical processes involved in the AGW-TID coupling (after Kirchengast, 1996)

In the representation of Figure 1.5, the AGW can be described as a set of linearly perturbed neutral parameters, i.e. neutral number density (n$_{nl}$), neutral wind (v$_{nl}$) and neutral temperature (T$_{nl}$) and the Travelling Ionospheric Disturbance (TID) as a non-linear disturbance in the electron density (N_e), magnetic field-aligned ion drift (v$_{i\|}$), ion temperature (T$_i$) and electron temperature (T$_e$). The way the involved processes occur is dictated by the ratio between the relevant characteristic frequencies, namely the gyrofrequencies of ions and electrons (Ω_i), the collision frequency of the ions with the neutral gas (υ_{in}) and neutral gas with ions (υ_{ni}), the ion-electron collision frequency (υ_{ie} and the frequency of the AGW/TID disturbance itself, ω_{AGW}, Kirchengast, 1996; Kirchengast et al., 1996).

According to the theory proposed by Kirchengast et al. (1996), the generation mechanism for the perturbations in the electron density at the F-region N_e due to AGWs may be explained as follows. For AGWs at F-region heights, the dynamics of the AGW action onto the ionosphere is governed by the relation $\Omega_{i,e} \gg v_{in} \gg \omega_{AWG}$. The AGW wind perturbation (v_{nl}) drags the ionospheric plasma along the magnetic field line almost instantaneous in phase with the AGW. This induces a magnetic field-aligned ion drift ($\mathrm{v}_{i\|}$) together with strong field-aligned gradients in the electron density (except at the F_2-peak), which leads to a periodic plasma advection. In addition, at the same time, the v_{nl} produces, due its wave nature, amplitude variations along the field line leading to periodic plasma compression. Above the F_2 peak, however the action of v_{nl} is not the primary mechanism due to the increased effect of plasma diffusion above these altitudes (Kirchengast et al., 1996). At lower F-region, chemical loss processes are responsible for significantly limiting the N_e-TID amplitude.

Although a significant number of studies on the TIDs have been performed during the last decades, real-time monitoring activities and prediction of these disturbances still have room for improvement. The next chapter presents some results on the identification of precursors for the occurrence of LSTIDs and prediction of LSTIDs activities based on solar wind data, aiming at contributing to this research field.

1.1.5 Ionospheric irregularities

Ionospheric irregularities correspond to inhomogeneities in the ionospheric plasma that can have different spatial and temporal scales. Distinct types of irregularities have been investigated throughout the years, including plasma bubbles (regions with plasma depletions), irregularities associated with spread-F observed in ionosonde measurements, plumes observed in radars and irregularities responsible for fluctuations on the amplitude and phase of transionospheric signals (i.e. ionospheric scintillation, Kelley, 2009).

It is assumed that triggering mechanism together with favorable plasma conditions can lead to the development of such instabilities until they become detectable. In the case of the irregularities observed in the F layer ionosphere at low latitudes regions, the Rayleigh-Taylor instability (RT) is considered the main driving mechanism. Figure 1.6 illustrates this process.

In this scenario, two fluids with different densities n are under the effect of the gravity (g) with the lower dense fluid (n_2) sustaining the denser one (n_1). Therefore, a density gradient (anti-parallel to the gravity vector g) is generated in the lower part of the E-layer. One of the seeding mechanisms are the TIDs (Takahashi et al., 2018), that can lift the ionosphere and contribute to the RT and as a consequence the generation of irregularities. Assuming that a seeding mechanism generates a sinusoidal perturbation, the velocity of the charged particles will be proportional to collision frequency with the neutral particles. Hence, as a result there will be a predominance of ions in the $\mathrm{g} \times \mathbf{B}$ direction, driving a current $\mathbf{J_x}$ to east (or west)

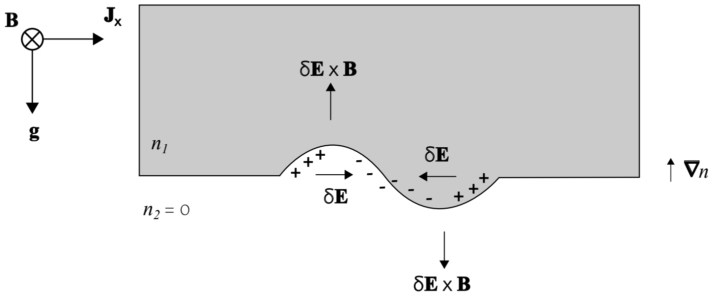

Figure 1.6 – Rayleigh Taylor instability formation (after Kirchengast, 1996)

given by:

$$\mathbf{J_x} = \frac{nm\mathbf{g} \times \mathbf{B}}{B^2} \tag{1.1}$$

Positive and negative charges will be accumulated at the extremities of the sinusoidal perturbation, leading to a non divergence-free condition. Polarization electric fields $\delta\mathbf{E}$ are generated in order to restore the divergence free condition $\nabla.\mathbf{J} = 0$. The electric fields $\delta\mathbf{E}$ generate a plasma drift $\delta\mathbf{E} \times \mathbf{B}$. Depletion regions are created with the lower density region moving up and the higher density region moving down, leading to an amplification of the initial perturbation and an unstable system (Kelley, 2009).

A similar condition can occur in the F-layer, which can be intensified during the peak of the pre-reversal enhancement (PRE). The PRE corresponds to an enhancement of the $\mathbf{E} \times \mathbf{B}$ vertical plasma drift due to the eastward electric field at the evening terminator at the magnetic equator. The magnitude of this electric field peaks before it is reversed to the westward direction in the post-sunset hours (Ghosh et al., 2020). During these periods, the E layer is affected by the recombination process and there is a strong upwards $\mathbf{E} \times \mathbf{B}$ plasma drift in the F region, leading to the generation of strong ∇n gradients in the bottom of the F layer. When the F layer is high enough, and/or the density gradient is strong enough, density fluctuations develop with $\delta\mathbf{E} \times \mathbf{B}$ drift due to the RT instability. At these periods, the plasma bubbles can develop to higher altitudes, following the local plasma in the eastward direction. The plasma bubbles are, therefore, a nighttime phenomena in which the irregularities start to cease after mid-night (local time). It is important to mention that the gravity and density gradient are not the only reasons for generating irregularities in the F layer ionosphere. The generalised instability theory of RT also considers the action of the zonal electric field and neutral winds. In addition, considerations related to the conductivity are commonly incorporated into the generalised RT instability theory (Prol, 2019).

Table 1.2 – Categorization of radio systems taking into account the role of the ionosphere.

Category 1 (ionosphere is considered part of the system)	Category 2 (ionosphere is considered a nuisance)
VLF-LF Communication and Navigation	Satellite Communication
MF Communication	Satellite Navigation (GNSS)
HF Communication	Space-based Radar and Imaging
HF Broadcasting ("shortwave listening")	Terrestrial Radar Surveillance and Tracking

1.2 Impact of the ionosphere on the radio communication

Radio based communication and broadcasting systems can be either controlled by the ionosphere, such as High Frequency (HF) skywave systems, or be impacted by it through the modification of the transmitted signal (e.g. transionospheric radio communication and navigation systems). In the first category, the ionosphere is part of the system and for the second it is a nuisance. For both cases, however, accounting for the ionospheric impact is a beneficial task for the planning and systems design activities. Table 1.2 presents some examples of systems that can be classified in the aforementioned categories (Goodman, 2005).

As shown in Table 1.2, the propagation through the ionosphere is a serious concern for satellite communication and navigation systems. The highest impact is at the resonance or critical frequency separating HF impact on terrestrial radio systems and higher frequencies for transionospheric propagation. Satellite communication systems operating at UHF band may be strongly affected by the ionosphere. One can take as example the event reported by Kelly et al. (2014) in which ionospheric irregularities contributed to a communication outage that jeopardized a military crew during a tactical operation mission. Also, nowadays different Low Earth Orbit (LEO) nanosatellite mission have been deployed and several of them operate in the UHF band. One example of such mission is the AlfaCrux mission developed by the Laboratory of Simulation and Control of Aerospace Systems (LODESTAR) of the University of Brasília. This mission is an amateur radio and educational mission with in-orbit technological demonstration and high-level tasks, which include planning, management, and risk analysis along of its life cycle (Borges et al., 2022). Since ionosphere specification and short-term forecasting are essential for Earth-space paths (Cander, 2019), investigations on the impact of the ionosphere for the mission have been conducted in this work. For this purpose, two ionospheric impacts are considered: the Faraday Rotation and ionospheric scintillation. The former corresponds to a rotation of the polarization plane of linearly polarized radio-waves due to its interaction with the ionosphere and the later refers to the fluctuations of the amplitude of the radio wave signal due to the occurrence of irregularities on the ionospheric plasma. The results of this investigation are presented in Chapter 4.

1.3 Objectives

This work aims at contributing to a better understanding of thermosphere-ionosphere perturbation events and their characteristics. This study investigates distinct SWe phenomena and analyze different strategies to predict them. The SWe events investigated herein are: geomagnetic substorms (assessed here by means of the AE index), the Large Scale Traveling Ionospheric Disturbances excited during geomagnetic events and the ionospheric scintillation at low latitude regions.

1.4 Justification

Since SWe events may impact different technological systems, monitoring and forecasting those space weather disturbances are activities that have become increasingly important. The substorms, which correspond to an injection of energy into the high-latitude ionosphere due to the reconnection of previously stored flux tubes in the magnetotail, lead to an enhanced current flow in the auroral electrojets (Baumjohann & Treumann, 2012). Since the indices used to monitor them are usually derived from magnetometers on the ground (e.g. Auroral Electrojet index, AE; IMAGE Electrojet index, IE), having the possibility to predict their behaviour based on Solar Wind measurements can be useful for estimating the level of energy input into the Magnetosphere-Ionosphere-Thermosphere system. Given the relation of the IMF and Solar Wind with the energy input into the MIT system, one could use this information to predict the amplitude of the electrojets in the auroral region. This task may be challenging due to mechanisms such as the loading-unloading processes, in which the energy from the solar wind is first stored in the magnetotail for an arbitrary period of time and later deposited in the ionosphere. In addition, changes in the configuration of the IMF and Solar Wind on the way from the measurement point (e.g. Lagrangian point L1) to the Earth may also compromise the estimates. Despite the challenges involved, predicting the AE index from such measurements can still be a helpful tool for predicting substorms. In order to contribute to this research field, this work investigates the capabilities of Artificial Neural Networks on accomplishing this task. Such predictions of the AE index can be also useful in monitoring the magnitude of other related phenomena, such as LSTIDs, given the correlation of their amplitude with the AE index.

For decades different studies have been performed in an attempt to explain the LSTIDs characteristics, but the mechanisms generating LSTIDs are still not fully understood. In order to contribute to a better understanding and characteristics of this phenomenon over the European region, this work presents an analysis of the LSTIDs that occurred in the descending phase of SC 24. In addition, investigations on the driving mechanisms and on the potential precursors for the LSTIDs excited during a case study in September 2017 are also presented. Although different techniques and indices to monitor such disturbances have been already proposed, a methodology that allows their prediction is not yet established. This kind of predictions are challenging due to the different complex interactions between the solar wind, MIT system and lower atmosphere. In this context, this investigation also presents different methodologies for predicting the level of LSTIDs activity excited during geomagnetic storms. The proposed models are based on linear regression methods, artificial neural networks and multi-model ensembles. Such methodologies are developed based on the TID activity index (A_{TID}) proposed by Borries et al. (2023) and the main goal is to use solar wind measurements derived from Lagrangian Point L1 to predict the level of LSTIDs activities over mid-latitude Europe.

In addition, this work investigates the ionospheric impact (due to Faraday rotation and ionospheric scintillation) on UHF satellite communication systems taking as a case study the AlfaCrux satellite mission. For the frequency of 437 MHz used in the AlfaCrux mission, one can expect a significant influence of the ionosphere, which can lead to deleterious impacts on the communication activity, including disruptions of the service. It is, therefore, desirable to have a metric that allows to assess the probability of success on the communication activities during post-sunset hours in equatorial regions, when the severe fluctuations in the signal power due to scintillation may occur. Due to the lack of real measurements on the 437 MHz over the Brazilian region, a climatological model has been used to obtain estimates of the ionospheric scintillation level. Then, a new methodology for assessing the risk of communication outage due to ionospheric scintillation is proposed, which might be useful not only for the AlfaCrux mission but also for any other UHF satellite missions aiming at operating in regions under strong ionospheric scintillation activity.

1.5 Description of the manuscript

The next chapters of this manuscript are organized as follows: Chapter 2 presents the results on the investigations of the LSTIDs over Europe. It includes an analysis of the LSTIDs generated during the geomagnetic storms observed from 2015 to 2019; the ionosphere-thermosphere dynamics that contribute to the LSTIDs generation during the September 2017 geomagnetic storm, together with an analyses of potential precursors for the LSTIDs occurrence. Chapter 3 presents the results of the prediction of SWe events based on solar wind measurements. The space weather events analysed here are the substorms (assessed by means of the Auroral Electrojet index) and the LSTIDs observed over mid-latitude Europe. Chapter 4 presents the studies of Faraday Rotation and scintillation impacts on UHF satellite communications with the goal of supporting the AlfaCrux mission planning and others UHF satellite missions. In this case, a new methodology to estimate the risk of communication outage due to ionospheric scintillation is proposed. The conclusions of the investigations conducted in this manuscript are presented in Chapter 5.

2 Analysis of LSTIDs Occurrence At Mid-latitudes

Parts of this chapter have been published as: Ferreira, A. A.; Borries, C.; Xiong, C.; Borges, R. A.; Mielich, J.; Kouba, D., Identification of potential precursors for the occurrence of Large-Scale Traveling Ionospheric Disturbances in a case study during September 2017. **Journal of Space Weather and Space Climate, v. 10, p. 1/10-17, 2020***, which is published under the terms of the Creative Commons Attribution License CC BY 4.0 (https://creativecommons.org/licenses/by/4.0)*

Geomagnetic storms and their associated effects have been investigated for decades not only to better understand the phenomena, but also to measure their impact on human technologies (Gonzales et al., 1994). These storms are closely related to ionospheric perturbations, such as significant enhancements of the ionospheric electrojets, positive or negative deviations of electron densities from quiet conditions, high-latitude irregularities and other effects (Borries et al., 2015; Cherniak & Zakharenkova, 2015; Prölss, 2006). One frequently observed phenomenon during geomagnetic storms are the LSTIDs. These are wave-like structures propagating through the ionosphere and are the ionospheric signature of Atmospheric Gravity Waves (AGWs). Often, intensive thermosphere heating in the auroral zones is considered to generate AGWs which propagate equatorward (e.g., Paznukhov et al., 2009; Prölss, 2006). LSTIDs propagate with horizontal velocities between 400 and 1000 m/s, horizontal wavelengths greater than 1000 km and periods in the range of 30 min to 3 hours (Hocke & Schlegel, 1996; Hunsucker, 1982). Another type of TIDs are the MSTIDs, which propagate with velocities between 100 and 250 m/s, periods in the range of 10 min to 1 hour and wavelengths between 100 and 1000 km (Chum & Podolská, 2018; Hunsucker, 1982; Shiokawa et al., 2009). Mid-latitude MSTIDs are considered to be excited by diverse mechanisms (see Chen et al., 2019; Kelley, 2011; Kotake et al., 2006, 2007; Otsuka et al., 2013) and are out of the scope of this work (Ferreira et al., 2020)[1].

Several studies have been performed during the last decades in an attempt to explain the LSTIDs characteristics (Bowman & Mortimer, 2011; Habarulema et al., 2016; Shimeis et al., 2015), but the mechanisms generating LSTIDs are still not fully understood. Great importance is given to Joule heating in the auroral region. Auroral electrojet activity is repeatedly discussed in relation to LSTID generation (Borries et al., 2017a; Wilder et al., 2012;

---

[1] Sections 2.1.1, 2.1.2, 2.2 (and its subsections) have been reprinted from Ferreira et al. (2020): Ferreira, A. A.; Borries, C.; Xiong, C.; Borges, R. A.; Mielich, J.; Kouba, D., Identification of potential precursors for the occurrence of Large-Scale Traveling Ionospheric Disturbances in a case study during September 2017. *Journal of Space Weather and Space Climate, v. 10, p. 1/10-17, 2020*, which is published under the terms of the Creative Commons Attribution License CC BY 4.0.

Zakharenkova et al., 2016). The correlation of the LSTID amplitude with the Auroral Electrojet index (AE) has been shown in Borries et al. (2009), reaching a correlation coefficient of 0.8 (95% significant) during solar maximum period.

In this context, the study presented in this chapter aims to contribute to the understanding of the processes involved on the LSTIDs generation and to the prediction activities related to this phenomenon. This investigation is subdivided in two parts: Section 2.1 is devoted to analyze the occurrence of geomagnetic storms and LSTIDs over the European sector during the descending phase of the solar cycle 24. Section 2.2 presents an investigation of potential precursors for the occurrence of LSTIDs during a case study in 7-8th September 2017, together with a discussion of the ionosphere-thermosphere dynamics related to the excitation of the observed LSTIDs.

2.1 Analysis of the occurrence of LSTIDs from 2015 to 2019

This section presents the results on the analysis of the LSTIDs excited over the European sector during geomagnetic storms. The analysis conducted herein is based on TEC data provided by the MIT Haystack Observatory, available at the CEDAR Madrigal database[2]. This database provides slant TEC data starting on the 1st of January 2015. Due to this fact, this investigation extends from the 1st of January 2015 until December 2019, which coincides with the declining phase of solar cycle 24. Although the period of data availability is not considerably large, the amount of detected geomagnetic events can help to improve our understanding of this phenomena occurrence. For the European region, this database comprises data from more than 800 stations. The distribution of the GNSS stations is illustrated in Figure 2.1 (left panel). Although a higher concentration of stations is observed in the Scandinavian region, the distribution of mid-latitude stations is considered sufficient for the purpose of this work.

2.1.1 Total Electron Content (TEC)

TEC is a parameter widely used in the studies of the near-Earth plasma environment and it provides, along with its derived products, useful information on the ionospheric behavior during geomagnetic storms (Mendillo, 2006). It is given in TEC units (TECU), with 1 TECU corresponding to 10^{16} electrons/m^2 and it is defined as the integral of the electron density N_e along the line of sight between the satellite and the receiver (Ciraolo et al., 2007; Mendillo, 2006). It can be obtained from GNSS dual-frequency measurements by combining carrier-

---

[2] http://cedar.openmadrigal.org/

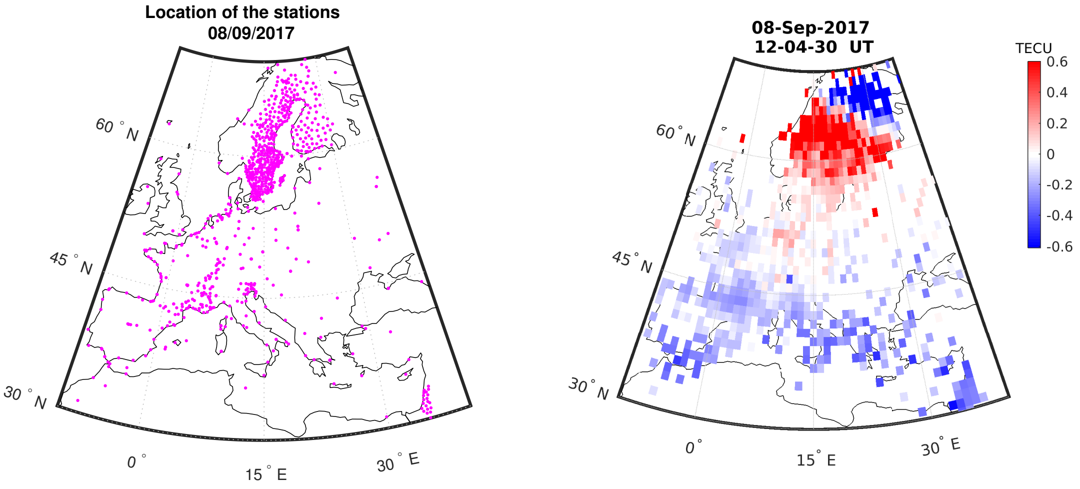

Figure 2.1 – Distribution of the GNSS stations provided by the Madrigal database for the European sector (left); two-dimensional map of the detrended TEC over the European region (right) (Ferreira et al., 2020).

phase/code pseudoranges on two frequencies as presented in Equations (2.1) and (2.2)

$$TEC = \frac{f_1^2 f_2^2}{40.3(f_1^2 - f_2^2)}[(\Phi_1 - \Phi_2) + B_{amb} + \varepsilon_{\Phi_1 - \Phi_2}], \tag{2.1}$$

$$TEC = \frac{f_1^2 f_2^2}{40.3(f_1^2 - f_2^2)}[(\Psi_2 - \Psi_1) + \varepsilon_{\Psi_2 - \Psi_1}] \tag{2.2}$$

where Φ and Ψ are the carrier-phase and code pseudoranges, respectively. Their subscripts refer to the signals measured on frequencies f_1 and f_2, B_{amb} is the carrier-phase ambiguity, $\varepsilon_{\Phi_1 - \Phi_2}$ and $\varepsilon_{\Psi_2 - \Psi_1}$ correspond to noises (e.g. thermal noise). For simplicity, other terms such as inter-frequency biases and multipath effects (Hoque & Jakowski, 2012) are not included here.

2.1.2 LSTIDs detection

In order to detect the LSTIDs, the slant TEC ($sTEC$) is first converted into a vertical expression $vTEC$ and the vTEC trend is removed afterwards. The $sTEC$ at an elevation angle ϵ is converted into an equivalent vertical TEC value according to Equation (2.3), as described in Jakowski (1996).

$$vTEC = M(\epsilon) sTEC, \tag{2.3}$$

where $M(\epsilon)$ is the slant factor that projects the slant to vertical TEC in a thin-shell model of the ionosphere and it is given by

$$M(\epsilon) = \sqrt{1 - \left(\frac{R_e \cos \epsilon}{R_e + h_i}\right)^2}. \tag{2.4}$$

The geo-reference of the resulting $vTEC$ is the piercing point of the ray path in the ionosphere approximated as a thin-layer at the height h_i = 350 km. R_e = 6,378 km is the Earth radius. The accuracy of this mapping procedure is affected by the elevation angle, in such a way that it decreases with decreasing elevation (Borries et al., 2009). Therefore, a cut-off elevation angle of 30° was chosen in order to reduce this mapping error. For the detrending of $vTEC$, an one-hour moving average window centered at time instant t ($\overline{vTEC}(t \pm 30min)$) is applied, as follows (Borries et al., 2009; Figueiredo et al., 2017; Tsugawa et al., 2004):

$$dTEC(t) = vTEC(t) - \overline{vTEC}(t \pm 30min). \tag{2.5}$$

This is done for all receiver-satellite links within a 1-minute interval. As pointed out in S. Zhang, Coster, et al. (2019) different lengths of sliding windows for TEC detrending can facilitate the detection of perturbations with different spatial and temporal scales. Previous studies indicated that the 1 hour window provides a good detection of disturbances in the temporal range of LSTIDs (Borries et al., 2009; Cherniak & Zakharenkova, 2015; Tsugawa et al., 2004). Therefore, in this study an one-hour sliding window is applied to detect the disturbances. Nevertheless, it is important to highlight that LSTIDs perturbations with longer periods ($>$ 1 hour) can still be detected, but with reduced amplitudes.

The detrended TEC is then mapped into a grid of 1° latitude x 1° longitude to enable a 2D visualization of the ionospheric disturbance. An example map of the detrended TEC over Europe is shown in Figure 2.1 (right panel).

2.1.3 Geomagnetic storms detection

The Solar Cycle 24 was rather unusual when compared to its predecessors SCs 22 and 23. As presented in Figure 2.2, SC 24 was a quite weak cycle, preceded by a long and quiet solar minimum with the lowest F10.7 index recorded (Basu, 2013). Although weak, several geomagnetic storms events have been registered during the period. Based on records of the SYM-H values retrieved from the NASA'S OMNIWeb data service, several geomagnetic storms events have been detected, and each event was inspected in order to confirm or not the occurrence of LSTIDs.

In order to identify the occurrence of geomagnetic storm, indices such as the Disturbance Storm Time (Dst) and SYM-H indices are commonly used. The purpose of both indices is the

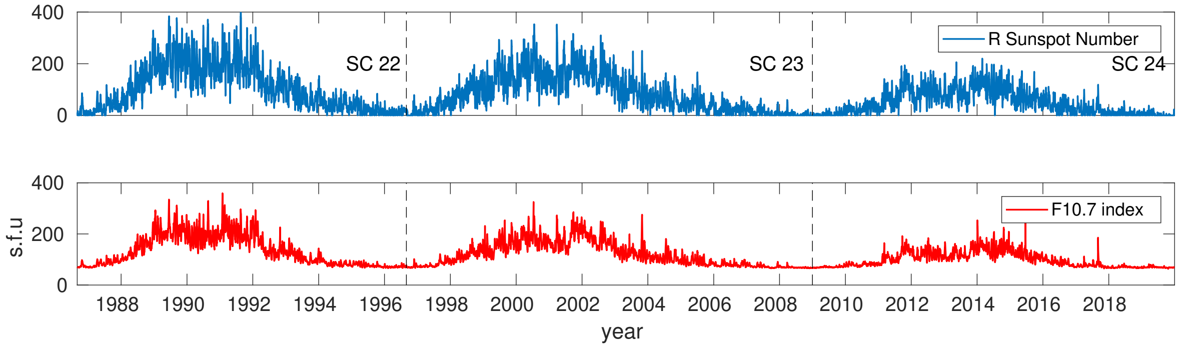

Figure 2.2 – Solar Radio Flux F10.7cm and R Sunspot number for Solar cycle (SC) 22 to 24.

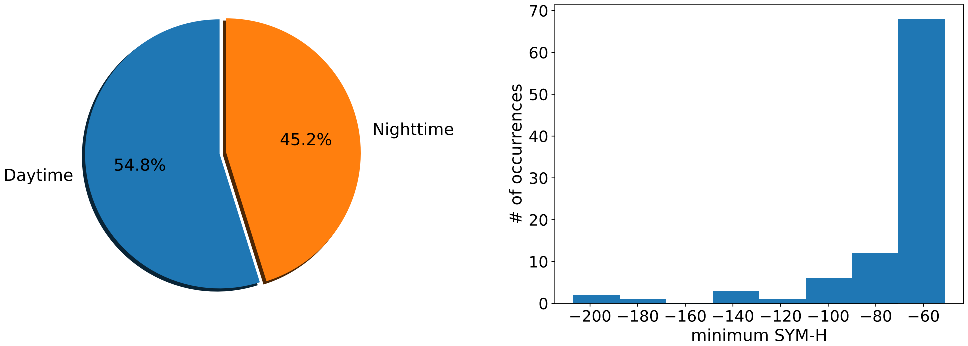

Figure 2.3 – Statistics of the detected geomagnetic storms from 2015 to 2019. Left panel: Daytime and nighttime distributions. Right panel: Histogram of the strength of the storms assessed by the SYM-H index.

same and they differ on time resolution. Whereas the former is provided in 1 hour intervals, the later has a resolution of 1 minute. Both indices measure the ring current magnetic field and thus its energy (Baumjohann & Treumann, 2012). In this investigation the SYM-H is used to detect the geomagnetic storms based on the procedure described in Borries et al. (2015). A threshold of Dst < -50 nT is commonly used for storms detection, therefore the same threshold was applied on the SYM-H values. Time intervals where the SYM-H is below the threshold are inspected and the minimum value of SYM-H in each one of the intervals is identified. The storm onset is then estimated as the time instant when the SYM-H reached the maximum value in the 12 hours prior to the minimum SYM-H. Based on this criteria, 93 geomagnetic storm events have been identified and their statistics are presented in Figures 2.3 and 2.4.

From Figure 2.3 one can observe a balanced distribution of daytime and nighttime geomagnetic storms. Also, this figure shows that the majority (88%) of the storms are classified as moderate (i.e. -100 nT < SYM-H < -50 nT, Gonzales et al., 1994) and the minority (12%) are considered intense. Figure 2.4 shows how the geomagnetic storms present a monthly and annual variability. Based on this information, one can note that the events occur mostly during equinoxes. Also, the farther from the solar maximum, the smaller the number of

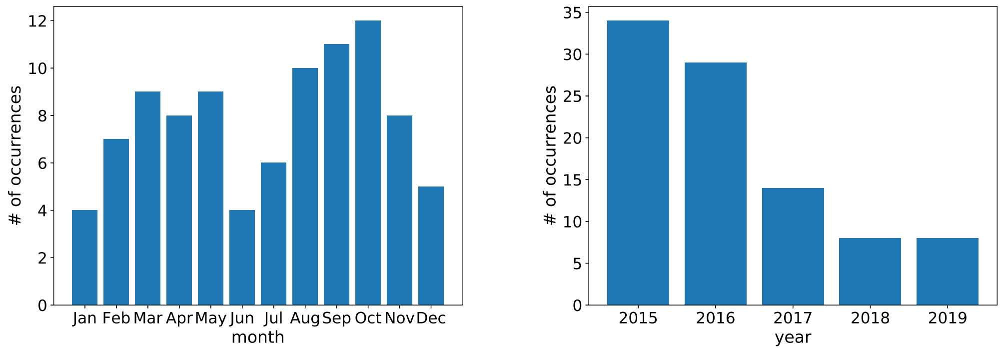

Figure 2.4 – Occurrence of the detected geomagnetic storms grouped by month (left panel) and year (right panel).

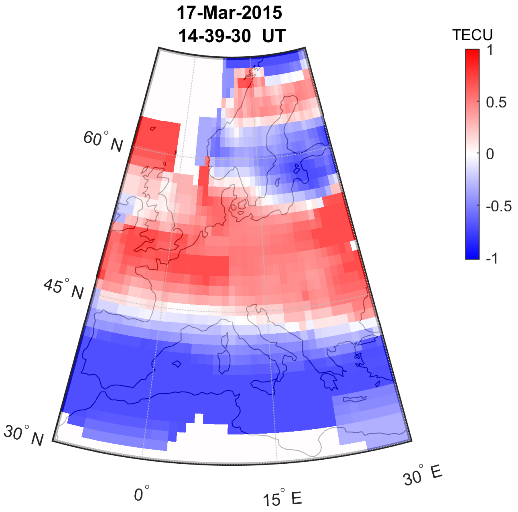

Figure 2.5 – Smoothed detrended TEC map showing an LSTID over Europe on 17 March 2015 - 14:39:30 UT.

observed storms.

Following the analysis of the geomagnetic storms observed between 2015 and 2019, the LSTIDs excited during the detected storms were investigated. The method used to detrend the GNSS derived TEC and generate detrended TEC maps is the one presented in Section 2.1.2. For each geomagnetic storm event, the detrending method was applied and a sequence of detrended TEC maps (similar to Figure 2.5) was obtained with 1-minute time resolution. Some of statistics of the detected LSTIDs are presented in the next section and a list of events from which the LSTIDs information was extracted is presented on the Appendix B.

2.1.4 LSTIDs statistics

In order to automatically retrieve the LSTIDs information, two-dimensional Fourier analysis for each detrended TEC map generated during the storm was employed. This method allows to retrieve the amplitude, wavelength and direction of propagation of the wave-like disturbances (Borries et al., 2009). The focus of this investigation is, however, only the amplitudes.

The procedure to automatic detect the LSTIDs and retrieve their amplitudes is briefly described below:

(a) First, in order to compensate for data scarsity on the detrended TEC maps, the detrended TEC value in each point of the map is temporally smoothed with a moving average of 10 minutes. Then each map is spatially smoothed with a moving average within an area covered by 5 degrees in latitude and 10 degrees in longitude, which is based on the technique applied to the TEC data in North America presented in Tsugawa et al. (2007). An example of the smoothed map is shown in Figure 2.5.

(b) A two-dimensional Fast-Fourier Transform analysis is applied in each map and the amplitude of the dominant component of the 2D spectrum is retrieved and properly scaled.

(c) For each storm event a time series of the amplitude of the dominant component from each 2D spectrum is generated (see Figure 2.6(b)).

(d) The LSTIDs are then detected by means of the local maxima of the time series described in (c). These local maxima are obtained using the following criteria:

    - minimum threshold of 0.3 TECU;
    - minimum time interval between consecutive local maxima of 30 minutes;

    Both criteria are applied in order to avoid false detection of the LSTIDs due to noise on the data and MSTIDs. Figure 2.6 presents and example of the proposed method on the LSTIDs detection for the St Patrick's day storm of March 17, 2015 together with a Time-latitude plot (TLP) of the detrended TEC for the same period. The detected TIDs using the proposed method are indicated with the green triangles on the second and third panels. One can note that the proposed method presents good correspondence with the LSTIDs observed using the TLP.

The method for automatic detection of the amplitude of the LSTIDs allows to retrieve some statistics of the LSTIDs during the periods of storms. From the procedures (a)-(d) described above, a total of 233 LSTIDs have been detected with a maximum amplitude reaching 2.92 TECU. Figure 2.7 presents the histogram of the amplitudes (left panel) and

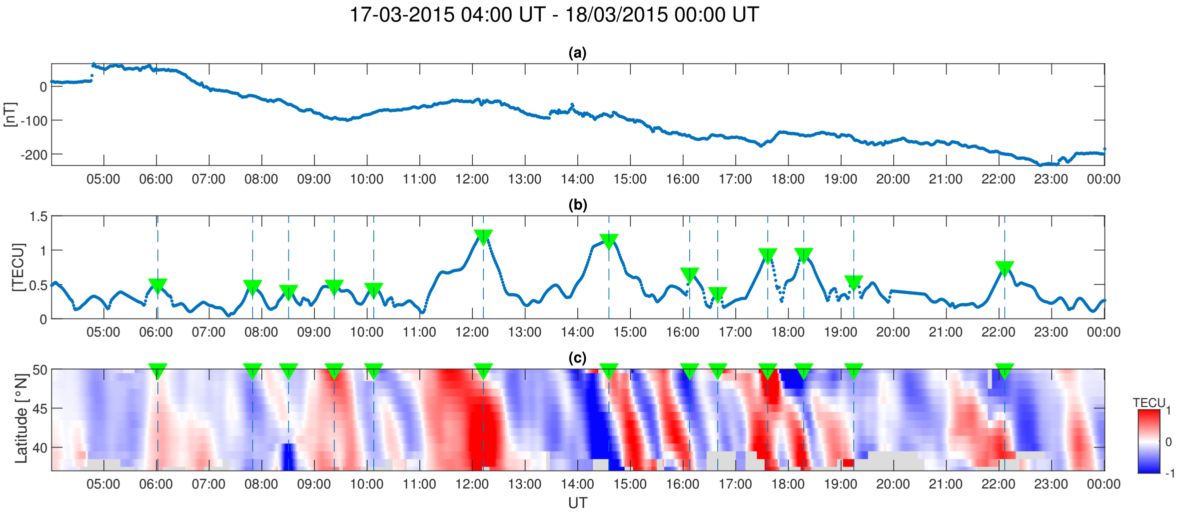

Figure 2.6 – Detection of LSTIDs using the 2D FFT for the 17/03/2015 storm: (a) SYM-H index, (b) Time-series of the max amplitude derived from the 2D FFT analysis (green triangles indicate the maximum amplitude of each detected disturbance), (c) Time-Latitude Plot (TLP) of the detrended TEC indicating the LSTIDs with green triangles.

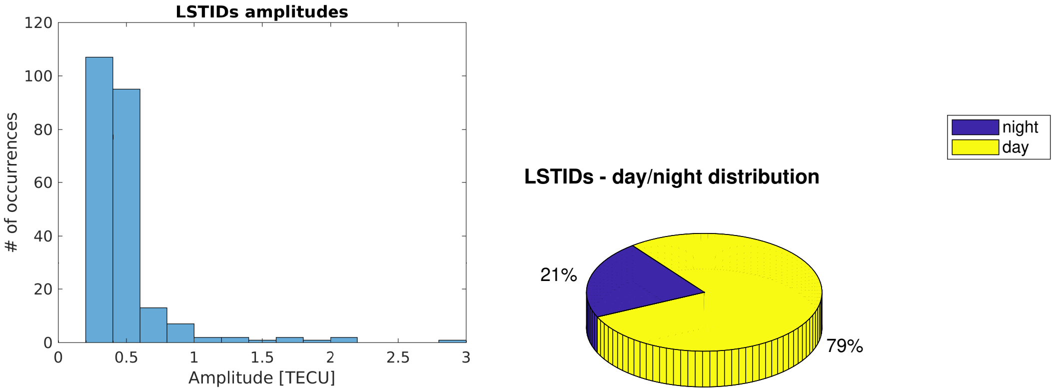

Figure 2.7 – Statistics of the LSTIDs detected via the 2D FFT transform. Left panel: Histogram of the amplitude of the detected disturbances. Right panel: Daytime and nighttime LSTIDs distribution.

the distribution of the occurrence during daytime and nighttime (right panel). Most of the observed LSTIDs presented low amplitude (around 0.3 TECU). Also, one can observe a significant asymmetry on the amount of LSTIDs generated during daytime and nighttime, even though the distribution of geomagnetic storms is rather symmetric. This difference may be explained by the LSTIDs excited by the passage of the morning terminator (Cherniak & Zakharenkova, 2018b). This LSTIDs can be observed even during quiet-time and they may have a small amplitude, when compared to the disturbances excited after the geomagnetic storm onset.

Figure 2.8 presents the amplitudes of the LSTIDs detected during daytime and nighttime periods. As one can notice, the amplitude of the LSTIDs observed in mid-latitudes (more specifically in the latitudinal range from 37 to 50° N) during daytime are lower when com-

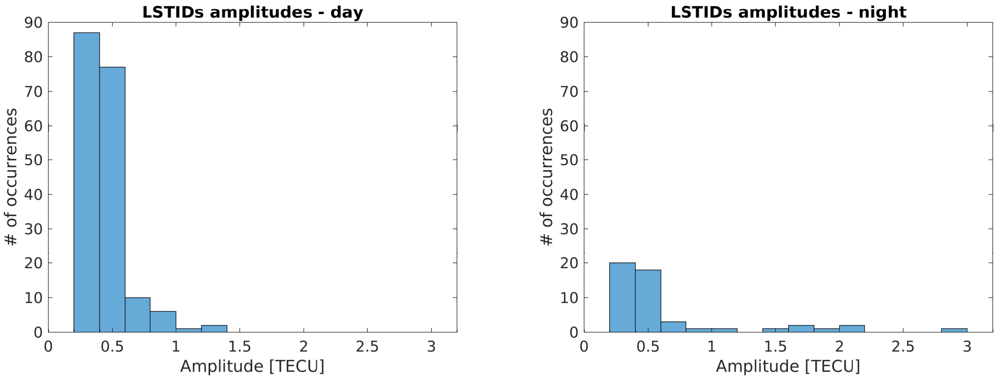

Figure 2.8 – Statistics of the LSTIDs detected via the 2D FFT transform. Left panel: Histogram of the amplitude of the detected disturbances. Right panel: Daytime and nighttime LSTIDs distribution.

pared to the nighttime ones. It is important to highlight that the amplitude of the LSTIDs identified during nighttime might be impacted by the fluctuations observed in the auroral zone. Although in the results of this investigation the auroral oval has not often expanded down to 50° N, such impacts should be considered, since the smoothing technique considers a moving average within 5 degrees in latitude. Another possible explanation for the amplitude difference between the daytime and nighttime disturbances may be the attenuation of the LSTIDs amplitude as they propagate from high to mid latitudes. As suggested by Tsugawa et al. (2003), the ion drag effect, which is proportional to the ion collision frequency, can be one of the main causes of LSTIDs attenuation. During daytime, due to the increased ionization of the F region, one can expect the enhancement of the collision frequency between ions and neutrals, which leads to the strong ion drag and therefore, stronger attenuation effect on the LSTIDs (Song et al., 2012).

2.2 Identification of potential precursors for the occurrence of LSTIDs: a case study

As presented in the previous section, a significant amount of LSTIDs have been observed even during the descending phase of solar cycle 24, with different amplitude ranges. Previous numerical simulations suggested that even large energy deposition into the ionosphere is often not accompanied by significant increase in the AGW excitation and TIDs. Sometimes, however, energy deposition that are not that strong may generate such disturbances, which makes very challenging activities such as tracking, nowcasting (Belahaki et al., 2020) and prediction of TIDs.

In order to contribute and to derive a comprehensive view on the TID mechanisms, the EU Horizon 2020 project Warning and Mitigation Technologies for Traveling Ionospheric

Disturbances Effects (TechTIDE) was conducted from 2017 to 2020 and it aimed at designing and testing new strategies for near real-time detection and warning for occurrence of TIDs (Belehaki et al., 2019), which requires the identification of appropriate indicators for the generation of LSTIDs. Different methods to track and detect TIDs have been developed (e.g. Altadill et al., 2020; Juan et al., 2018; Reinisch et al., 2018) and used to feed the TechTIDE warning service (Belehaki et al., 2019). As contribution to the TechTIDE project, this case study of the ionospheric perturbations occurring in the source region of LSTIDs has been performed, targeting the following two objectives:

1. Identification of individual ionospheric perturbation indices that can serve as precursors for the LSTIDs occurrence in the mid-latitude European region. The focus is on TEC estimates derived from Global Navigation Satellite Systems (GNSS) measurements, because they are available in near real-time. Well-known parameters are investigated, including TEC gradients (often analyzed with respect to threads for ground-based augmentation systems, Pradipta & Doherty, 2015), Rate of change of TEC index (ROTI) (Jacobsen, 2014; Pi et al., 1997), and Along Arc TEC Rate (AATR) (Juan et al., 2018);
2. Discussion of ionosphere-thermosphere dynamics, that contribute to the generation of LSTIDs. Here, the relations to Field-aligned currents (FACs) and the auroral electrojets are studied, and the auroral precipitation effects are assessed.

The geomagnetic storm registered on the 7-8th September 2017, which is part of the intense solar and geomagnetic disturbances that started on 6th September 2017, is selected as a case study. The aforementioned geomagnetic disturbances are associated with many space weather phenomena, such as, solar flares (Berdermann et al., 2018), solar radio bursts (Sato et al., 2019), and radiation storms (Mavromichalaki et al., 2018; Mishev & Usoskin, 2018), and effects on near-Earth space, such as, plasmasphere erosion (Obana et al., 2019), HF radio wave absorption and solar flare effects (Sfe, Curto et al., 2018) and Geomagnetically Induced Currents (GICs, Dimmock et al., 2019).

2.2.1 Dataset

2.2.1.1 IMAGE equivalent currents

IMAGE Equivalent Currents (IECs) represent the ground magnetic disturbance caused by ionospheric currents. The IEC are calculated from measurements of the International Monitor for Auroral Geomagnetic Effects (IMAGE) magnetometer network and the result is projected to the ionospheric plane. Thus, the IEC are horizontal equivalent ionospheric currents which correspond to the observed ground magnetic field. It is important to point out that, in reality, the true ionospheric currents correspond to a combination of horizontal and field-aligned currents, and it is not possible to distinguish those by using ground magnetometer data only (Dimmock et al., 2019; A. Pulkkinen et al., 2003). IEC provide valuable information about the ionospheric electrodynamics and magnetosphere-ionosphere coupling and it is derived by the Finnish Meteorological Institute (FMI) using the spherical elementary current system method (Amm, 1997; Amm & Viljanen, 1999; A. Pulkkinen et al., 2003). IMAGE magnetometer measurements and derived IEC can be obtained via IMAGE webpage[3].

2.2.1.2 Swarm field-aligned currents and auroral oval boundary estimation

The FACs play an important role in the energy coupling between the magnetosphere and the upper atmosphere at auroral latitudes. Therefore, the knowledge of their intensity and distribution is relevant for studies of the magnetosphere-ionosphere interactions. One way to obtain the FACs is by applying the Ampére's integral law to the magnetic field measurements from Low Earth Orbiting (LEO) satellites (e.g. Lühr et al., 1996; Ritter et al., 2013). In this work, the Level-2 product of Swarm FACs data provided by the European Space Agency[4] has been used. The FACs data are then used to estimate the boundaries of the auroral oval using the method described in Xiong et al. (2014). In this method, the auroral oval boundaries are based on the S variable, which was introduced by Heilig and Lühr (2013) to represent the FACs intensity. This variable is given by a boxcar averaging over a 20s window length applied to the logarithm of the squared FACs density ($S = \langle log_{10} j_{\|}^2 \rangle_{20s}$). The values of S, as a function of latitude, are obtained for the four high-latitude segments, from ± 40° Apex latitude (see Richmond, 1995) to the magnetic pole in the north and south hemispheres. For each segment, the auroral boundary is then estimated via an iterative process consisting of finding the linear parts of the S curve with steepest gradient.

2.2.1.3 MFACE field-aligned currents

One of the FACs estimates used in this work is obtained from the Model of Field-Aligned Currents through the Empirical orthogonal function analysis (MFACE). It is an empirical high-resolution model of FACs based on 10 years of CHAMP measurements. Empirical orthogonal functions are used to model FACs in separate magnetic local time sectors (He et al., 2014).

The model inputs are the interplanetary magnetic field (IMF), solar wind speed and AE index. The IMF and solar wind speed measurements are obtained from the Advanced Com-

---

[3] https://space.fmi.fi/image/

[4] http://swarm-diss.eo.esa.int/

position Explorer (ACE) MAG and SWEPAM instruments[5], respectively. The AE index used in this work has been provided by the Kyoto World Data Center for Geomagnetism[6].

2.2.1.4 Precipitation from DMSP

The auroral particle precipitation plays an important role in the energy input to the high-latitude ionosphere, and the characteristics of the precipitating spectra can provide useful information about the energy transfer process. In this work, the data used to investigate the contribution of the particle precipitation are derived from the Defense Meteorological Satellite Program (DMSP) low Earth orbit satellites F16A, F17A and F18A. These are polar orbit satellites with an inclination of 98.9°, nominal period of 101 min, and altitude of 840 km. Modern payloads include the Special Sensor J (SSJ) instruments which are designed to measure precipitating auroral particles and have been supporting a variety of operational and research products including energy inputs, auroral boundary identification, spacecraft charging, and field-aligned currents (Redmon et al., 2017). DMSP SSJ data used in this work are available at the CEDAR Madrigal Database.

2.2.1.5 Ionosonde data

Since TIDs reflect changes in the ionospheric electron density, ionosondes are an ideal sensor to detect and monitor them. In this study, data from the Digisondes DPS-4D located at Pruhonice (International Union of Radio Science (URSI) code PQ052, 50.0° N 14.6° E) and Juliusruh (URSI code JR055, 54.6° N 13.4° E) are used. Both stations are in the mid-northern European area, about 500 km north-south from each other and belong to the ionosonde data providers for the real-time TechTIDE warning system (Belehaki et al., 2019). The ionograms derived from Juliusruh ionosonde were obtained with a time resolution of 5 minutes. For Pruhonice, after the storm onset, a special campaign of higher temporal resolution was used (2 minutes, instead of the standard 15 minutes resolution). Frequency settings for the ionograms were modified manually within the main phase of the storm according to actual critical frequency values. The ionograms with higher resolution were recorded with the ordinary mode only, but at each 15 minutes the ionograms were obtained with the ordinary and extra–ordinary modes (Mosna et al., 2020).

For an operational use, such as HF propagation predictions or statistical long-term studies of ionospheric characteristics, data from automatic scaled ionograms available on the Global Ionospheric Radio Observatory (GIRO) web portal (Reinisch & Galkin, 2011) provide good accuracy. However, under geomagnetically disturbed conditions, with degraded critical frequencies (ionospheric G conditions, i.e. when the critical frequency of the F2 layer

---

[5] http://www.srl.caltech.edu/ACE/ASC/level2/

[6] http://wdc.kugi.kyoto-u.ac.jp/

is equal to or less than that of the F1 layer, Piggott & Rawer, 1972), spread F echoes or even out-blanked F layer echoes due to auroral E layer signatures, the automatic scaling of ionograms by the scaling software ARTIST (Galkin & Reinisch, 2008) partly fails. Therefore, ionospheric characteristics derived from automatic ionogram scaling are not always suitable for such specific case studies like the one discussed in this manuscript. These ionograms should be inspected and scaled manually, which was done by the station operators according to the Ionogram Scaling Rules. Nevertheless, there may be uncertainties in the evaluated and derived parameters of up to several tens of kilometers in height and up to a few hundreds of kHz in frequency, which are due to the sometimes ambiguous interpretation of the ionogram echoes and traces under these dynamic ionospheric conditions. Especially spread F dominated ionograms are tricky to interpret and scale.

2.2.2 Investigation of precursors for LSTIDs occurrence

2.2.2.1 The AATR index

The AATR is an indicator for regional disturbed periods in the ionosphere that can affect the GNSS applications. As shown in Juan et al. (2018), large AATR values are reached in mid-latitudes during strong geomagnetic storm, indicating that this index can be sensitive to strong ionospheric storm disturbance that originates at high latitudes and expands towards the equator. This index was developed in the context of ionospheric research for the European Geostationary Navigation Overlay Service (EGNOS), and it was chosen to serve as a way to measure the operational conditions for the EGNOS. Based on this index several studies have been conducted in order to improve EGNOS availability during the intervals of large AATR. In addition, this index has been used as a standard tool for joint ionospheric studies in Space Based Augmentation Systems (SBAS) by the International Civil Aviation Organization (ICAO, Juan et al., 2017, 2018).

Following Juan et al. (2018), the instantaneous AATR is computed as

$$AATR_i^j(t) = \frac{1}{(M(\epsilon))^2} \frac{\Delta sTEC_i^j(t)}{\Delta t}, \tag{2.6}$$

where $\Delta sTEC_i^j(t)$ corresponds to the variation between two consecutive slant TEC observations considering the receiver i and the satellite j, Δt is the time increment of the carrier-phase measurements. $M(\epsilon)$ is the slant factor described in Equation (2.4). The AATR index is then calculated by taking the RMS of the instantaneous $AATR_i^j$ calculated for a pre-defined period T for all j satellites in view for a particular station i, according to:

$$RMS_{AART,i}(T) = \sqrt{\frac{1}{N}\sum_{t=T}^{T+\Delta T}\sum_{j=1}^{n_{sat}(t)}(AATR_i^j(t))^2}, \tag{2.7}$$

where N is the total number of observations during the interval ΔT (5 minutes or 1 hour), after summing all satellites in view, $n_{sat}(t)$, at every epoch t (Juan et al., 2018). In this work an interval ΔT of 5 minutes was used. An example map is shown in Figure 2.9. The AATR data used herein is provided by the Universitat Politécnica Catalunya (UPC) via the TechTIDE warning service[7], which grants open access to real-time and archived results of the main TID detection methods from the TechTIDE project.

2.2.2.2 Rate of TEC index

One of the potential precursors for the LSTIDs occurrence investigated herein is the Rate of TEC index (ROTI). In this work, ROTI data provided by the Norwegian Mapping Authority (NMA), which operates a national network of GNSS receivers for positioning services and other investigations (Jacobsen & Dähnn, 2014), is used. In addition, the ROTI provided by the Ionosphere Monitoring Prediction Center (IMPC) which processes GNSS data in real-time to generate TEC and ROTI maps (Berdermann et al., 2018) has been included. Combined NMA and IMPC data sources can provide a good coverage over high and mid-latitude Europe.

Defined as the standard deviation of the Rate of TEC (ROT) over a certain interval, the ROTI is a commonly used index to measure the ionospheric irregularities level (Cherniak et al., 2018; Jacobsen, 2014; Pi et al., 1997). It is based on the ROT which can be computed as

$$ROT(i) = \frac{L_{GF}(i) - L_{GF}(i-1)}{\Delta t \times 10^{16} \times 40.3 \times \left(\frac{1}{f_1^2} - \frac{1}{f_2^2}\right)}, \tag{2.8}$$

where $L_{GF}(i)$ is the geometry-free phase combination at epoch i. $L_{GF}(i)$ is given by:

$$L_{GF}(i) = L_1(i) \times \lambda_1 - L_2(i) \times \lambda_2, \tag{2.9}$$

with L_n, λ_n, and f_n corresponding to the phase measurement, wavelength and frequency for the nth frequency, respectively. Δt is the time difference between the epochs, in minutes.

---

[7] http://tech-tide.eu

The ROTI is given in TECU/minute and is calculated over N epochs as

$$ROTI(i) = \sqrt{\frac{1}{N}\sum_{j=i-N}^{i}(ROT(j) - \overline{ROT})^2}. \tag{2.10}$$

where $\overline{ROT}$ corresponds to the ROT average over the N epochs. Figure 2.9 presents an example of ROTI map for the European region on 8th September 2017. In this work, the ROTI data are provided with a spatial resolution of 1° latitude × 1° longitude, with a 5 minutes cadence. The NMA ROTI is calculated over a 5 minutes interval (using 1/30 Hz data), whereas IMPC ROTI is obtained over 1 minute interval (using 1 Hz data). Despite the different methods of computation, this work combines both methods (NMA ROTI for latitudes above 50° N and IMPC ROTI for latitudes below 50° N) in order to have a good coverage over Europe.

2.2.2.3 TEC gradients

Given the threat that TEC gradients can impose on GNSS services, these gradients, associated with geomagnetic storms and other phenomena (like plasma bubbles), have been investigated over the years (e.g., Cesaroni et al., 2015; Mayer et al., 2009). Regarding the purpose of the present work, as presented in Borries et al. (2017a), the TIDs source regions can be associated with strong TEC gradients and therefore, these gradients could be a potential precursor for LSTIDs occurrence. In order to investigate this applicability, the single GPS receiver station method described in Pradipta and Doherty (2015) and Mayer et al. (2008) is used in order to infer the magnitude of the spatial TEC gradients based on the observed temporal change in TEC, as follows

$$|\nabla_{||}TEC| = \frac{|vTEC(t_1) - vTEC(t_2)|}{ds}, \tag{2.11}$$

where ds corresponds to the distance travelled by the Ionospheric Pierce-Point (IPP) from the instant t_1 to instant t_2. This method provides an estimate of the TEC gradient along the IPP trajectory and it has the advantage of not being highly sensitive to errors in the receiver bias computation (Pradipta & Doherty, 2015). From Equation (2.11), one can note that the gradients presented herein contain spatial and temporal information that cannot be separated. However, it can be used as an indicator for disturbances in the ionosphere (Mayer et al., 2009). The TEC gradients used herein are obtained by using a time difference ($t_1 - t_2$) of 1 minute and are derived from the GNSS TEC data presented in Section 2.1.1.

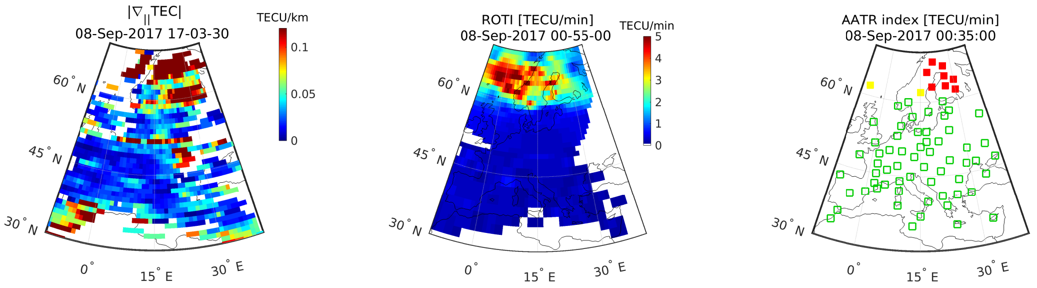

Figure 2.9 – Example maps of TEC gradients (left), ROTI (center) and AATR index (right) in three different levels: AATR ≤ 0.5 (green); $0.5 < \text{AATR} \leq 1$ (yellow); AATR > 1 (red) (Ferreira et al., 2020).

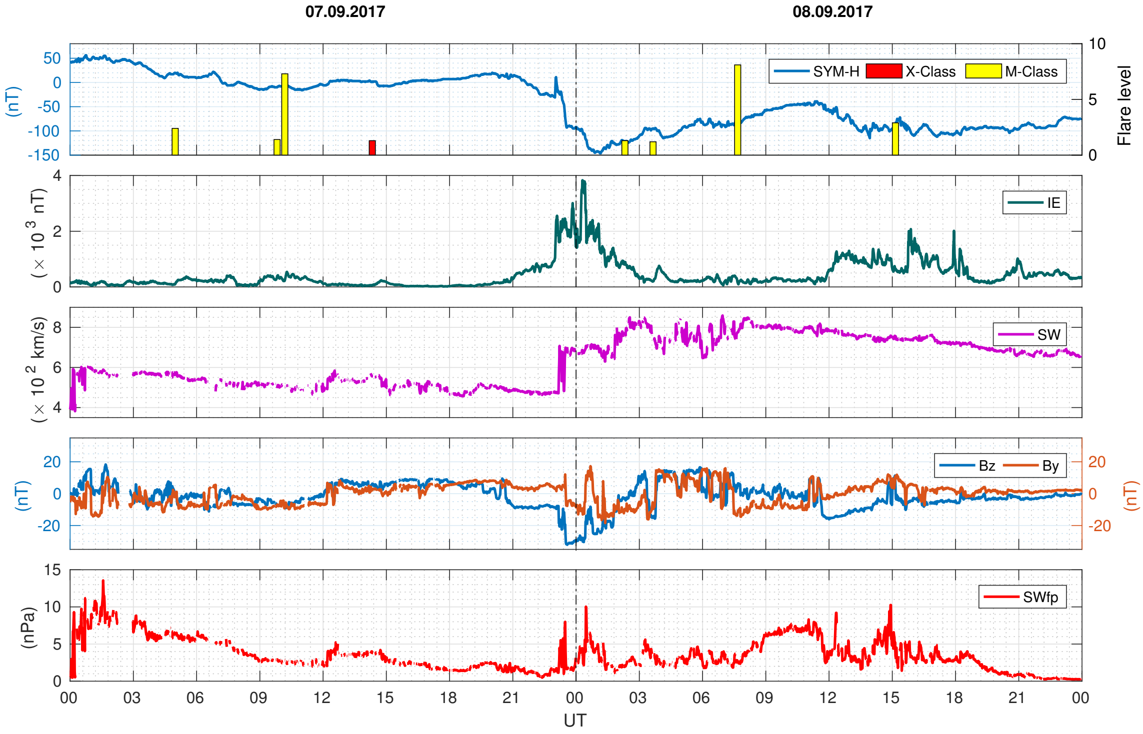

Figure 2.10 – Space weather conditions during 8th September 2017, shown with common parameters. Top panel: solid line is geomagnetic SYM-H index. Bars indicate occurrence of solar flares. Second panel: Auroral electrojet index derived from IMAGE magnetometers (IE). Third panel: solar wind speed (SW). Fourth panel: Y and Z-components of the interplanetary magnetic field (By, Bz) in the GSM coordinates. Last panel: SWfp. The solar wind data presented herein corresponds to the 1-min averaged values and involves the Earth's bow shock nose shifted ACE and WIND data available from the NASA'S OMNIWeb data service (http://omniweb.gsfc.nasa.gov/) (Ferreira et al., 2020).

2.2.3 Space weather conditions on 8th September 2017

Multiple coronal mass ejections (CMEs) associated with a X9.3-class solar flare on 6th September 2017, reached the Earth's bowshock on 7th September 2017 around 23:04 UT, and triggered a geomagnetic storm with a double main phase (Aa et al., 2019; Jin et al., 2018). The two main phases of the geomagnetic storm resulted in two periods of intense auroral activity, as indicated by the IMAGE electrojet index (IE) presented in Figure 2.10, second panel. During the first period, the auroral activity increased, with the IE index reaching a maximum of almost 4000 nT at 00:18 UT. The ring current index SYM-H decreased, indicating the first main phase of the storm, and reached a minimum value of -146 nT on 8th September at 1:08 UT (see Figure 2.10, first panel). A second period of intense auroral activity started on 8th September 2017 at 11:55 UT. The ring current index SYM-H decreased, indicating the second main phase of the storm, and reached a second minimum of -115 nT at 13:56 UT. The two periods of enhanced auroral activity were related to the periods of southward directed IMF (c.f. Figure 2.10, fourth panel). A few M-class flares did occur on the 7th and the 8th of September 2017. An additional X-class flare did occur on 7th September 2017 14:20 UT (see Figure 2.10, first panel). Solar wind speed increased with the arrival of the first CME and remained high during 8th September 2017 (see Figure 2.10, third panel).

2.2.3.1 LSTIDs and potential precursors

In order to analyze the temporal evolution of the concurrent perturbations in detrended TEC, AATR index, ROTI and TEC gradients, time-latitude plots (TLPs) for each parameter are generated (Figure 2.11). Each TLP shows the TEC perturbations at the 15° E longitude between 37 and 70° N geographic latitudes. This latitudinal sector includes mid- and part of high-latitude regions, and is also the sector with the highest data coverage over Europe during this case study (see Figure 2.1). Above or below this latitudinal sector the amount of data gaps increases significantly.

The detrended TEC shows very strong amplitudes of above 0.5 TECU after the onset of both periods of auroral activity intensification. The high latitude TEC perturbations in detrended TEC, which appear like random fluctuations, start on 7th September 2017 at around 18 UT at 70° N and extend equatorwards with time. Around 23 UT, they reach down to 58° N. The perturbations are seen at these latitudes until about 02:00 UT the next day and tend to relocate poleward until they disappear from the map around 06:00 UT. On 8th September after 11:00 UT, a significant very clear wave-like perturbation occurs at high latitudes and moves equatorward rapidly until it disappears only half an hour later at around 58° N. Such wave-like structure is observed in the TLP as a slant band of positive/negative values. This wave-like feature is marked as III in Figure 2.11. In contrast to the other high-latitude TEC perturbations in the detrended TEC, this wave-like feature has a very long zonal extent

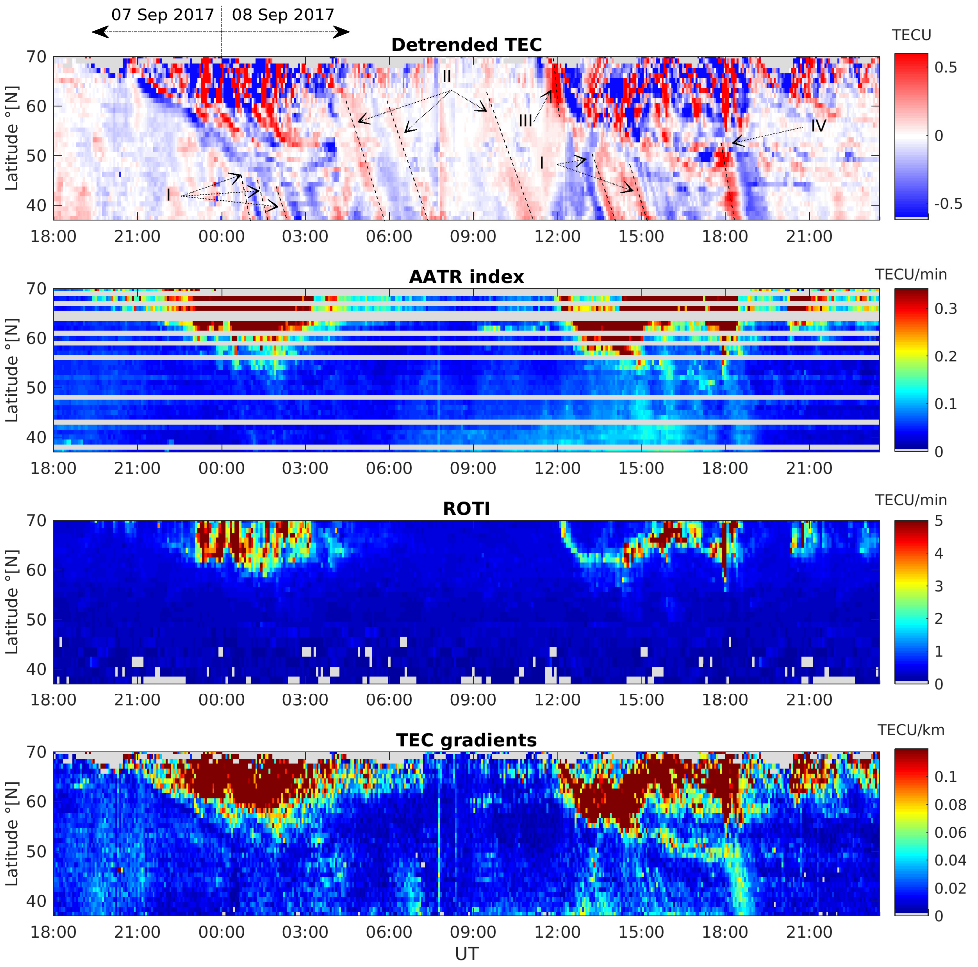

Figure 2.11 – Time-latitude-plots centered at 15 ° E of perturbations in the Total Electron Content (TEC) from 7th Sep 2017 (18:00 UT) to 8th Sep 2017 (23:59 UT), estimated with the different methods described in Section 2.2.1. First panel: Detrended TEC mostly reflecting TID amplitudes, where I corresponds to the group of fast LSTIDs in mid-latitudes, II corresponds to the group of slow LSTIDs, III corresponds to a significant strong wave-like TEC perturbation in high latitudes, IV corresponds to a strong LSTID in mid-latitudes generated in high-latitudes around 18 UT. Second panel: AATR index. Third panel: ROTI. Fourth panel: TEC gradients. Data gaps are presented in gray color (Ferreira et al., 2020).

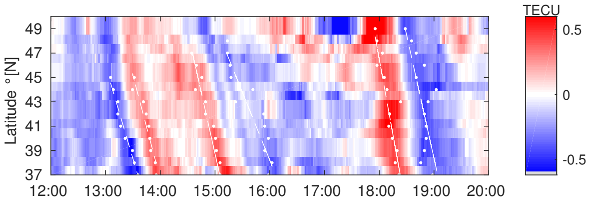

Figure 2.12 – Illustration of the linear fitting procedure used to estimate the LSTIDs propagation parameters on 8th Sep 2017, between 12:00 and 20:00 UT. White dots indicate the points for the linear fitting of crests and troughs, and the fitting results are indicated with white dashed-lines (Ferreira et al., 2020).

parallel to the auroral oval, as visible in the detrended TEC maps. After this wave-like perturbation disappears, the typical high-latitudes perturbations, which do not show clear propagation characteristics, persist. At 13 UT, they are located between around 58 to 70° N. With proceeding time, they extend more and more equatorward. At 17 UT, they can be observed between around 45 and 70° N. At 18 UT, the situation suddenly changes. High-latitude TEC perturbations appear back at higher latitudes and around 18:30 UT their activity reduces significantly for the following two hours. At the equatorward edge of the high-latitude perturbations, the detrended TEC often shows signatures that look like slanted rays. This is the signature of AGWs, observed in TEC, which are referred to as LSTIDs. The size and the tilt of the slanted rays provide the information about wavelength, velocity and period. The parameters of the observed disturbances are obtained based on the method described in Liu et al. (2019) in which the linear least-square method is used to fit pairs of crests and troughs for each disturbance, as depicted in Figure 2.12. The white dots are the minimum and maximum values around the trough and crest, respectively. Based on the slope of the fitting lines (white lines), the velocity of crest (v_c) and trough (v_t) are estimated. The LSTID velocity is then considered as the mean value of v_c and v_t. The period of the disturbance is estimated based on the time interval between trough and crest in the TLPs. The half-period of the disturbance is set as the averaged value of the time intervals between crest and trough observed at each latitude. The wavelength is then obtained from the multiplication of the speed and period. It is important to highlight that the extracted information corresponds to the zonal projection (centered in 15° E) of the LSTIDs. Moreover, it should be noted that the GNSS coverage at mid-latitudes is lower than the coverage at high-latitudes. Therefore, in order to reduce data gaps and then perform the propagation parameters estimation, the detrended TEC is averaged along a 10° band (centered in 15° E) for each latitude. This procedure, although useful, may influence to a certain extent the accuracy of the estimation of LSTIDs propagation parameters in mid-latitudes. However, it is assumed to have a minor impact on the propagation parameters estimation, because usually LSTID wave-fronts have thousands of kilometers longitudinal extend (Zakharenkova et al., 2016).

On 8th September at around 7:45 UT, there occurs a signature at all latitudes and at the same time (looks like a vertical red line). This can be caused by either solar flares or Prompt

Penetration Electric Fields (PPEF). In this case, it is caused by a strong M-class flare, which is indicated in Figure 2.10 at exactly this time. There is no indication of sources for PPEF at this time, like a reversal of the IMF Bz component.

A few LSTIDs occur between 0 and 3 UT on 8th September (indicated as I in Figure 2.11). They are not well visible and seem to interfere with other perturbations. Their properties are about 1900 km wavelength, 40 minutes period and 780 m/s phase velocity. During the morning, there occur LSTIDs with longer wavelength (approx. 2900 km), period of around 110 min and phase velocity about 430 m/s. These LSTIDs are marked as II in Figure 2.11. From 13 – 16 UT two LSTIDs with velocities of about 520 m/s are also observed. These LSTIDs present periods of 50 and 100 minutes, and wavelengths of around 1600 and 3000 km, respectively and are indicated as I in Figure 2.11. A comparably strong large-scale wave is suddenly generated at 18 UT at about 53° N (indicated as IV in Figure 2.11), when the high-latitudes perturbations move back polewards. It is a single wave with very long wavelength ($\approx$ 3300 km), period of around 80 min and typical phase velocity ($\approx$ 730 m/s) of LSTIDs during disturbed conditions.

The TLP of AATR index (Figure 2.11, second panel) shows data gaps, because AATR is measured at the location of GNSS stations only and the density of the GNSS stations is not sufficient to fill the TLP completely. Still, the amplitudes of AATR are well visible. AATR indicates TEC perturbations in the high-latitude range between 60-70° N between 23-03 UT in the night from 7th to 8th September and between 12-18:30 UT and 20:30-21:00 UT. It corresponds with the times when the detrended TEC shows high-latitudes perturbations. At 17:55 UT, AATR peaks to extreme values with amplitudes exceeding 2.3 TECU/min. It does not remain more than 5 minutes.

The TLP of ROTI look rather similar to that of AATR. There are individual data gaps in lower latitudes due to sparse data coverage. Here, the same high-latitude TEC perturbations are indicated as in AATR, but they seem to be confined further north. On 8th September 2017, between 12:00-12:30 UT, a very sharp TEC perturbation moves equatorward from 70 to 60° N and it remains at 60° N for two hours before it moves poleward again and intensifies in amplitude and horizontal extend. At 18:00 UT, there occurs a very sharp peak of ROTI with an amplitude of up to 10 TECU/min. Amplitudes that high are rarely observed in ROTI. It does not remain more than 5 minutes. In mid-latitude regions ROTI does not increase. As pointed out in Section 2.2.2.2, the ROTI computation is different for latitudes above and below 50° N. Since IMPC ROTI presents higher sample rate and short calculation time interval (1 minute) than NMA ROTI, one can expected that it would present higher values than if it was calculated as the NMA ROTI for the same region (Jacobsen, 2014). However, even with those characteristics, no significant increasing on ROTI was observed in latitudes below 50° N. In the TEC gradients and AATR, more structures seem to be visible than in ROTI. The high-latitude perturbations are similar, but seem to reach a larger horizontal

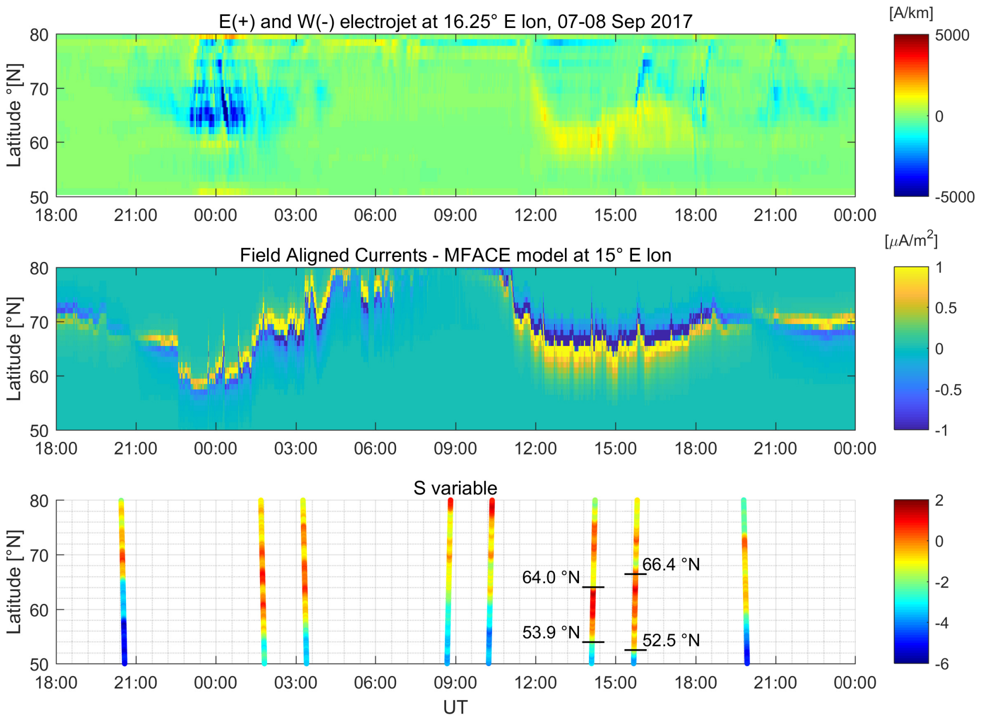

Figure 2.13 – Upper panel: Ionosphere Equivalent Currents (IEC), which indicate auroral electrojet activity (positive: eastward electrojet, negative: westward electrojet). Middle Panel: Field Aligned Currents (FAC), derived from MFACE model. Lower panel: S variable obtained from the Field Aligned Currents derived from Swarm constellation. Latitude coordinates correspond to the coordinates of Swarm satellites (vertical projection to the ground). Estimates of equatorward auroral oval boundaries and their geographic latitudes are indicated as black horizontal lines (Ferreira et al., 2020).

extend. Next to this, weaker TEC gradients are visible in mid-latitudes, where LSTIDs are present. Remarkable is a thin band of TEC gradients which start at around 15 UT at 53° N and move equatorward. At around 17 UT, the thin band of TEC gradients is located at 50° N. In comparison with the detrended TEC, this thin band of TEC gradients is located in the transition region between high-latitude perturbations and LSTIDs in mid-latitudes. At 18 UT, a TEC gradient with moderate amplitude occurs at about 50° N and moves then equatorward. It is associated to the signature of the single strong LSTID observed in the detrended TEC (indicated as “IV” on Figure 2.11, first panel), because it occurs at the same time with the same wavelength (≈ 3300 km) and phase velocity (≈ 730 m/s).

2.2.3.2 *Dynamics in the thermosphere-ionosphere: Relation of TEC perturbations to FAC and the auroral electrojet activity*

In order to investigate the contribution of ionospheric currents to the LSTIDs excitation, this work analyses the IEC, and the FACs derived from the MFACE model and Swarm mission measurements shown in Figure 2.13. It is important to point out that in this section, in addition to the geographic latitudes, some of the observations are also presented in Apex magnetic latitudes (Richmond, 1995). In these cases, the observations have been projected along the field line to the altitude at E region (110 km), enabling the direct comparison of observations from different instruments.

Figure 2.13 shows a clear enhancement of the IEC during the two phases of the storm (night from 7th to 8th September and afternoon of 8th September). During the first main phase there occurs an enhancement and equatorward shift of the westward electrojet from 70° N to 62° N (67° N to 59° N, Apex latitude). This equatorward shift of currents is also observed in the FACs obtained from the MFACE model. According to the MFACE model, the FACs seem to be located at the equatorward edge of the westward electrojet. Swarm FAC in situ data represented by the S variable (Figure 2.13, lower panel) are shown to verify the MFACE model data. The S variable also shows an equatorward movement of FAC boundaries during the first main phase of the storm, reaching latitudes ∼54° N (52° N, Apex latitude). This is significantly more equatorward than the model prediction. This equatorward shift of currents, which is linked to an expansion of the auroral oval, relates well with the equatorward expansion of strong high-latitude TEC perturbations observed on the detrended TEC (Figure 2.11, upper panel). Thus, the high-latitude TEC perturbations seem to be located within the auroral oval.

During the second main phase of the geomagnetic storm, an intensification of the eastward electrojet occurs around 12 UT and it shifts equatorward from 72° N to 60° N (69° N to 56° N, Apex latitude) within very short time (less than 1 hour). After that the eastward electrojet remains located at 60° N (56° N, Apex latitude) for about one hour, then it moves poleward again and reduces its intensity slightly. At 18 UT, the westward electrojet becomes dominant again. In general, the electrojet intensity during the second period of intense auroral activity is not as strong as the intensity of the westward electrojet during the first period. A similar location is reproduced by the MFACE model for the FACs (Figure 2.13, middle panel). However, the model predicts stronger intensity of FACs in the second period of intense auroral activity relative to the first one. It is also important to note that during the second period of intense auroral activity, Swarm measurements indicate FACs activity further equatorwards than what is indicated by the MFACE model. At 14:06 UT, Swarm B measures the equatorward edge of the auroral oval at 54° N (51.5° N, Apex latitude) and at 15:42 UT it is at 52.5° N (50.4° N, Apex latitude). The Swarm estimates of the auroral oval edge correspond well with the edge of high-latitude TEC perturbations, showing again that the high-latitude TEC perturbations are located within the auroral oval.

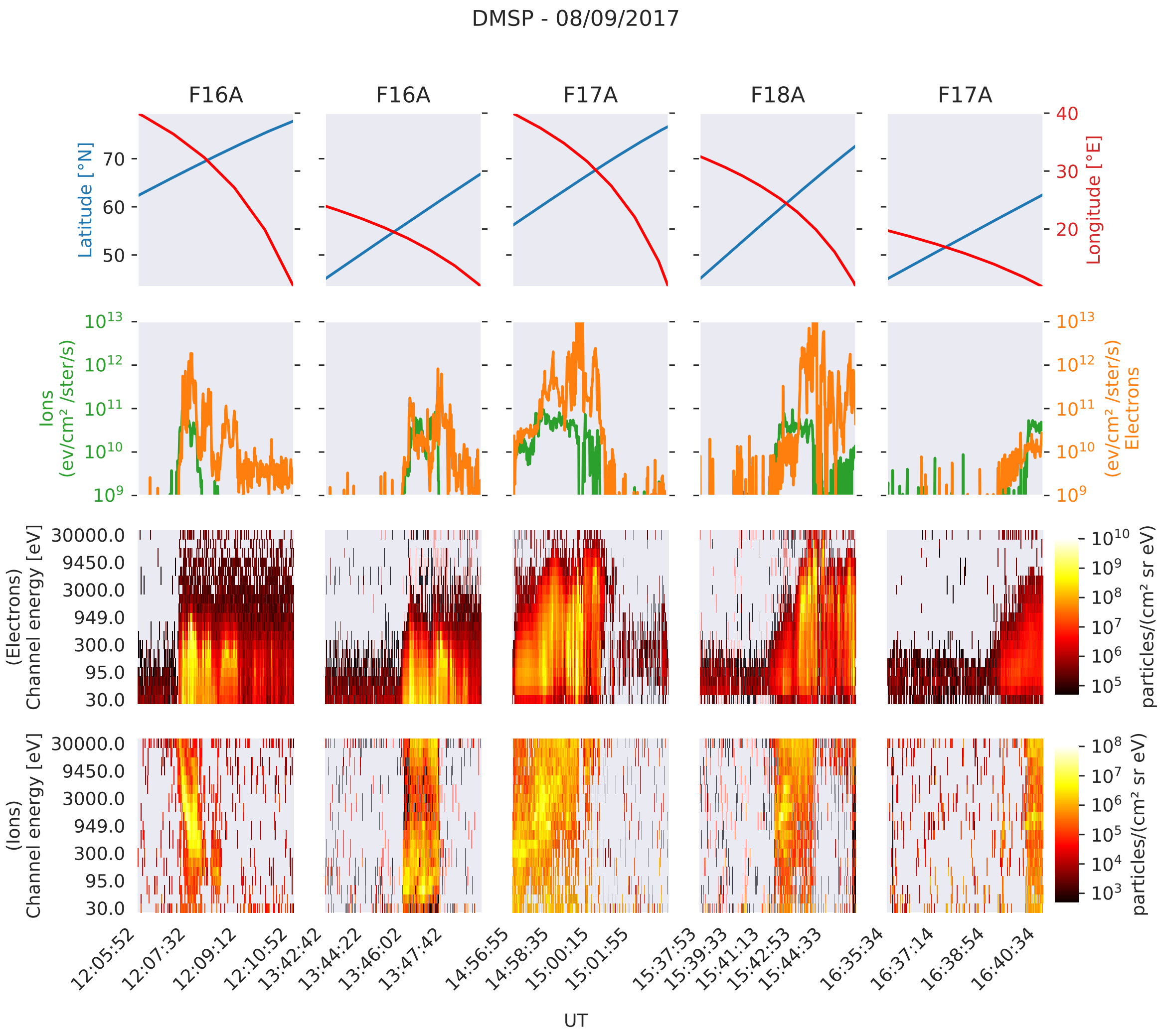

Figure 2.14 – Selected DMSP crossings over Europe on 8th September 2017 for DMSP satellites F16A, F17A and F18A. First panel: Geographic coordinates of the satellite during the passage (vertical projection to the ground, also known as satellite ground-track). Second panel: Integrated electron/ion energy flux. Third panel: Differential electron energy flux. Fourth panel: Differential ion energy flux (Ferreira et al., 2020).

2.2.3.3 Dynamics in the thermosphere-ionosphere: Relation of TEC perturbations to particle precipitation

For information about the occurrence of particle precipitation, measurements from Juliusruh and Pruhonice ionosondes and DMSP satellites are used. In ionosonde measurements, a particle precipitation is normally manifested by an enhanced Aurora E-layer, a sporadic E-layer like signature, but with slightly increasing heights with increasing frequency. For the afternoon of 8th September, no Aurora E was observed over Juliusruh. Hence no precipitation occurred at 54.6° N, 13.4° E. Occasionally, Pruhonice measures sporadic E-layer with increased heights in the time between 11:13–12:03 and 14:37–17:06 UT on 8th September (Mosna et al., 2020). Juliusruh shows similar weak structures partly between 15:13-16:13 UT. But in both stations the observed structures have a duration of only few minutes and they do not show the typical Aurora E characteristics. Moreover, they have a cloudy, non-continuous structure.

Interestingly, in the afternoon hours (after 17:30 UT) the ionograms in Juliusruh show strong oblique spread F echoes up to 1 MHz frequency spread which are not reflected from the zenith, but slightly south, with zenith angles (see schematic representation in Figure 2.15) up to 20° (i.e. elevation angles above 70°). These oblique echoes indicate that the ionosphere is tilted in North-South direction with increasing heights from South to North. Also Pruhonice measurements show this kind of oblique echoes. Furthermore, between 14 and 16 UT, the F-region ionosphere over the two ionosondes is perturbed and does not have homogeneous horizontal structure.

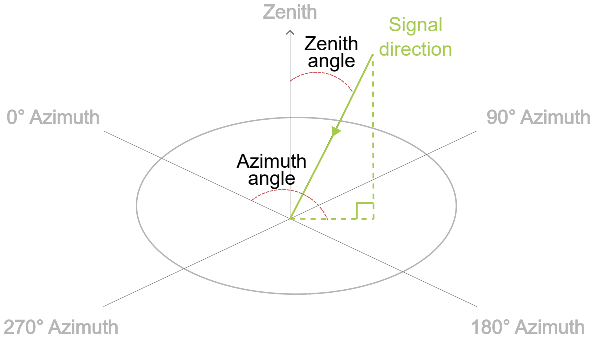

Figure 2.15 – Schematic representation of Zenith and Azimuth angles.

Precipitation measurements from the DMSP satellites passing over the European sector during the afternoon of the 8th of September 2017 are shown in Figure 2.14. By observing the integrated and differential energy fluxes one can note that significant particle precipitation occurs in latitudes above 58° N. This region has a good correspondence with the region where high-latitude perturbations are observed in the detrended TEC (Figure 2.11, upper panel). This indicates that particle precipitation influences this region of strong ionospheric perturbations at high-latitudes. However, particle precipitation does not occur in the region further equatorward down to 52° N, where one can observe TEC gradients and auroral boundary signatures.

2.2.4 Discussion

2.2.4.1 Applicability of indices as precursors for LSTID occurrence

A precursor for the occurrence of LSTIDs is considered to be a parameter that exceeds a certain threshold before LSTIDs occur. As described in the earlier section, several different types of LSTIDs are observed during 8th September 2017:

I. Fast LSTIDs in mid-latitudes between 0-3 UT and 13-16 UT;

II. Slow LSTIDs between 3-12 UT;

III. A significant strong wave-like TEC perturbation at high-latitudes, which vanishes around 58° N;

IV. A strong single LSTID at mid-latitudes generated at high-latitudes around 18 UT.

These disturbances are indicated as I, II, III, and IV, respectively, in Figure 2.11, first panel. In the case of fast LSTIDs, AATR, ROTI and TEC gradients show significant amplitudes at high latitudes prior to the LSTID occurrence. Thus, they are all suitable candidates to be used as precursor for such ionospheric perturbations. However, the relation to LSTID occurrence seems to differ between these indices. While ROTI amplitudes are high only in latitude range between 60 and 70° N, AATR and TEC gradient amplitudes follow more accurately the expansion of the strong ionospheric high-latitudes perturbation observed in the detrended TEC (Figure 2.11, upper panel). The relation with LSTID occurrence is also reflected in moderate amplitudes in regions where LSTIDs occur. In addition, AATR and TEC gradients show the same boundary of high-latitude perturbations and mid-latitude LSTID occurrence (source region of LSTIDs which moves from 55° N at 15 UT to 50° N at around 18 UT) which is visible in the detrended TEC. Although ROTI reflects high-latitude perturbations, the affected region does not cover the whole auroral region (as shown in the comparison with Swarm auroral oval boundaries Figure 2.13). ROTI is known to indicate regions affected by auroral precipitation (Cherniak & Zakharenkova, 2015) and the same behavior is also evident in this case study (comparing DMSP electron precipitation and ROTI in Figs. 2.9 and 2.14). Hence, ROTI does not cover well the source region of LSTIDs. In addition, ROTI does not reflect LSTIDs signatures at mid-latitudes. This is in accordance with the results presented in Cherniak and Zakharenkova (2018b). Therefore, AATR and TEC gradient indices are considered to be more accurate in indicating the potential generation of LSTIDs.

There is no perturbation index that can serve as precursor for the slow LSTIDs observed in the morning hours (indicated as II in Figure 2.11). It is likely that they are related to the passage of the morning terminator, as shown in Cherniak and Zakharenkova (2018b). Therefore, no ionospheric perturbation index is suitable for predicting this kind of LSTIDs. They are considered to be a regular phenomenon with smaller amplitudes than those LSTIDs generated by auroral activity. In Chum and Podolská (2018) this kind of TIDs is discussed and it is shown that they can propagate in different directions.

The significant strong wave-like TEC perturbation at high latitudes (indicated as III in Figure 2.11) is reflected in all the perturbation indices, indicating that this is not a free atmospheric oscillation, but a direct impact of auroral precipitation or ionospheric currents.

The strong single LSTID propagating at around 18 UT (indicated as IV in Figure 2.11) occurs after all three ionospheric perturbation indices show significant spikes in their data. The same generation mechanism as the earlier discussed fast LSTIDs is attribute to this LSTID. However, in this case the driving mechanism is so intense that it is manifested by significant amplitudes of AATR, ROTI and TEC gradients.

Besides the analysis of LSTIDs, it is important to note that also signatures of flares are included in the presented results. The M-Class flare, which occurred on 8th September 2017 at 07:40 UT, is visible as a vertical line in the TLP of detrended TEC, AATR and the TEC gradients. Although signatures of flares in ROTI have been reported by Berdermann et al. (2018), ROTI does not depict the flare in this case study. It can occur due to the time interval of the ROTI calculation (5 min), which can remove/reduce short-lived peaks due to the inherent smoothing effect of the computation method (Jacobsen, 2014).

2.2.4.2 Dynamics contributing to the generation of LSTIDs

LSTID are understood to be generated by sudden strong heating in the auroral region. Heating occurs either due to dissipation of currents or precipitation. Often both effects will contribute to the strong heating. In this case study, LSTIDs are generated more frequently and with higher amplitude during periods with enhanced electrojet activity, indicated by increased IE index. Also the phase velocity seems to increase during periods with increased IE. This indicates that not only the LSTID amplitude relates with auroral electrojet activity (as described in Borries et al. (2009)), but also period and phase speed.

LSTIDs are supposed to start at the edge of the auroral oval, where the currents are located and particle precipitation occurs (Cherniak & Zakharenkova, 2018b). This seems to be valid for the LSTIDs observed in the night from 7th to 8th September and for the first LSTIDs of the second period of intense auroral activity (indicated as I in Figure 2.11). However, there is a period between 15 and 18 UT, in which the auroral oval boundary cannot be clearly identified because horizontal currents and FAC are not in the same latitudinal region.

Starting around 15 UT, the region of the FAC location is several degrees equatorward of the location of the horizontal currents and the LSTID amplitudes become smaller for a few hours. The LSTID source region coincides with the auroral oval boundary indicated by Swarm measurements and is characterized by enhanced TEC gradients, indicating electrodynamic processes in this region (Borries et al., 2017a). In addition, the typical strong high-latitude TEC perturbations, which are observed between the LSTID source region and the TEC gradients enhancement at about 50° N, reflect auroral activity.

To support the unusual auroral activity in the region 50-55° N, Figure 2.16 presents related measurements from the Juliusruh and Pruhonice ionosondes. Figure 2.16 (upper panel) shows the critical frequency $foF2$ and the spread F parameter FF ("URSI code 86"), which

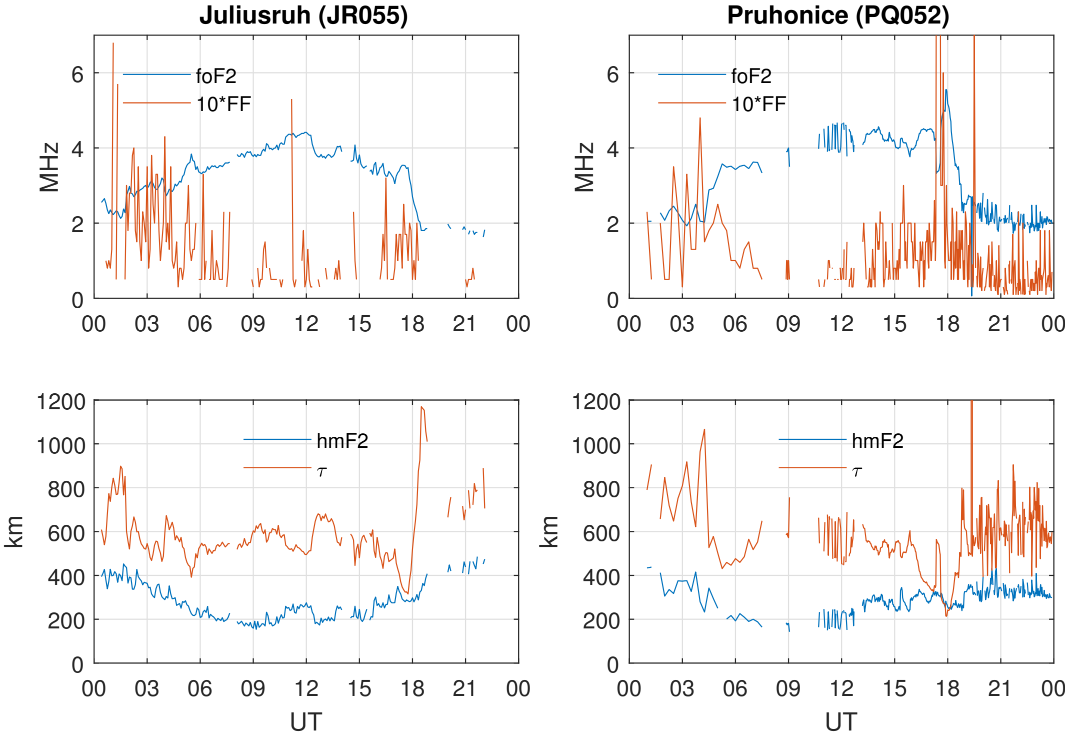

Figure 2.16 – Ionosonde measurements on 8th September 2017, at Juliusruh (54.6° N, 13.4° E, left panels) and Pruhonice (50.0° N, 14.6° E, right panels). Top: foF2 and spread F parameter FF. Bottom: Height of F2-layer $hmF2$ and equivalent slabthickness τ (Ferreira et al., 2020).

corresponds to the frequency spread between the critical F-layer frequency and the highest recorded F-layer echo for a specific wave mode, ordinary or extraordinary (Gamache & Reinisch, 1990). Figure 2.16 (lower panel) presents the height of the maximum electron density $hmF2$, and also the equivalent slab thickness τ, which gives an approximation of the altitude range over which the electrons are spread. τ, which is derived from $foF2$ and TEC, is a valuable parameter for characterizing ionosphere perturbations. It has already been used in Borries et al. (2017a) for discussing LSTID generation mechanisms. One can observe that τ is rather high on 8th September 2017. An unusually stratified F layer is causing the large τ values. This is accompanied by an increased spread F (FF parameter in Figure 2.16) in Juliusruh and Pruhonice, starting at 12 UT. High FF indicates plasma instabilities in the F-layer, e.g., bubbles occurring at this time, supporting the assumption that the ionosphere is not homogeneously layered. It is important to mention that the scatter in the variables presented in Figure 2.16 is related to uncertainties in the interpretation and manual scaling of the disturbed-time ionograms, as described in Section 2.2.1.5.

Between 16 UT and shortly before 18 UT, $foF2$, which is proportional to the maximum electron density of the F2-layer, increases and τ decreases. This shows a compression of the ionosphere to a thinner layer. Either northward winds or electric fields can cause the plasma transport leading to this change in electron density. Since an intensification of northward winds in mid-latitudes during a period of intense auroral activity is unlikely, electric fields are considered to be the source. Strong horizontal and vertical plasma drifts in this time interval are reported over Pruhonice in (Mosna et al., 2020). Specifically, the westward plasma flow increases constantly between 14 and 18 UT reaching 400 m/s. This strong plasma flow is assumed to be caused by electric fields penetrating to sub-auroral latitudes (Foster & Vo, 2002; Pokhotelov et al., 2008). These sub-auroral polarization streams, which occur between 15-18 UT, are considered to cause the observed TEC gradients between 50-55° N, and unusual stratification of the F-layer at this time too.

Very significant is the wave-like TEC perturbation on 8th September at around 11:30 UT at high latitudes (marked as III in Figure 2.11). In contrast to the LSTID signatures, this wave-like perturbation is visible not only in the detrended TEC, but also in ROTI, TEC gradients and AATR. Since its amplitude is large compared to the other LSTIDs, it must have a strong forcing. The fact that it vanishes at around 58° N indicates that it is not a free wave but a forced wave, which disappears as soon as the forcing mechanism ceases. In Figure 2.13, it is shown that the eastward electrojet and FACs are located in the same region. They have enhanced intensity and move equatorwards from 80 to 60° N between 11:30 and 12:00 UT, the same way like the TEC perturbations. This indicates that the dislocation of the currents causes the wave-like TEC perturbation. The dislocation of the currents relates with a sudden equatorward shift of the cusp, which is reported in Yamauchi et al. (2018). It was attributed to the sudden IMF southward turning, resulting in a strong anti-sunward plasma convection flow observed near local noon by the Tromsø radar.

The single LSTID, generated at 18 UT on 8th September 2017, had a rather large amplitude compared to the other LSTIDs observed during this day. It must be related to intensive dynamics in the thermosphere-ionosphere-magnetosphere system. This is not obvious from the Dst and IE indices, but it is indicated by the peaks in ROTI and AATR. Strong electrodynamic processes are also evident considering the results of Dimmock et al. (2019), who reported significant Geomagnetically Induced Current (GIC) at 18 UT in Fennoscandia. Since neither the solar wind and IMF, nor the geomagnetic indices show significant perturbations at that time, magnetosphere-ionosphere electrodynamics must be the source of the LSTID and the GIC. Magnetometer measurements provided by the IMAGE network and Juliusruh station (JR0) reflect the perturbations of ionosphere currents by strong temporal changes in the geomagnetic field strength. Figure 2.17 shows that significant amplitudes of dB/dt are apparent from high latitudes down to 60° N. Although the magnitude of dB/dt becomes smaller with decreasing latitude, the sudden increase of dB/dt at 18 UT is still visible at Niemegk (NGK, 52° N). Also the ionosonde measurements indicate a significant change in the electrodynamics a few minutes before 18 UT. While the westward plasma flow was increasing constantly between 14 and 18 UT, reaching a maximum value up to 400 m/s right before 18 UT, it decreased significantly after this peak. In addition, $foF2$ starts to de-

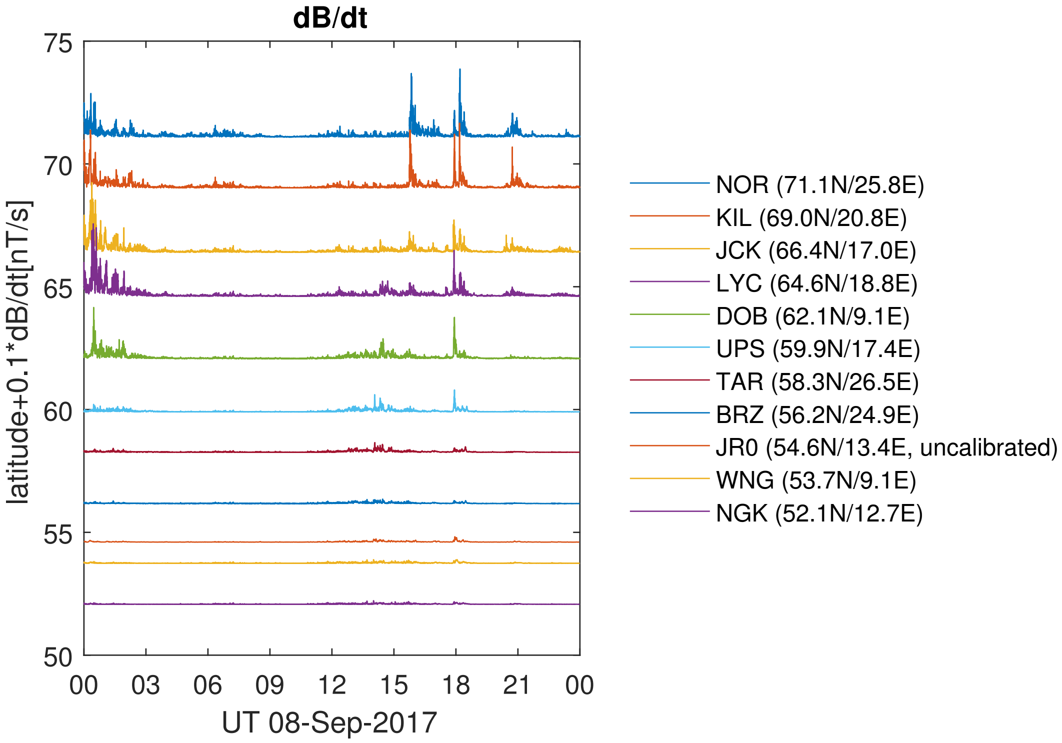

Figure 2.17 – Temporal change of geomagnetic magnetic field derived from different magnetometer stations (Ferreira et al., 2020).

crease significantly at both ionosonde stations a few minutes before 18 UT and τ increases significantly. This is a dramatic change in the plasma transport, because now the plasma is distributed over a very large altitude range. Since electric fields are considered to cause the plasma transport, a reversal of electric fields is considered to be the source of the extreme ionosphere perturbation at 18 UT. Figure 2.13 reveals that at the same time at higher latitudes the auroral electrojet also reverses from strongly eastward to westward and the FACs also reverse. This manifests the Harang discontinuity (Erickson et al., 1991), which normally occurs a few hours before midnight.

On 8th September 17:55 UT rapid changes in the ionosphere currents and changes in the electric fields trigger a GIC and a single strong LSTID. The significantly large LSTID starts at 53° N and moves equatorward with a speed of $\approx$ 730 m/s, a period of $\approx$ 80 min and a wavelength of $\approx$ 3300 km. After 18 UT, ionosphere perturbations reduce significantly for about 2 hours. Only the single large LSTID, which has been generated by the quick extreme enhancement of ionosphere currents, moves equatorward.

2.2.5 Summary

The analysis presented in this chapter aims at investigate the occurrence of geomagnetic storms and LSTIDs over the European sector from 2015 to 2019. In this investigation one could observe several geomagnetic storms and excited LSTIDs, even though the period of analysis corresponds to the descending phase of the SC 24. Most of the observed storms can be classified as moderate, and were more likely to occur during equinoxes and during the years closer to the solar maximum. The investigation of the LSTIDs excited during the period show that most of the disturbances do not present very strong amplitudes, with the majority having amplitudes below 1 TECU. Also, during the period one can observe stronger disturbances during nighttime than during daytime, which may be related to the ion drag effect. It was also observed a significant asymmetry on the occurrence of the LSTIDs during daytime and nighttime, which might be related to the occurrence of TIDs excited by the solar terminator.

In addition, the manifestation of the LSTIDs over mid-latitude Europe during the space weather events registered during the night of 7th to 8th September 2017 has been analyzed. The analyses included on the one hand the investigation of potential ionospheric perturbation indices that can serve as precursors for the LSTIDs occurrence and, on the other hand, the investigation of generation mechanisms for the observed LSTIDs via a detailed analysis of the electrodynamics. In order to perform this investigation, different ground and space based measurements, together with empirical models, have been employed in order to obtain a comprehensive picture of the mechanisms responsible for the LSTIDs excitation during the aforementioned geomagnetic storm.

GNSS data from ground-based stations have been used in this study to identify the LSTIDs and their different characteristics in amplitude, period and phase speed. The manifestation of fast LSTIDs in mid-latitudes has been observed between 0–3 UT and 13–16 UT; slow LSTIDs were observed between 3–12 UT; a forced wave-like perturbation at high-latitudes occurred around noon; and a strong and large LSTID at mid-latitudes was recorded around 18 UT. The weak and slow LSTIDs observed from 3–12 UT are likely to be induced by the morning terminator passage. Strong heating due to dissipation of currents and particle precipitation are concluded to be the main contributors for the other observed LSTIDs. However, particle precipitation was rather weak in the LSTID source region during the second period of intense auroral activity in this case study. The single rather strong and large LSTID observed around 18 UT was generated after a reversal of electric fields and auroral currents. This reversal caused sharp and very intense changes in the ionosphere currents that also triggered GIC in Fennoscandia.

The most pronounced LSTIDs occurred after strong ionospheric perturbations at high-latitudes. These high-latitude perturbations were reflected in significant amplitudes in TEC gradients, AATR index and ROTI. Often, LSTIDs signatures start at the equatorward edges of these high-latitude perturbations. For the first time, a joint comparison of the three different indices has been performed in the context of LSTIDs and their applicability to serve as precursors has been investigated. AATR index and TEC gradients follow more accurately the expansion of the strong ionospheric high-latitude perturbation observed in the detrended

TEC, which is caused by sub-auroral polarization streams. In addition, the boundary of high-latitude perturbations depicted in AATR index and TEC gradients shows good agreement with the source region of the LSTIDs. These results indicate that AATR index and the TEC gradients are promising candidates for near-real time indication and warning for the LSTIDs occurrence in mid-latitude Europe. Apart from the LSTIDs generated by storm dynamics, it must be considered that weak LSTIDs are a regular phenomenon in the morning hours. They are likely associated with the passage of the solar terminator. The terminator itself has to be considered as precursor for these LSTIDs.

Since such indices are obtained from ground-based GNSS TEC measurements, such indicators could be a valuable tool for near-real time indication and warning for LSTIDs occurrence over mid-Latitude Europe. Prediction activities with longer prediction horizons would require, however, a different approach. A possible alternative for such kind of warning/prediction can be the use of solar wind information at the Lagrangian point L1 to give insights on the possible occurrence of ionospheric/thermospheric disturbances. Results in this regard are presented in the next chapter.

3 Prediction of Space Weather Events Based on Solar Wind Measurements

Parts of this chapter have been published as: Ferreira, A. A.; Borges, R. A.; Performance Analysis of Distinct Feed-forward Neural Networks Structures on the AE Index Prediction. **2021 IEEE Aerospace Conference (50100), Big Sky, MT, USA, 2021, pp. 1-7** © *2021 IEEE; and*
Borries, C. ; Ferreira, A. A.; Nikyel, G. ; Borges, R. A . A new index for statistical analyses and prediction of traveling ionospheric disturbances. **Journal of Atmospheric and Solar-Terrestrial Physics**, *v. 247, p. 1-13, 2023, which is published under the terms of the Creative Commons Attribution License CC BY 4.0 (https://creativecommons.org/licenses/by/4.0).*

As discussed in Chapter 1, space weather disturbances, such as geomagnetic storms and substorms, can affect the operation of modern equipment and systems that mankind currently relies on. The impact on technological infrastructure can include electric power grids, impacts on satellite drag, space radiation, failure on space and ground assets, and direct effects on radio wave communication systems. Therefore, it is essential to monitor and forecast those space weather disturbances in order avoid damage and losses (Berdermann et al., 2018; Gu et al., 2019; Schrijver et al., 2015).

The energy produced by the Sun and transported by the solar wind reaches the Earth and is dissipated via different processes. This energy carried out by plasma flows causes three major current systems in the magnetosphere-ionosphere system generating three different kind of magnetics disturbances: Chapman-Ferraro current, ring current and auroral electrojet. In terms of energy flow, these processes can be treated as an input-output problem (Akasofu, 2018).

Given the threats the severe geomagnetic events can impose to technological systems, several efforts have been made to model, monitor and predict the SWe events. Among the techniques used on the prediction of SWe events, Artificial Neural Networks (ANNs) have been extensively employed (Camporeale, 2019a). Different ANN models have been used to estimate SWe events, such as substorms and solar flares (Camporeale, 2019a; Maimaiti et al., 2019; Zheng et al., 2019). Also, these techniques have been employed on the prediction of different geomagnetic indices, such as the Dst and the K_p index (Ayala Solares et al., 2016; Boynton et al., 2011; Camporeale, 2019a). In this chapter, investigations on the prediction of the AE index using ANN have been performed and the results are presented in the next section[1].

---

[1] Section 3.1 and its subsections have been reprinted, with permission, from Ferreira and Borges (2021):

3.1 Prediction of the Auroral Electrojet Index

Different studies have been carried out aiming at forecasting the AE index, which is commonly associated to the occurrence of substorms. Prediction of the smoothed AE index via ANN considering as inputs the vB_z component of the IMF together with previous values of the AE index has been presented in Takalo and Timonen (1997). A study conducted by Gleisner and Lundstedt (1997) investigated the relationships between individual solar wind variables and corresponding coupling functions on the estimation of the AE index using ANN and found that the solar wind number density is an important parameter for the AE index estimation. Investigations on how the performance of the ANN Elman network (with IMF B_z and solar wind speed V_x as inputs) varies according to the resolution of the AE index can be found in Pallocchia et al. (2008). The use of solar wind-magnetosphere coupling functions as inputs of an ANN in order to predict 1, 3 and 6 hours ahead, considering data from 1998-2009, is presented in Bala and Reiff (2012).

In this study, the goal is to assess the performance of different ANN structures (different amount of neurons and types of inputs) on the prediction of the hourly averaged AE index in order to determine which structure could be a better candidate to be used in operational services of AE predictions. Since the AE measurements can take days to be released, which would limit the use of the model for operational purposes, this study does not include historical values of the AE index as an input of the ANNs.

3.1.1 The AE index

The AE index was introduced by Davis and Sugiura (1966) as a measure of global electrojet activity in the auroral zone. The fluctuations in the solar wind convection electric field produced by variations in the solar wind velocity and IMF leads to changes in the auroral electrojet (Gu et al., 2019; Milan et al., 2017). The index is derived from measurements of the horizontal component of the Earth's magnetic field obtained from a series of ground-based magnetometers (Bala & Reiff, 2012). It is an index widely used for research on geomagnetism, solar-terrestrial physics and aeronomy.

The AE index is derived from the AU and AL indices, which are obtained from the *upper* and the *lower* envelops of the superposed H-components curves collected from a set of magnetometers located at geomagnetic latitudes between 60° and 70°N rather evenly distributed over all longitudinal sectors of the Earth (Pallocchia et al., 2008). In other words, among the data from all the stations at each given time (UT), the largest and smallest values are selected to generate the upper and lower envelopes (WDC KYOTO, 2001). The AE index is

---

Ferreira, A. A.; Borges, R. A.; Performance Analysis of Distinct Feed-forward Neural Networks Structures on the AE Index Prediction. *2021 IEEE Aerospace Conference, Big Sky, MT, USA, 2021, pp. 1-7* © 2021 IEEE.

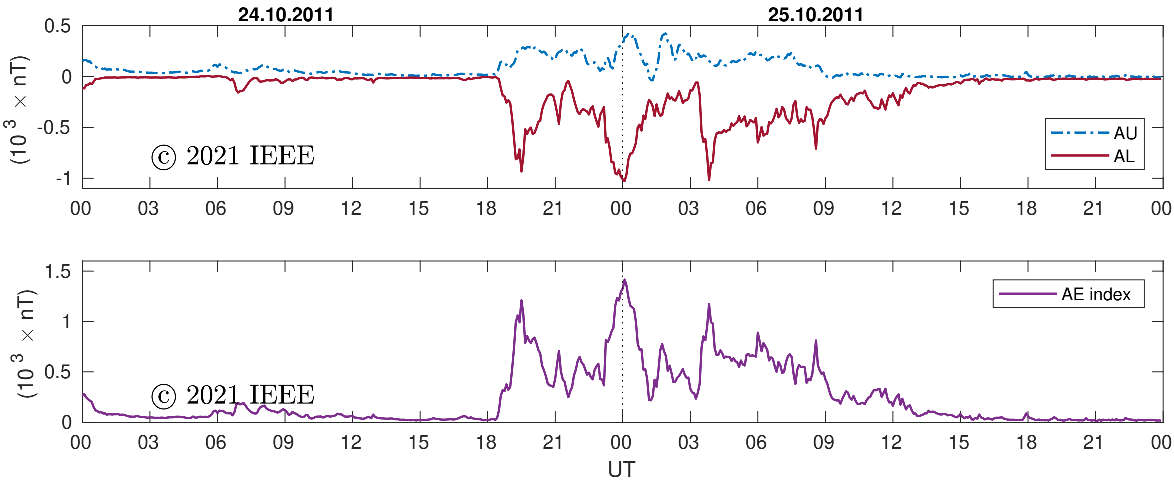

Figure 3.1 – AL, AU, and AE index profiles during the space weather events on the 24-25 October 2011 (Ferreira & Borges, 2021).

then defined as AE = AU - AL and can provide an estimate of the auroral electrojet strength (Davis & Sugiura, 1966). Figure 3.1 presents a profile of the AU, AL, and AE index during the geomagnetic substorm registered from 18 UT on 24th October 2011. As can be noted, the AE index can be significantly increased during geomagnetic events. Therefore, accurate estimates/forecasts of the index can be useful in monitoring the magnitude of substorms and other related phenomena, such as predicting the amplitude of Large Scale Travelling Ionospheric Disturbances (LSTIDs), given the correlation the amplitude of the AE has with the amplitude of LSTIDs (Borries et al., 2009).

3.1.2 The neural network model

This investigation assesses the performance of different Multi-Layer Perceptron (MLP) neural networks on the forecasting of the AE index one hour ahead using solar wind measurements as inputs. The structures investigated in this work consist of MLPs with two layers of neurons (one hidden layer and one output layer). Figure 3.2 presents a schematic representation of the ANNs employed herein.

The MLPs consist of interconnected processing units called neurons. In the neuron model, a synapse j is connected to the neuron k and a signal x_j at the input of the synapse is multiplied by w_{kj}, the synaptic weight. Based on known input-output data pairs, the network is trained by an iterative process in which the synaptic weights are adjusted. The output y_k of a neuron k can be represented as

$$y_k = \varphi\left(\sum_{j=1}^{n} w_{kj}x_j + b_k\right), \tag{3.1}$$

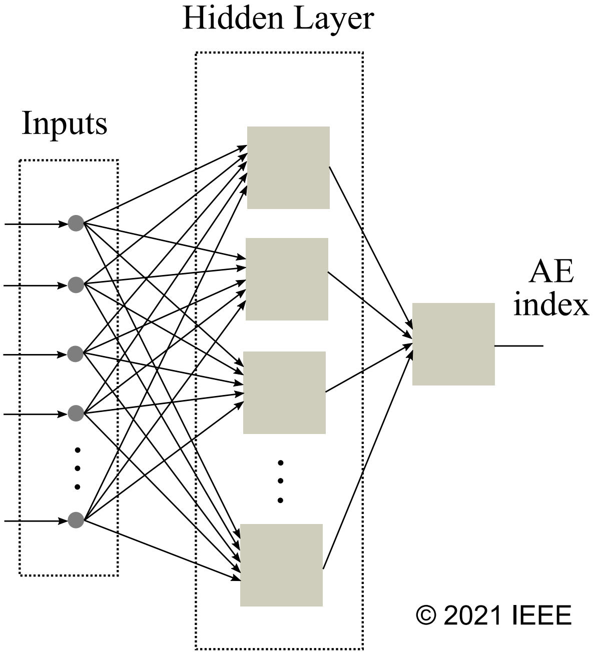

Figure 3.2 – Neural Network model schematic (Ferreira & Borges, 2021).

where n is the number of inputs, b_k is the bias, w_{kj} the synaptic weights and φ is the activation function (Haykin, 2009). In this work, the activation function used on the hidden-layer neurons is the hyperbolic tangent function $tanh(n)$. In the case of the output layer, a linear transfer function is used. The output of the neuron in this case is given by

$$y_k = \sum_{j=1}^{n} w_{kj} x_j + b_k, \tag{3.2}$$

For the training procedure, the Mean Square Error (MSE) is considered as the performance function and the synaptic weights are updated using the Levenberg-Marquardt backpropagation algorithm (Hagan & Menhaj, 1994), presented in Equation (3.3)

$$\Delta \underline{w} = [\mathbf{J}^T(\underline{w})\mathbf{J}(\underline{w}) + \mu \mathbf{I}]^{-1} \mathbf{J}^T(\underline{w}) \underline{e}(\underline{w}), \tag{3.3}$$

where $\mathbf{J}$ is the Jacobian matrix containing the first derivatives of the network errors with respect to the parameters vector $\underline{w}$ (weights and biases), $\underline{e}$ is the vector of network errors and μ is a scalar. If μ is very large, Equation (3.3) gives the gradient descent, and for small values of μ the expression reduces to the Newton method. Since the Newton method is faster near an error minimum, after each successful step (i.e reduction in the sum of the squared errors), the μ is decreased in order to approach the Newton method as quickly as possible (Takalo & Timonen, 1997). This training procedure is applied to all ANNs investigated in this work.

3.1.3 Inspected structures

Variations in the AE index are driven by changes in the solar wind convection electric field, which occur due to fluctuations in the solar wind velocity and IMF. Both parameters govern the efficiency of the coupling between the solar wind and the magnetosphere (Gu et al., 2019). Therefore, this investigation includes as inputs of the networks the B_y and B_z components of the IMF and the solar wind velocity magnitude V. Although other studies have included previous values of the AE index as an input for the model (Gu et al., 2019; Takalo & Timonen, 1997), in this work only solar wind measurements are included. Since the AE index is currently not immediately available, the use of historical values of the AE index as inputs for the ANN would not be possible in a realistic prediction/monitoring scenario (Pallocchia et al., 2008). Additionally, although the investigation presented in Gleisner and Lundstedt, 1997 suggests that proton number density might be an important parameter for the AE index estimations, in this work this parameter is not included, due to the occurrence of datagaps on the 1-hour averaged proton density measurements during the period under investigation.

Table 3.1 presents the first set of network structures investigated in this work, where inputs from the instant t and/or previous instant (i.e. $t - 1\text{h}$) are used to predict the AE index one hour ahead (i.e., the instant $t + 1\text{h}$). It is worth mentioning that this investigation limited the solar wind history to 2 hours prior the prediction time. During tests with longer solar wind history, no significant improvement on the estimates was observed, which agrees to previous studies that suggest that the length of the magnetospheric system memory, as seen by neural networks, is around 100 min (Gleisner & Lundstedt, 1997). In addition to the investigation of the coupling of the AE to the solar wind, an analysis of the solar cycle effects has been included, considering as a proxy the solar radio flux at 10.7cm ($F_{10.7}$ index, Tapping, 2013).

Besides B_y, B_z and V, this study investigated the inclusion of the hour of the day and the day of the year in the set of inputs to account for diurnal and seasonal variation. The hour of the day, H_r, is separated into cyclic trigonometrical components in order to consider the adjacency of the last hour of the day and the first hour of the next day. The same applies for the number of the year, D_n, (depicting seasonal variation), which is also split into two trigonometrical components (Habarulema et al., 2011). Therefore, the *sine* and *cosine* components of H_r and D_n are given by Equations (3.4) and (3.5),

$$H_rS = sin\left(\frac{2\pi \times H_r}{24}\right); H_rC = cos\left(\frac{2\pi \times H_r}{24}\right); \tag{3.4}$$

$$D_nS = sin\left(\frac{2\pi \times D_n}{365.25}\right); D_nC = cos\left(\frac{2\pi \times D_n}{365.25}\right). \tag{3.5}$$

Table 3.1 – Structures under investigation (adapted from Ferreira and Borges, 2021, © 2021 IEEE).

Structure	Inputs	Output
A	$B_y^t; B_z^t$	AE^{t+1}
B	$B_y^t, B_y^{t-1}; B_z^t, B_z^{t-1}$	
C	V^t	
D	V^t, V^{t-1}	
E	$B_y^t; B_z^t; V^t$	
F	$B_y^t, B_y^{t-1}; B_z^t, B_z^{t-1}; V^t, V^{t-1}$	
G	$B_y^t; B_z^t; V^t; F_{10.7}^t$	
H	$B_y^t, B_y^{t-1}; B_z^t, B_z^{t-1}; V^t, V^{t-1}; F_{10.7}^t, F_{10.7}^{t-1}$	

One can note that the temporal information described in Equations (3.4) and (3.5) is not included in the inputs of the networks defined on Table 3.1. To assess the inclusion of those inputs this work investigates also the variants *A, *B,..., *H, which have same inputs of A, B,..., H, but now including the temporal inputs D_nS, D_nC, H_rS and H_rC.

3.1.4 Results and discussions

This work uses solar wind data derived from the Advanced Composition Explorer (ACE) and the Global Geospace Science (GGS) WIND satellite (Gerrard et al., 1998; Lepping et al., 1995). Both satellites orbit at the Lagrangian Point L1 and operate in this orbit since 1997 and 2004, respectively. The idea is to develop the network that can be used regularly with data from the Lagrangian Point L1 as inputs and investigate its applicability on operational AE monitoring/prediction service. The IMF and plasma data used in this work correspond to the hourly averaged ACE and WIND data shifted to the Earth's Bow Shock Nose. The AE index used to train and test the network is processed and generated by the WDC for Geomagnetism at U. Kyoto. The data used in this research has been retrieved from the OMNIweb data service[2].

This dataset used herein starts on the 1st Jan 2008 and goes up to 28th Feb 2018, comprehending approximately 88,900 samples and almost in totality the solar cycle 24. It is important to note that the data from 2018 was included up to February 2018, because this was the most recent AE index data available on the OMNIweb data service at the time this investigation was conducted. From this dataset, the year of 2012 was selected to test the model, due to its close location to the center of the dataset. The remaining data were used

---

[2] https://omniweb.gsfc.nasa.gov/ow.html

for training and validation purposes, being divided in 80% and 20% of the total amount. For the performance assessment this investigation evaluates each structure described in Table 3.1 (and their variants *A, *B,...,*H) in terms of Root Mean Square Error (RMSE), shown in Equation (3.6),

$$RMSE = \sqrt{\frac{1}{N}\sum_{t=1}^{N}(AE_{\text{model}}(t) - AE_{\text{observed}}(t))^2}, \tag{3.6}$$

and correlation coefficient. For each structure, the number of neurons in the hidden layer varied from 1 to 30 and the RMSE and correlation coefficient were registered.

Figure 3.3 presents the results obtained with the validation set for the structures described in Table 3.1. In this case, the temporal information is not considered in the input of the ANNs. The ANN was training using one batch, selecting an initial μ of 0.001 and a maximum number of training epochs equal to 1000. The training is stopped earlier if the performance of the network fails to improve or does not change for 6 epochs of training in a roll. Following the analysis presented in Gleisner and Lundstedt (1997) one can have a close look in the results presented in Figure. 3.3 in order to infer information about the coupling of the AE to the solar wind. However, this analysis has to be carefully done, since the neural networks reveals covariations rather than causal relations, although causality often underlies the covariations (Gleisner & Lundstedt, 1997).

Starting the analysis with the structures A and B, one can observe that the inclusion of the historical information of the solar wind and IMF parameters clearly provided better estimates. The results of the structures E and F suggest that the addition of the solar wind velocity leads to an improvement on the AE estimates, meaning that V has components that vary with AE independently of B_y and B_z.

Previous ANN models for the AE index prediction have not tested the effect of having only the solar wind velocity as input of the network. Therefore, this analysis includes the structures C and D in order to be able to comment on which of the two drivers (V and IMF) has more influence on the AE estimates. Comparing the structures C and D with A and B, one can note that the IMF information clearly dominates. Nevertheless, one can observe that combined, both drivers provided the best results (i.e. structure F).

For all the networks under investigation, the inclusion of historical values of the inputs resulted in an increasing of performance during the training procedure, except for the case where the input is the solar-wind velocity only. This finding evidences the aforementioned magnetospheric system memory. In order to investigate the solar cycle effects on the AE index estimation, the $F_{10.7}$ index was included on the model inputs (structures G and H). The results presented in Figure 3.3 show that the inclusion of this information did not provided any improvement on the results, suggesting absence of influence of the $F_{10.7}$ index on the AE index prediction.

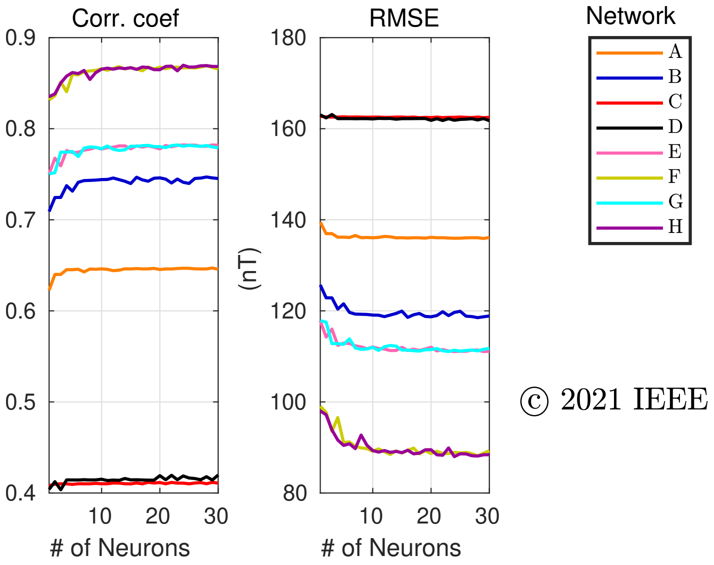

Figure 3.3 – Correlation coefficient and RMSE for the structures described in Table 3.1 (Ferreira & Borges, 2021).

Figure 3.4 presents the performance of the ANNs with the inclusion of the temporal variation information. The results show that the addition of the temporal variability information provides an improvement of up to 10% in the performance of the network for the investigated structures. To the best of the author's knowledge, no previous ANN based model has included this temporal information on the inputs of the network. The results suggest that the information of daily and seasonal variability may be beneficial for the AE index estimation.

As can be noted in Figures 3.3 and 3.4, no significant improvement of performance is observed when the number of neurons exceeds 20. Therefore, based on the results presented in these plots, the Network *F with 20 neurons on the hidden layer was selected as the model for the AE index prediction.

In order to test the performance of the network for the year 2012, this work evaluates the RMSE, normalized RMSE (NRMSE, c. f. Equation (3.7)), Average Relative Error (ARE) shown in Equation (3.8) and correlation coefficient. The AE index for the whole year of 2012 was estimated, leading to RMSE equal to 86.53 nT, NRMSE approx. 0.048, ARE around 0.46 and correlation coefficient of 0.91.

$$NRMSE = \frac{\sqrt{\frac{1}{N}\sum_{t=1}^{N}(AE_{\text{model}}(t) - AE_{\text{observed}}(t))^2}}{AE_{\text{model}}^{\text{max}} - AE_{\text{model}}^{\text{min}}} \tag{3.7}$$

$$ARE = \frac{1}{N}\sum_{t=1}^{N}\frac{|AE_{\text{model}}(t) - AE_{\text{observed}}(t)|}{|AE_{\text{model}}(t)|} \tag{3.8}$$

Aiming at having a better picture of the ANN model performance during different levels

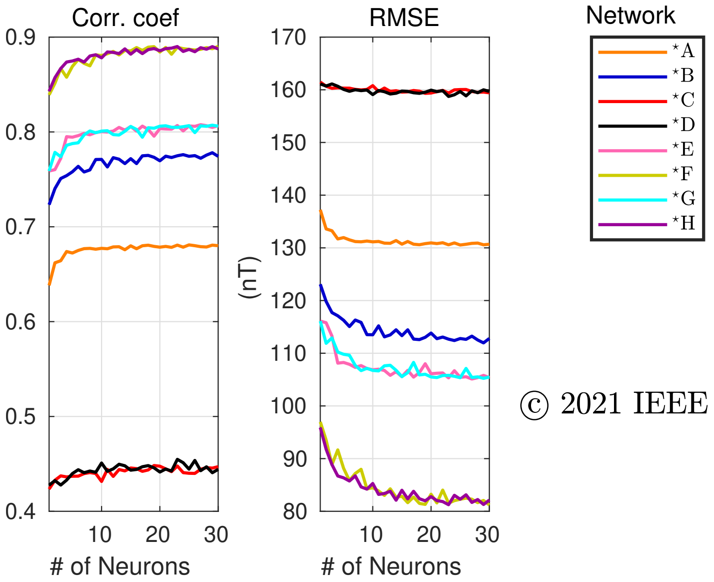

Figure 3.4 – RMSE and correlation coefficient (R) for the structures described in Table 3.1 with temporal information added in the ANN input (Ferreira & Borges, 2021).

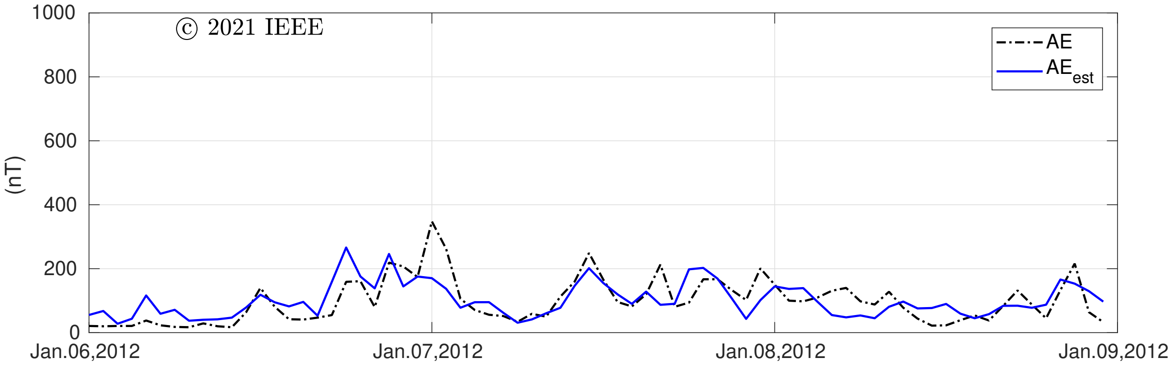

Figure 3.5 – ANN prediction and AE reference values for the quiet geomagnetic activity period (Ferreira & Borges, 2021).

of geomagnetic activity (quiet, moderate and severe), three different periods were selected and the performance of the model was evaluated based on the geomagnetic storms level described in Gonzales et al. (1994). The results are the following:

Quiet activity period This investigation tested the ANN model from the 6 to 9th of January 2012. During this period no geomagnetic storm was registered. Figure 3.5 presents the reference AE index and the values predicted by the ANN model. For this case the obtained RMSE value was 52.77 nT, the ARE of 0.65 and the correlation coefficient between both profiles is 0.65.

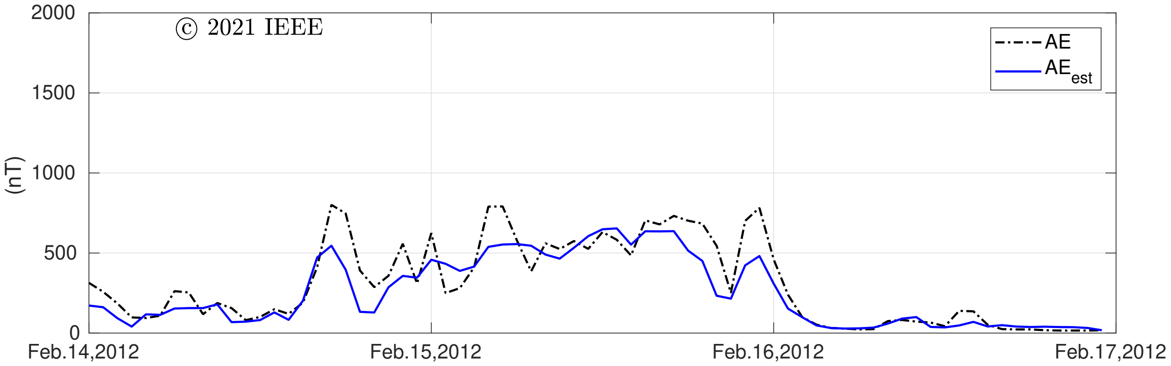

Figure 3.6 – ANN prediction and AE reference values for the moderate geomagnetic activity period (Ferreira & Borges, 2021).

Table 3.2 – Statistics of the *F ANN model results (adapted from Ferreira and Borges, 2021, © 2021 IEEE).

Period	RMSE	NRMSE	ARE	R
2012	86.53	0.048	0.46	0.91
Low activity (Jan 6-9, 2012)	52.77	0.16	0.65	0.65
Moderate activity (Feb 14-17, 2012)	121.86	0.16	0.34	0.91
Severe activity (Mar 9-12, 2012)	179.74	0.11	0.29	0.90

Moderate activity period For this analysis the period from 14 to 17th February 2012 was selected. On the 14th of February a geomagnetic storm was registered, with the Dst index reaching a minimum value of around -60 nT on the 15th of February 2012. Figure 3.6 presents the output of the ANN model together with the reference values. One can note that during the most part of the period the ANN model underestimates the AE values. The RMSE value for this period is 121.86 nT, the ARE is approximately 0.34 and the correlation coefficient is 0.90.

Severe activity period For testing the ANN model during severe geomagnetic activity the period from 9 to 12th of March 2012 was selected. A severe geomagnetic storm was registered on the 9th of March, in which the Dst reached a value of approximately -150 nT. The AE values estimated via the ANN for this period are presented in Figure 3.7. Similar to the behavior of the moderate periods, in this severe period the ANN model also underestimated the AE values, and it was not able to reproduce the strong variations (peaks) observed on the reference AE index. The RMSE for this period is 179.74 nT, the ARE is 0.29 and the correlation coefficient is 0.90. Table 3.2 summarizes the obtained results. Since the RMSE values increase with the level of geomagnetic activity, in order to compare the performance of the model during different periods, normalized RMSE given by Equation (3.7) has been used.

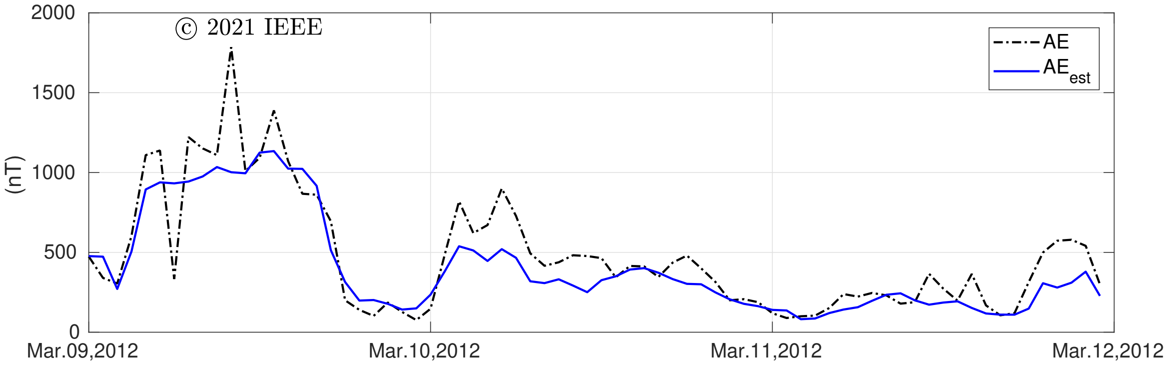

Figure 3.7 – ANN prediction and AE reference values for the severe geomagnetic activity period (Ferreira & Borges, 2021).

The results obtained from the tests of the ANN model indicate good correlation between the estimated AE and the reference values during the analyzed periods, however an inspection at the AE profiles indicate that the model was not able to reproduce strong and rapid variations. A better correlation coefficient is observed during the moderate and severe activity periods when compared to quiet activity period, which may be expected due to the reduced forcing observed in the latter case. Comparing these results with the ones obtained in Gu et al. (2019) and Bala and Reiff (2012), one can note that the proposed model provided comparable performance for the 1 hour ahead prediction of the AE index in terms of correlation coefficient for the three different levels of geomagnetic activity. When considering the whole testing set (the year of 2012), the estimates derived from the proposed model present better correlation with the observations than these previous investigations.

In agreement with the findings of Pallocchia et al. (2008) and Gu et al. (2019), the results indicate that it is not possible to have accurate forecasting of the AE based on IMF and solar wind velocity only. As suggested by Rostoker et al. (1988), there are two different processes involved on the substorm: the directly driven process, in which the energy from the solar wind is directly deposited in the auroral ionosphere and in the ring current and the *loading-unloading*, in which the energy is first stored in the magnetotail for an arbitrary period of time and later deposited in the ionosphere. Due to this, it would be necessary to include information of the internal magnetotail state, which can be done indirectly by including previous values of the AE index (Pallocchia et al., 2008; Takalo & Timonen, 1997). However, since the provisional values of the AE index are not immediately released, the use of historical values of AE is not yet possible on operational monitoring activities.

3.2 Prediction of the LSTIDs activities at mid-latitudes

Previous sections have shown that the occurrence of geomagnetic storms is associated with the excitation of different disturbances in the Magnetosphere-Thermosphere-Ionosphere system. Solar wind energy, captured by the Earth's magnetosphere, is transformed and dissipated, primarily, in the polar upper atmosphere and can lead to significant ionospheric disturbances (Borries et al., 2015). These disturbances include, for example, positive or negative deviations of the ionospheric and thermosphere from the quiet conditions, changes in the thermosphere winds and circulation, increase of ionospheric currents and occurrence of high-latitude ionospheric irregularities.

Nowadays, a considerably large number of applications in aviation, navigation and communication rely on radio frequency transmission, and can be strongly impacted by strong ionospheric perturbations (Borries et al., 2015). Therefore, given the impact these perturbations can have on the transionospheric signals, a good understanding, monitoring and forecasting of such ionospheric disturbances are of the most importance for the development of mitigation strategies. Among the set of ionospheric disturbances observed during geomagnetic storms are the Large Scale and Medium-Scale Travelling Ionospheric Disturbances.

Investigating TIDs may lead to a better understanding of the dominant energy distribution and momentum transfer mechanisms in the ionosphere and thermosphere, which in turn allows the development of warning and mitigation strategies for applications that are impacted by the ionosphere (Altadill et al., 2020). Different strategies have been developed over the years to detect and monitor in near real-time the TIDs, including the use of data derived from ionosondes (Altadill et al., 2020; Reinisch et al., 2018) and from Global Navigation Satellite Systems. However, to the best of the author's knowledge, a methodology to predict LSTIDs activities is still not yet available. In this scenario, this work proposes a new methodology to forecast LSTIDs at mid-latitudes solar wind parameters derived at Lagrangian point L1[3].

3.2.1 Data and methods

3.2.1.1 TID activity index

As presented in Section 2.1.2, LSTIDs can be detected from TEC measurements derived from GNSS measurements. After removing the regular trend of the background TEC of the ionosphere, one can obtain for each satellite-receiver link a perturbation TEC (TEC_p) that allows to identify the LSTIDs. In order to derive the background TEC, different methods

---

[3] Parts of sections 3.2.1.1, 3.2.1.2, 3.2.1.3, 3.2.1.4, 3.2.2, 3.2.3, 3.2.4 have been reprinted from Borries et al. (2023): Borries, C. ; Ferreira, A. A.; Nikyel, G. ; Borges, R. A . A new index for statistical analyses and prediction of traveling ionospheric disturbances. *Journal of Atmospheric and Solar-Terrestrial Physics*, v. 247, p. 1-13, 2023, which is published under the terms of the Creative Commons Attribution License CC BY 4.0 (https://creativecommons.org/licenses/by/4.0).

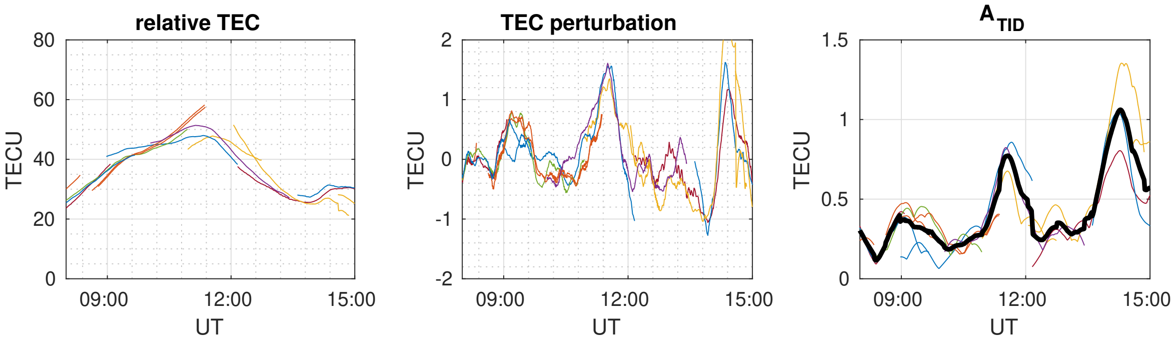

Figure 3.8 – TEC for the SULP station observed during the geomagnetic storm of 17 March 2015: geometry free TEC for all visible GNSS satellites (left panel), TEC_{bp} along each satellite-receiver link, illustrating TID amplitude (middle panel), TID activity index for each satellite-receiver link in colors and the weighted mean in black (right panel).

might be used, which includes moving average, polynomial fit or other estimations of trends, but no significant difference is observed between the methods (Borries et al., 2023).

A new TID activity index (A_{TID}) has been introduced by Borries et al. (2023) with the aim to perform statistical analysis and prediction of TIDs. In this case, the TEC variability in the range of 30 to 60 min is extracted by calculating the difference moving averages with 60 and 30 minutes window size, as presented in Equation (3.9)

$$TEC_{bp}(t) = \frac{1}{T_{30}} \sum_{n=t-0.5T_{30}}^{t+0.5T_{30}} TEC_v(n) - \frac{1}{T_{60}} \sum_{m=t-0.5T_{60}}^{t+0.5T_{60}} TEC_v(m), \tag{3.9}$$

where T_{30} and T_{60} were obtained using 30 and 60 minutes moving averages, respectively, i.e., $T_{30} = 30/\Delta t$ and $T_{60} = 60/\Delta t$, with Δt corresponding to the sampling time. For each time step t, the TID activity index is obtained taking the difference between the maximum TEC_{bp} and minimum TEC_{bp} in a 60 minutes window size centered around t and multiplied by 0.5 , as presented in the Equation (3.10) below (Borries et al., 2023)

$$A_{TID} = 0.5(max(TEC_p(x) \times F(x-t)) - min(TEC_p(x) \times F(x-t))), \tag{3.10}$$

where F corresponds to a Gaussian function applied to reduce the impact of the values that are distant from the 60 minutes window center. Figure 3.8 presents the TID activity index computed for the SULP station (49° N, 24° E) during the geomagnetic storm observed on 17 March 2015. One can note that each panel presents different satellite-receiver links (shown in different colors). In the case of the TID activity index (right panel), the values for each link are combined in order to obtain the A_{TID} for the station (black curve). To combine different links, a weighted average of all A_{TID} estimates at time step t is performed, in which the weights values depend on the elevation angle of the measurements, with high elevation angles leading to higher weights (Borries et al., 2023).

In order to illustrate the capabilities of the TID activity index, a group of 7 stations located in Europe and Africa in the longitude sector ranging from 9 to 30° E was selected and the TID activity index derived for each station during the St. Patrick's Day storm of 2015 was computed. The results can be found in Figure 3.9. For the sake of comparison and better visualization, for each station the TID activity index was multiplied by 10 and summed to the latitude value of the station. The results show how the index (colored bold lines) differs during a geomagnetic storm, when compared to the geomagnetic quiet-days activity, considered here as the average value of the index on the 26 days prior to the storm. The average and standard deviation of the 26 days prior the storm are indicated with the dashed lines and error bars, respectively. In addition, since the TID activity depends on day-night conditions (Borries et al., 2009), the solar terminator is also indicated with yellow asterisks. For all stations, one can observe a significant increase in the TID activity index during the storm when compared to the quiet-days activity levels. The storm time LSTIDs start around noon, and the highest amplitudes can be observed during sunset and post-sunset hours. Also, one can observe a delay from North to South in the initial TID activity index observed at around noon. The observed delay indicates the propagation of the LSTIDs from the auroral region towards the equator.

At low latitude stations ADIS (9° N, 39° E) and MBAR (-1° N, 31° E), the storm-time TID index exceeds the quiet-time levels during the day, but not during night. After the sunset, which is a typical time for the occurrence of Equatorial Plasma Bubbles (EPBs), a clear increase on the TID activity (and its variability) is visible during quiet-times. During this time the storm-time TID activity does not exceed the quiet-time activity (Borries et al., 2023).

3.2.1.2 Solar wind parameters and geomagnetic indices

The main goal in this analysis is to use the aforementioned proposed TID index to forecast TIDs activity in mid-latitudes. It is necessary, however, to know which geophysical parameters or indices do reflect the driving mechanisms for generating such disturbances. This analysis has been done in Borries et al. (2023) by using cross correlation studies of the TID activity index with a list of potential candidate parameters. The study separates two different types of geophysical parameters: geomagnetic indices and solar-wind magnetosphere coupling functions. For the correlation study, 60 geomagnetic storm events from 2001 up to 2017 were selected. The list of geomagnetic storm events and their respective minimum registered Dst index are presented in the Appendix C.

Although the investigation presented in Borries et al. (2023) analyses the correlation with 15 geophysical parameters and the TID activity index, only the results obtained from the correlation with the AE index (see Section 3.1.1) and the Kan-Lee merging electric field will

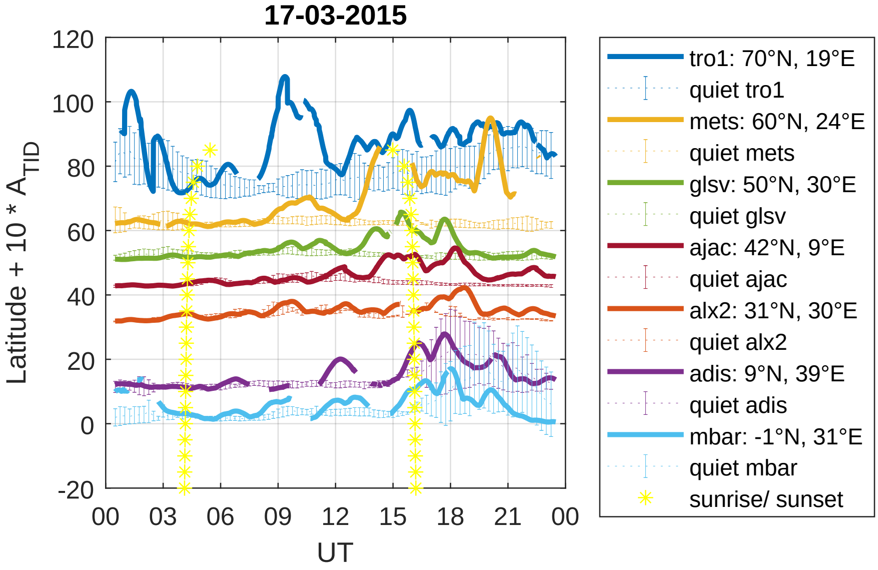

Figure 3.9 – TID activity index for 7 GNSS stations (as listed in the legend) during 17 March 2015. The TID activity index for each station is multiplied by 10 and the latitude integer has been added to illustrate the temporal evolution of the TID activity index at different latitudes. A mean TID activity value and its standard deviation of the preceding 26 days is illustrated with error bars for each station. The two yellow almost vertical lines of asterisks indicate the sunrise and sunset times (Borries et al., 2023).

be presented here for the sake of simplicity. The Kan-Lee merging electric field (E_{KL}) has been chosen due to its good performance in the study conducted in Newell et al. (2007), which investigated the geoeffectiveness of several parameters. The study performed a broad assessment of some solar wind transfer functions and their relation to different geomagnetic indices and parameters (Borries et al., 2023). The Equation (3.11) describes the E_{KL} coupling function

$$E_{KL} = vB_T sin2(\theta_c/2), \tag{3.11}$$

where v is the solar wind speed, $B_T = (B_y^2 + B_z^2)^{1/2}$ is the transverse IMF component, with B_y and B_z corresponding to y and z components of the IMF and $\theta_c = arctan(B_y/B_z)$ is the IMF clock angle.

Figure 3.10 (red dots) presents scatter plots of the maximum TID index of the GNSS station GLSV during each one of the 60 aforementioned geomagnetic storms versus the maximum EKL and AE indices observed in the 18 hours preceding the time of the maximum TID index. One can note positive correlation between both variables. The Hampel filter method is used to identify outliers, which are indicated by the crosses and are excluded from the computations of the regression lines and Pearson correlation coefficients (indicated in each panel). The results show correlation coefficients of 0.79 and 0.72 between the maximum values of the TID activity index and the EKL, and AE index respectively. The same investigation presented in Figure 3.10 has been performed for a set of stations in the European-African sector to verify how the latitude impacts the correlation coefficients. It

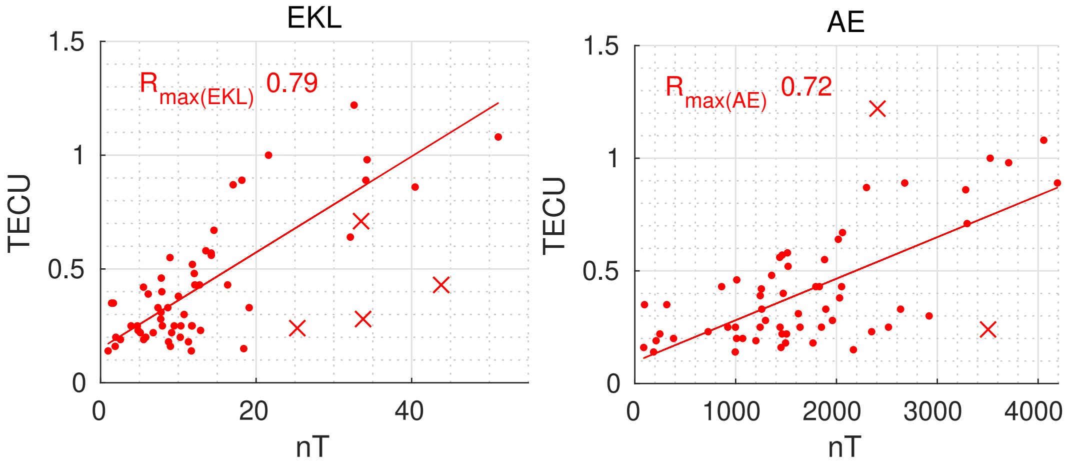

Figure 3.10 – Scatter plots of the maximum TID activity index (y-axis) of the GNSS ground station GLSV during each of the 60 storm events versus the maximum geophysical parameter (x-axis) in the 18 hours ahead of the maximum TID activity index (minimum for IMF Bz). Left: Kan-Lee electric field EKL, right: AE index (adapted from Borries et al., 2023).

was observed that good correlations are observed mainly at mid-latitude stations (Borries et al., 2023). Therefore, in this study the single GNSS station GLSV (50° N, 30° E) is selected as a representative to investigate the TIDs activity at mid-latitudes. The observed good correlations indicate that the EKL and AE indices could be useful for the prediction of the TID activity (Borries et al., 2023). Based on this information, this work investigates the capabilities of different models on the prediction of the TID activity index. Results of this analysis are presented in the following sections.

3.2.1.3 Linear regression model

From the results presented in Figure 3.10, one can note that there is a good correlation between the maximum TID activity index and the maximum Kan-Lee electric field E_{KL} observed in the 18 hours prior to the maximum TID activity index. In addition, the AE index also presents a good correlation of around 0.72, but for the prediction studies, instead of using the AE index, the ANN predicted AE index (NN AE, see Section 3.1) is used, in order to test the usage of the proposed NN model in an application scenario, since the AE index itself takes several days to be officially released, which does not allow its use in near-real time application. The objective in this section is to derive coarse-grained predictions of the A_{TID} based on a linear regression approach. This task is performed as follows: since the correlation investigation presented in Figures 3.10 has been conducted by analysing the maxima values, the maximum EKL and NN AE in a 2 hours intervals ($max_{2hr}E_{KL}$ and $max_{2hr}NNAE$, respectively) is computed. Different intervals could be used, but in this work, an interval of 2 hours was empirically chosen, aiming at the maximizing the prediction performance. The obtained values $max_{2hr}E_{KL}$ and $max_{2hr}NNAE$ are then applied to a linear regression model to predict the A_{TID}.

In order to derive the linear regression model, this investigation uses an approach based on the leave-one-out cross-validation, in which one event from the n geomagnetic storm events presented in Figure 3.10 is used for validation and the other $n-1$ events are used to derive a linear regression model that will be used for the A_{TID} prediction on the validation event. In this case, n linear regression models are generated, each with another storm event kept for validation. This allows to use all the available geomagnetic storms for the validation of the proposed approach. Figure 3.11 illustrates the linear regression fit lines obtained for prediction of the A$_{TID}$ for the geomagnetic storm of November 20, 2003.

For this geomagnetic storm, for example, the following simple linear equations, which are based on the linear regression fits presented in Figure 3.11, have been used:

$$\hat{A}_{TID}(t+n) = 0.152 + 0.021 \times max_{2hr}E_{KL}(t), \tag{3.12}$$

$$\hat{A}_{TID}(t+n) = 0.098 + 0.0002 \times max_{2hr}NNAE(t), \tag{3.13}$$

where $max_{2hr}E_{KL}(t)$ and $max_{2hr}NNAE(t)$ correspond to the maximum EKL and NN AE in a 2 hours interval, respectively, and n represents the 30, 60, ... 180 minutes predictions time, which are then compared to the A_{TID} reference values at t, $t+30$, ..., $t+180$.

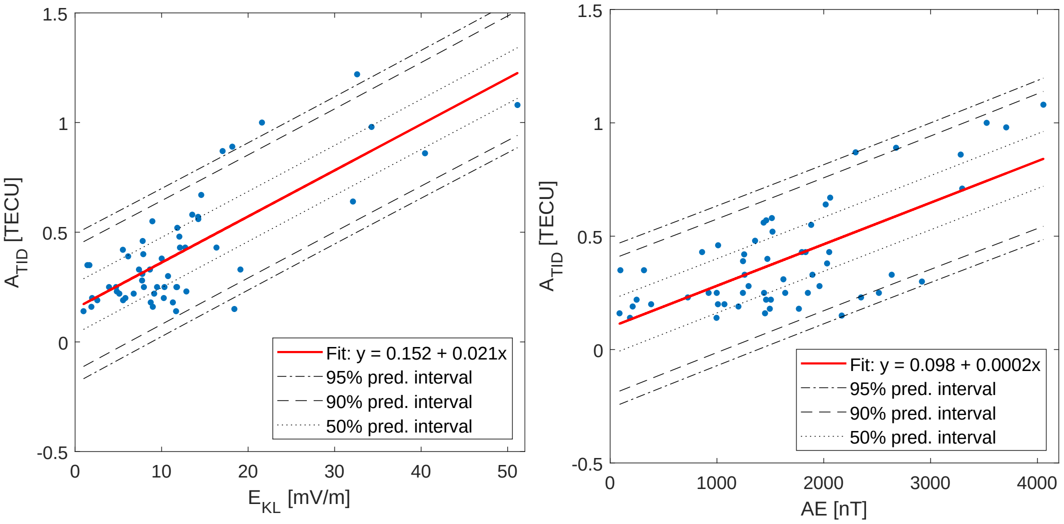

Figure 3.11 – Scatter plot of the maximum TID activity index of the GNSS ground station GLSV during each of the 56 storm events versus: (a) the maximum Kan-Lee electric field E_{KL} in the 18 hours ahead of the maximum TID activity index (Borries et al., 2023) (b) the maximum AE index in the 18 hours ahead of the maximum TID activity index. Outliers indicated in Figure 3.10 are not included.

3.2.1.4 Persistence model

In order to evaluate the performance of the estimates, this work uses as a benchmark the persistence model (Paulescu et al., 2021; Reikard, 2018b), which in this case would assume that a future value of the A_{TID} is equal to the most recent observation, i.e. $\hat{A}_{TID}(t+n) = A_{TID}(t)$. This kind of approach has been used as a benchmark for the prediction of different space weather parameters, such as, solar radio flux, solar-flare activity and the geomagnetic K-index (Devos et al., 2014).

3.2.1.5 Neural network model

As an alternative to the Persistence and the Linear Regression models presented in the previous section, a model based on artificial neural networks is proposed, more specifically, the MLP (Haykin, 2009). A schematic representation of the inputs and the network used is presented in Figure 3.12. This model takes as inputs the Solar Zenith Angle (SZA), to account for the daily variability observed on the LSTIDs activity described in Borries et al. (2009) and historical values of the TID index and the Kan-Lee merging electric field (EKL) described in Sections 3.2.1.2 and 3.2.1.2, respectively. This investigation uses a MLP with two hidden layers (with 256 and 128 neurons, respectively) and one output layer. For both hidden layers, the Rectified Linear Unit (ReLU) activation function has been used and a linear activation function has been employed in the output layer. The network was trained with 600 epochs, learning rate of 1.5×10^{-4} and a batch size equal to 2048. The training/-validation procedure has been performed in the same way as presented in Section 3.2.1.3. Due to the existence of data gaps and outlier events described in Section 3.2.1.3, some of the 60 geomagnetic events presented in Figure 3.10 were removed from the analysis. After removing these events, a total of 54 geomagnetic storms events were available to perform the training and validation. For each event, the day of the storm main phase together with its prior and following days were selected. Therefore, the training procedure includes not only storm days but in some cases, quiet days are also included.

Due to the reduced number of geomagnetic storm events, the performance of the model is evaluated using the leave-one-out cross-validation scheme, in which the network is trained using $n-1$ events and tested in the nth event. In this case, the performance of the model is tested for all events available, which is different from the procedure presented in Kim et al. (2021), that presents the prediction of the ionosphere state during geomagnetic storms using Long Short-Term Memory (LSTM) neural networks. In that study, from a set of 70 geomagnetic storms, 60 are selected for training, 7 events for validation and 3 events for testing. Since in the proposed approach the model is tested in all events, it may present a more comprehensive performance assessment of the model during different parts of the solar cycle and for storms with different features.

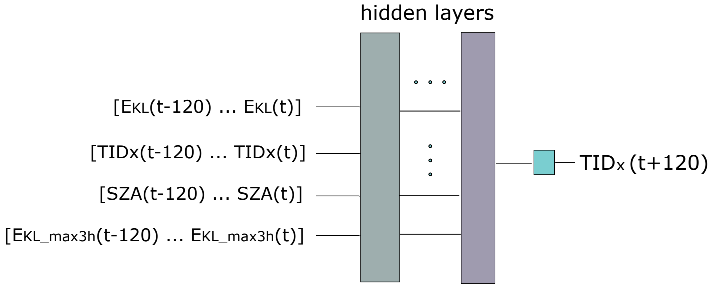

Figure 3.12 – Schematic of the MLP model for the A$_{TID}$ prediction.

3.2.2 Results

In order to illustrate the prediction procedure using different methods, the geomagnetic storm event observed on the 20th of November 2003 has been chosen. This was a strong storm that occurred due to an Interplanetary Coronal Mass Ejection (ICME, J. Zhang et al., 2007) that reached the Earth in the morning of the 20th of November 2003 and lead to a Dst index of approximately -422 nT at 21 UT (Blanch et al., 2005). The TID analysis for this particular storm is presented in Borries et al. (2017b).

Figures 3.13 (a) and (b) show the result of the one-hour prediction using the linear regression model using EKL and NN AE index as inputs for the period from 19th to 21st of November 2003. The A_{TID} computed for the GLSV station during this event reached magnitudes of around 0.8 TECU, indicating a moderate/strong TID activity over the station. For this period, one can note that both prediction models are able to reproduce the increase of the A_{TID} observed during the storm. Rapid fluctuations are, on the other hand, not very well reproduced. In this event, the predictions lead to a Root Mean Squared Errors (RMSE) of 0.16 and 0.14 TECU and Pearson correlation coefficients (R) of 0.84 and 0.76 for the EKL and AE index based estimates, respectively.

Figure 3.13 (c) shows the prediction results obtained from the the persistence model and Figure 3.13 (d) the results of the Neural Network model described in Section 3.2.1.5. For this specific events the correlation coefficient and the RMSE are equal to 0.77 and 0.13 for the Neural Network model prediction and equals to 0.80 and 0.11 for the Persistence model, respectively.

3.2.2.1 LSTID activity detection performance

As presented in Figure 3.13, although the proposed model is not able to reproduce the rapid fluctuations, it can depict fairly well the significant increases of the TID index during storm events. With this in mind, and taking into consideration that, in practice, any regression problem for a continuous variable can be simplified as a classification task by introducing thresholds and separating the range of classes (Camporeale, 2019b), this work evaluates the

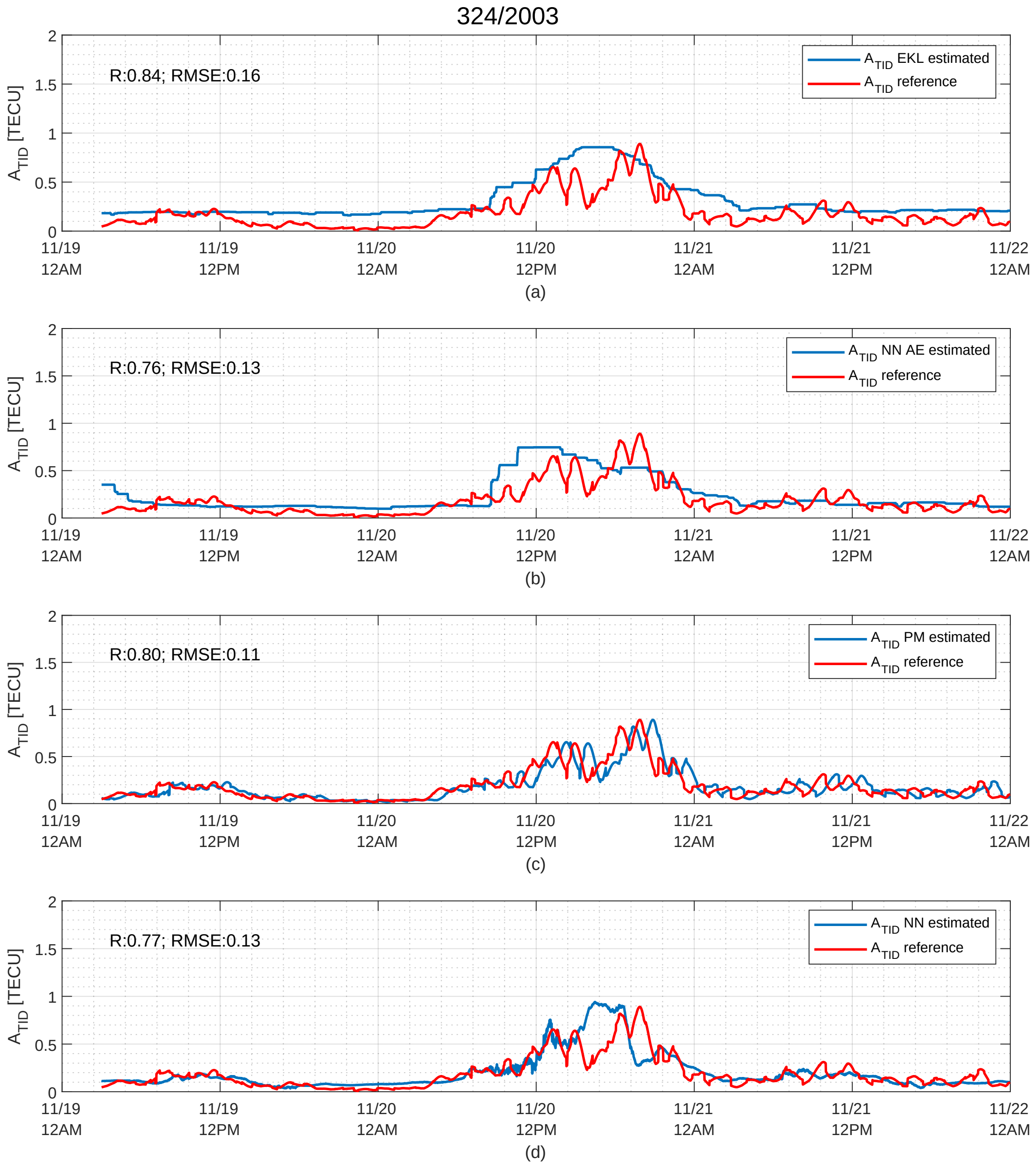

Figure 3.13 – Prediction of the TID activity index during the geomagnetic storm event registered on the 20th of November 2003 using different models described in Sections 3.2.1.3 - 3.2.1.4: a) Linear Regression Model using EKL as input, b) Linear Regression model using NN AE index as input, c) the Persistence Model and d) Neural network based model.

performance of the models on the LSTID activity detection over the GLSV station for all the aforementioned geomagnetic storms events. According to this approach, every prediction point of A_{TID} greater than or equal to the threshold level is considered as a LSTID activity event and prediction points below this threshold are considered as a non-LSTID activity

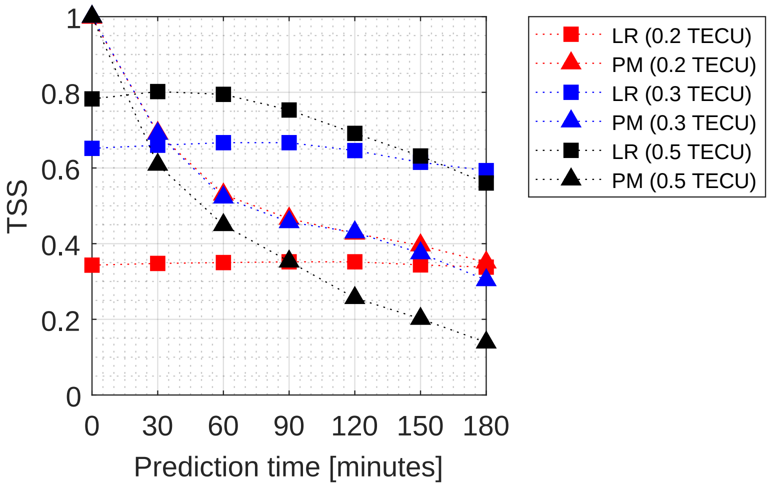

Figure 3.14 – True Skill Score for the predictions based on the linear regression (LR) and persistence model (PM) for different thresholds (in parenthesis) and different prediction times. The threshold determines the criterion to determine the occurrence or not of a LSTID activity event (Borries et al., 2023).

event. This type of classification leads to the following possibilities when comparing to the reference values: True Positive (TP), True Negative (TN), False Positive (FP) and False Negative (FN). In order to evaluate the performance of the model in predicting the occurrence or not of LSTID activity events, this investigation assesses the True Skill Statistic (TSS), which gives the difference between true and false positive rates and is unbiased with respect to class imbalance (Camporeale, 2019b; Detman & Joselyn, 1999). TSS ranges between -1 and 1, with -1 to be interpreted as always wrong predictions (Bobra & Couvidat, 2015), 0 or less indicating a performance no better than random (Detman & Joselyn, 1999) and 1 indicating perfect forecasts. In addition, this investigation uses, as a benchmark, the persistence model, which assumes that a future value A_{TID} is equal to the most recent observation (Reikard, 2018a). Figure 3.14 shows the TSS for different thresholds and prediction horizons for the linear regression model using the EKL as input. One can note the influence of the threshold level of the model performance

Figure 3.15 (a) shows the resulting TSS for all the aforementioned models for a threshold of 0.5 TECU, which corresponds to the 98% percentile of the A_{TID} considering all values and events. The tested prediction lead times range between 0 and 180 minutes.

For the lead time of 0 minutes (nowcast), the persistence model reaches the maximum achievable TSS of 1 because it is identical with the ground truth. For lead times larger than 30 minutes, the TSS of the linear regression model using EKL as input is larger than the TSS of all models under analysis. The TSS for lead times larger than 30 minutes reaches maximum values between 30 and 60 minutes lead times and decreases continuously for larger lead times. The best performance is obtained by the linear regression model using EKL as input for a prediction time of 30 minutes, leading to a TSS of 0.802 (compared to a TSS 0.608 of

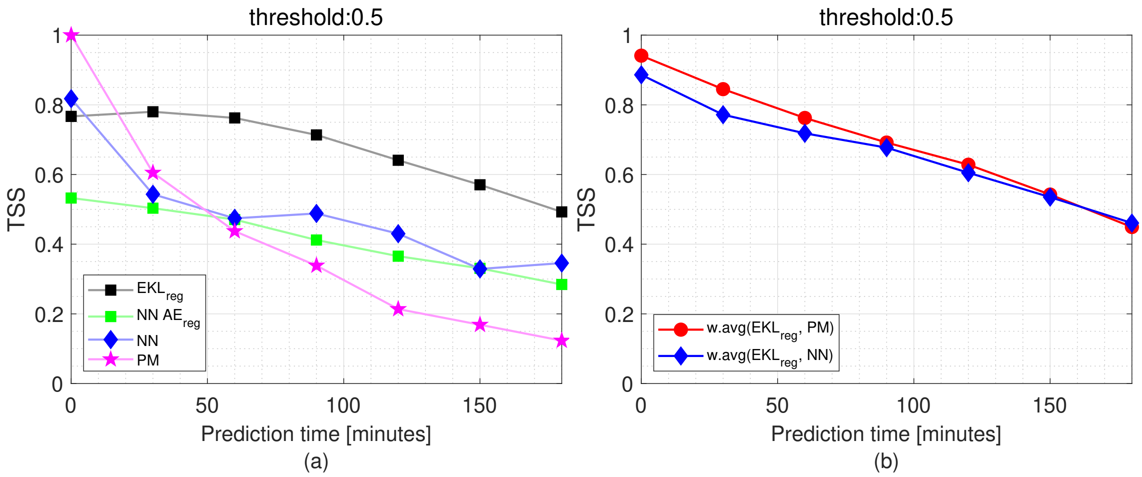

Figure 3.15 – (a) TSS for the different models under investigation, i.e. regression (obtained from EKL and AE), Neural Network and the Persistence models and (b) the TSS obtained from the combination of some of such models using a weighted average scheme.

the persistence model). One can observe from Figure 3.15 (a) that for prediction horizons higher than 60 minutes, the NN based model and the linear regression model using the NN AE index as inputs (blue and green lines, respectively) presented higher TSS when compared to the benchmark (persistence model).

3.2.2.2 Multi-model ensemble

In addition to the models presented in the previous sections, this work also assesses the combination of the models results. A common application of such methodology is the multimodel ensemble, which combines different models in order to increase the performance of a single-model prediction. One basic approach is the linear combination of different methods in order to create a better ensemble forecast (Murray, 2018). Taking probability forecasts as an example, one can combine multiple forecast probabilities outputs from n different models according to $P_{ens} = \sum_n \omega_n p_m$, where p denotes a forecast probability value and ω is the weight value (often chosen in such a way that the sum of all weights equals to 1 (Murray, 2018; Zhou, 2012). Here, the mentioned forecasts could be a number of parameters other than probabilities. In case of this investigation, they correspond to the A_{TID} predictions generated by each one of the presented models.

Different approaches can be used for setting the weights for each model, which may go from simple ensemble averages (which tend to be used in operational forecasting methods, for example) up to nonlinear weighting schemes. Another weighting schemes based on performance metrics can be used in order to improve the forecasts based on the user-end requirements (Murray, 2018). In this work, a weighting scheme that takes into account the performance of each model on predicting the A_{TID} at different levels is adopted. The weights were heuristically chosen in this case. The weighting procedure is performed according to

Equation (3.14)

$$A_{TID}(t) = \begin{cases} 0.8EKL_{reg}(t) + 0.2M_2(t), & \text{if } EKL_{reg}(t) \geq 0.5 \text{ and } M_2(t) \leq 0.5 \\ 0.2EKL_{reg}(t) + 0.8M_2(t), & \text{if } EKL_{reg}(t) \leq 0.5 \text{ and } M_2(t) \geq 0.5 \\ 0.5EKL_{reg}(t) + 0.5M_2(t), & \text{otherwise,} \end{cases} \tag{3.14}$$

where $EKL_{reg}(t)$ corresponds to the prediction obtained from the linear regression model using EKL as input at the time step t, and $M_2(t)$ to the prediction obtained from one of the other models under investigation (i.e. Persistence Model or Neural Network Model). Given its good performance when compared to the other models, the Linear Regression model using EKL as input was included in all multi-model combinations, in an attempt to investigate if such combinations may improve the performance of the single model.

Based on this scheme, new predictions for the A_{TID} index, that will be identified from now on as described in the Table 3.3, are obtained. The TSS for the ensembles investigated in this work are presented in Figure 3.15 (b). The results indicated that the combination of the EKL_{reg} and PM models may improve in about 22% and 8% for the nowcast and 30 minutes predictions, respectively, when compared to the predictions obtained using the linear regression model based on the EKL. For prediction horizons of 60 minutes no changes where observed. Above this prediction horizon, the results indicate that the combination of models did not lead to a performance improvement, but rather to a slightly degradation.

Table 3.3 – Description of the combined predictions using the weight average approach.

Description	**Identifier**
Weighted averaged predictions from the Linear Regression model with EKL as input and the Persistence Model	w.avg(EKL$_{reg}$, PM)
Weighted averaged predictions from the Linear Regression model with EKL as input and the Neural Network Model	w.avg(EKL$_{reg}$, NN)

In order to investigate further the performance of each each model, Figure 3.16 shows the True Positive Rate (TPR), False Positive Rate (FPR) and the True Skill Statistic (TSS) for one hour prediction. From the results, one can clearly note that all models present low FPR, with the NN and PM models presenting the lowest levels (below 1%). The main difference in performance in this cases is lead by the TPR, which in this case is the highest for the predictions obtained from the linear regression model using the EKL as input (EKL_{reg}). For this case the observed TSS was 0.76. The other proposed models presented equivalent performance among them.

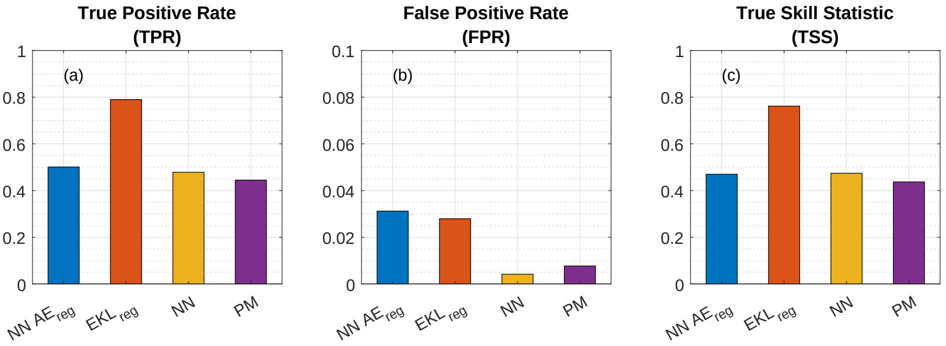

Figure 3.16 – Statistics obtained from the different models for 60 minutes prediction: True Positive Rate (left), False Positive Rate (center) and True Skill Statistic (right).

3.2.3 Discussion

3.2.3.1 TID index and geophysical parameters

Observing the quiet time TID activity index can be useful for understanding its level of noise and uncertainties. Since LSTID is a storm time related phenomenon (or related to the passage of the solar terminator (Cherniak & Zakharenkova, 2018a; Song et al., 2013)) one can expect that during quiet times the TID activity index should be low or peak during the passage of the solar terminator. For the mid-latitude GNSS stations presented in Figure 3.9 one can observe that during quiet times the amplitude of the TID activity index is low, as expected. No increasing of the index during the passage of the solar terminator was observed in this case. For the GNSS stations located at low latitudes (MBAR and ADIS), Figure 3.9 shows strong amplitudes and high variability of the TID activity index during quiet times after the sunset. At these locations and during this time, one can expect the occurrence of EPBs and ionospheric scintillation, which are associated to significant TEC perturbations at different temporal scales (Borries et al., 2023).

Previous studies have shown that AGWs/MSTIDs (Takahashi et al., 2018) can seed EPBs. Modelling results presented in Krall et al. (2011) and investigations using observations from the GOLD mission suggest that AGWs with periods of up to 1 hour can trigger EPBs (Chou et al., 2020; Eastes et al., 2019). Therefore, the periodicity of the LSTIDs investigated in this work and the aforementioned AGWs responsible for the EPBs seeding are similar and can both lead to strong amplitudes on the A_{TID}. In addition, EPBs and its associated irregularities can also generate strong signatures on the A_{TID} computed for low-latitude regions during the evening hours. Separating the signature of such disturbances would require a more sophisticated filtering and analysis (Borries et al., 2023). This is, however, beyond the scope of this investigation which is focused on mid-latitude Europe.

For the high-latitudes (TRO1 station), one can observe also significant high values of the A_{TID} during quiet times. These high fluctuations can occur due to the auroral activity, particle precipitation and patches, which in general have amplitudes higher than the LSTIDs observed in mid-latitudes (Borries et al., 2023). The TRO1 station is typically located inside the auroral oval and during storm conditions it may even be located into the polar cap. Therefore, since the storm driven LSTIDs are usually excited at the equatorward edge of the auroral oval, one can expect that observed high-values of the A_{TID} are not related to such LSTIDs. The occurrence of MSTIDs in the polar region and their correlation with the AE index have also been reported in previous studies, and may include not only equatorward, but also poleward perturbations (Negale et al., 2018; Vlasov et al., 2011; S. Zhang, Erickson, et al., 2019). Separating the effects of this set of disturbances for the high-latitude region would also require a more detailed analysis, which is also out of the scope of the present work. By analyzing Figure 3.9, one can observe that for the geomagnetic storm registered on March 17, 2015, the A_{TID} shows a significant increase for all stations. At mid-latitudes, an increase is observed from 9 to 12 UT, followed by a second increase from 14 to 19 UT, which is consistent with the investigation of the LSTIDs for the same event presented in Borries et al. (2016b), Liu et al. (2019), Lu et al. (2020), and Zakharenkova et al. (2016). These results confirm that the proposed index may be a useful tool for investigation of LSTIDs in mid-latitude Europe.

3.2.3.2 LSTIDs prediction

The analysis presented in Section 3.2.2 shows different approaches for the prediction of LSTIDs, which were based on linear regression, neural networks and multi-model ensembles. When predicting the TID activity index, one has to take into account that the index is subject to fluctuations that are not directly related to the solar wind conditions or perturbations reflected in the geomagnetic indices. Such fluctuations can be seen in Figure 3.13 and since it is not completely understood the main source of such fluctuations, the LSTIDs prediction model aims at predicting the maximum achievable TID index, A_{TID}.

Therefore, what is shown as blue lines in Figure 3.13 corresponds to an upper envelope for the A_{TID}. In this case, typical model evaluation metrics such as RMSE and correlation coefficient may be not ideal for evaluating the models' performance. Instead, one can look for the problem from a classification point of view and therefore, the computation of skill scores based on the contingency table might be better suited for the case. Such performance evaluation has been successfully applied to different space weather modelling and prediction activities (e.g. Bloomfield et al., 2012; Mukhopadhyay et al., 2020; Verkhoglyadova et al., 2020; Welling et al., 2018). In this analysis, the TSS has been used due to its advantages when evaluating data-sets with class imbalances, which is the case for the LSTIDs, since the majority of data does not contain increased LSTIDs activity.

In order to apply this methodology, one has to define the event detection. In this case, different thresholds have been tested based on the statistical occurrence of the A_{TID} magnitudes. The results presented in Figure 3.14 show that the model performance is significantly affected by the threshold definition. In addition, it has been observed that the threshold of 0.2 TECU might be too low for the evaluation of the linear regression models using the EKL as input, which can be easily observed by analysing Figure 3.10. As observed, the regression line crosses the y-axis at $y = 0.152$ and the 50% prediction interval reaches up to around 0.25. That means that even during quiet times, the results of the model would fluctuate around the threshold of 0.2 TECU, leading to detection errors. This shows that the prediction model is rather restrictive, showing most of the time the chance of getting a LSTID with 0.2 TECU amplitude. A recent study by Thaganyana et al. (2022), which shows an analysis of TIDs from mid to large scales in the European-African sector travelling from one hemisphere to the other, shows that this restriction is not wrong (Borries et al., 2023). The study shows that the disturbances occurred during geomagnetically quiet days were associated to tertiary AGWs from the dissipation of secondary AGWs excited by local body force created from breaking mountain waves (according to the theory of Becker and Vadas (2020)).

From Figure 3.14 one can also observe that the best performance for the LSTIDs activity prediction is obtained when larger thresholds are adopted, with the best performance obtained for a threshold of 0.5 TECU. Therefore, it indicates that the model is best suited for prediction of moderate/strong TID activity prediction and for lead prediction times between 30 and 60 minutes. Assuming that the LSTIDs are excited at the equatorward boundary of the auroral oval (Borries et al., 2016a), which is on average at about 65-70° N in the European region, and they propagate with a speed of 680 ms^{-1}, the LSTID would need 40-54 minutes to reach the GNSS station GLSV at 50°N, which has been used for the demonstration of the prediction model. This matches well with the derived best lead times of the prediction model and it also shows that the model assumes an immediate impact of the solar wind on the ionosphere. This estimation of the LSTID propagation time would only apply for the beginning of the geomagnetic storm. Later in the course of the storm, when the auroral oval expands, the LSTIDs need less time to reach the mid-latitude GNSS station (Borries et al., 2023).

When comparing all the investigated models with the linear regression model using EKL as input (EKL_{REG}) one can note a clear difference in the performance. For the one hour predictions, the EKL_{reg} model is followed by the NN, NN AE_{REG} and PM, respectively. Although all the models presented a low FPR, the EKL_{REG} presented the highest TPR, which translated in this case for a high TSS. It is important to highlight that for prediction above 60 minutes, all models presented higher performance than the persistence model. The NN model (described in Section 3.2.1.5) presented better results than almost all the other models for predictions above 60 minutes. Its lower performance when compared to the EKL_{REG}, however, may be attributed to the higher level of underestimation on this model when higher levels of A$_{TID}$ is observed, which leads to a decrease of TPR. One of the possible causes for the underestimation could be the low number of storms with significantly high A$_{TID}$ values, which could interfere on the NN estimates. Also, due to different characteristics and features of each geomagnetic storm event, the amount of geomagnetic storm events used to train the model may not be representative enough.

The ensemble models did not improve significantly the prediction results above 60 minutes. Below this time, however, improvements have been observed, which suggests that the combination of the EKL$_{REG}$ and the PM could be useful for short-term predictions of the LSTID activity level.

3.2.4 Summary

This chapter is devoted to investigate and propose prediction methods for two specific SWe phenomena, namely the substorms (by mean of the AE index investigation) and the Large Scale Traveling Ionospheric Disturbances (LSTIDs).

The first part of the chapter analyses different arrangements of feed-forward ANNs including distinct information related to the IMF, solar wind velocity and solar cycle (diurnal and seasonal variations) for the forecasting of the hourly-averaged AE index. During the selection for the most suitable ANN model arrangement, different numbers of neurons on the hidden layer, ranging from 1 to 30, were tested based on the analysis of the RMSE. The structure containing 20 neurons was chosen. The model was tested during different periods of year of 2012, and presented a good correlation with the reference AE values. However, the ANN model using only IMF and solar wind velocity as input was not able to reproduce strong variations, mostly underestimating them. These results are in agreement with other previous research findings, indicating that information of the internal magnetotail state should be included in the input. In order to have better quantitative predictions, it is necessary to include information from the dynamics of the magnetosphere to account for the loading-unloading processes, which impose challenges for operational prediction purposes. The results show that the inclusion of the temporal information provides an improvement of up to about 10% on the model performance. It suggests that this information, which to the best of the author's knowledge has not been included in others ANNs based models for estimation of the AE index, might be beneficial for the AE index estimation studies. Based on this, an extensive analysis of the inclusion of temporal information on different ANN based models is recommended, in order to quantify its influence and to infer the importance of the different temporal components on the AE index estimation. This study also suggests an absence of solar cycle influence (assessed herein by means of the F$_{10.7}$ index) on the estimates. In addition, this investigation has evidenced that although the IMF and solar wind velocity provide better performance when combined, the IMF information is dominant when compared to the solar wind velocity for the estimation of the AE index, which is not often highlighted in the discussions of the solar wind forcing of the auroral electrojets.

In the second part of the chapter, a new methodology for predicting LSTIDs activities over Europe is proposed. The investigation is based on a new index proposed by Borries et al. (2023) for investigating LSTIDs generated during geomagnetic storms. The index is based on an extension of the commonly used approach for TID detection, neglecting the phase information of the waves for the purpose of better indication of the amplitude level of the disturbances. It enables statistical investigation of such disturbances and their relation with solar and geomagnetic parameters. Correlation studies revealed that A_{TID} magnitudes at mid-latitude Europe are well correlated with solar wind parameters like the Kan-Lee merging electric field. Hence, different prediction models for storm induced LSTIDs based on only solar wind observations have been proposed and investigated. The set of investigated models includes linear regression models, ANN based model and also multi-model ensembles. The results show that proposed models have a good performance on LSTIDs activity predictions at mid-latitudes, with all the proposed models presenting better performance than the persistence model for predictions beyond one hour. For prediction times of 30 minutes, the use of multi-model ensembles may also help to improve the estimates. The results presented here contribute to a better understanding of the drivers of LSTIDs for their prediction activities and monitoring at mid-latitude Europe.

4 Impact of Space Weather Events on UHF Satellite Communications

Parts of this chapter have been published as: Ferreira, A. A., Borges, R. A., Reis, L. R., Borries, C., Vasylyev, D., Investigation of Ionospheric Effects in the Planning of the AlfaCrux UHF Satellite Communication System. **IEEE ACCESS, v. 10, p. 65744-65759, 2022, under the terms of the Creative Commons Attribution License CC BY 4.0 (https://creativecommons.org/licenses/by/4.0).**

4.1 Introduction

As introduced in the previous chapters, the ionosphere may have strong impact on the signals that propagate through, or are reflected by, it. These effects, which include absorption, refraction, signal group delay, phase advance and Faraday Rotation may be taken into account for some applications, such as, Satellite Communication (SATCOM), GPS single frequency navigation, HF over-the-horizon radar, satellite altimetry and space-based radar (Singh & Bettenhausen, 2011). The most important frequency ranges for communications, meteorological satellites, remote sensing and precision navigation and timing are the Ultra High Frequency (UHF), the Super High Frequency (SHF), and the Extremely High Frequency (EHF) (Pelton & Madry, 2017).

The lower bands (i.e. UHF, 300 - 3000 MHz) are well suited for transmitting signals to mobile services (such as vehicles and other applications), since it has the advantage of not requiring direct line of sight to the receiving antennas, unlike the SHF (3000 MHz to 30 GHz) and especially the EHF (above 30 GHz) bands. In addition, the UHF bands are not subject to any significant lower atmospheric disruptions, even with high rain rates, snow or fog (Pelton, 2017). Nevertheless, since all of the aforementioned ionospheric effects are inversely proportional to the squared frequency of the signal, one can expect that for UHF band signals some of ionospheric effects may be significant.

It is important to mention that although the UHF classification according to the International Telecommunications Union (ITU) encompass the spectrum range from 300 to 3000 MHz, which includes the GNSS signals frequency, this investigation[1] focus on the bottom part of the UHF spectrum, more specifically on the frequency around 437 MHz. This frequency is commonly applied on satellite communications due to the possibility of using

---

[1] This chapter has been reprinted from Ferreira et al. (2020): Ferreira, A. A., Borges, R. A., Reis, L. R., Borries, C., Vasylyev, D., Investigation of Ionospheric Effects in the Planning of the AlfaCrux UHF Satellite Communication System. *IEEE ACCESS, v. 10, p. 65744-65759, 2022*, which is published under the terms of the Creative Commons Attribution License CC BY 4.0.

an amateur radio channel, and it is the frequency used in the AlfaCrux mission, which is described in details in the following section. Typically, CubeSats operate in Very High Frequency (VHF), UHF or S-band (2 - 4 GHz, Cristóbal & Emami, 2019).

4.1.1 The CubeSat standard

A nanosatellite, a small satellite weighting less than 10 kg, is a spacecraft built at relatively low cost, which is able to serve not only to education purposes, but also space services and applications. Among the nanosatellites category, the CubeSat has appeared as a good opportunity for universities to approach space research. They are intended to be built in short time frame, at relatively low cost, and they make significant use of state-of-the-art commercial-of-the-shelf (COTS) technologies (Aguado-Agelet et al., 2019).

The CubeSat standard was developed by the California Polytechnic State University (CalPoly) and the Space Systems Development Laboratory of Stanford University. The term *CubeSat*, refers to a category of small satellites built in a modular fashion and have as a basic unity a cube of dimensions 10 cm×10 cm×10 cm with the mass up to 2.0 kg (Johnstone, 2020). This basic unity is also called the CubeSat Unity (1U, Johnstone, 2020; Popescu et al., 2016). These modules can be combined to form CubeSats in different sizes (1U, 2U, 3U and 6U) that can be launched as a secondary payload reducing the launching costs and allowing universities to conduct space science experimentation (Popescu et al., 2016; Saeed et al., 2020). CubeSat missions may consist of only one single satellite operated individually or it can contain a cluster/swarm of CubeSats. In the former case, CubeSats collect data for an specific scientific experiment, perform a basic data processing and transmits these data via a radio transceiver to a ground station, where these data are further processed and analyzed. In the latter case, satellites may establish inter-satellite communication links and share the collected scientific data along with the ancillary data (such as positioning and timing), allowing the satellites of the cluster to perform a joint/distributed processing of data (Popescu et al., 2016).

In this context, the AlfaCrux mission conducted by the University of Brasilia (UnB) and coordinated by the Laboratory of Simulation and Control of Aerospace Systems (LODESTAR) is proposed. The mission was named after the Alpha Crucis star, which is among the brightest stars in the sky and the brightest star in the southern constellation Crux (the Southern Cross). The motivation to choose AlfaCrux as the mission's name comes from the fact that the Southern Cross is the best-known constellation among the ones visible in the southern hemisphere. The Alpha Crucis star appears in the Brazilian flag, in the Brazilian coat of arms and it has a special importance in navigation and orientation (LODESTAR, 2022).

4.1.2 Mission Description

The AlfaCrux mission is an amateur radio and educational mission with in-orbit technological demonstration and high-level tasks, which include planning, management, and risk analysis along of its life cycle. The AlfaCrux CubeSat was launched on the 1st of April 2022 from the Space Launch Complex 40 at Cape Canaveral Space Force Station in Florida by the Falcon 9 Transporter-4 mission into a Sun-synchronous orbit at 500 km. The main motivation behind the mission launching is to provide an opportunity for space educational training together with scientific outcomes in the context of small communication satellite missions. In addition, the mission is also motivated by another critical need in our society, which is to provide reliable narrowband communication coverage. In the context of satellite communications, the term narrowband refers to the UHF-, L- and S-bands, where the bandwidth is limited. The lower frequency bands (300 MHz to 4 GHz) can be advantageous when compared to the higher frequency bands due to their better penetration into buildings, foliage and due to their lower level of attenuation in adverse weather conditions when compared to other higher-frequency bands (Gündüzham & Brown, 2015). These pros are important when trying to establish a satellite communication link in areas of tropical forest, such as the Amazon regions, which are characterized by a considerably dense foliage, and high level of humidity (Reis, 2021; Reis et al., 2020). In addition, narrowband satellite communication can meet the requirements of data collection systems in remote areas lacking infrastructure, such as undeveloped/uninhabited areas and areas devastated by natural disasters (Borges et al., 2022).

The AlfaCrux Cubesat's payload, a Software-Defined Radio hardware (SDR), is responsible for two main services: a digital packet repeater at 437.225 MHz based on AX.25 protocol, and a store-and-forward service at 437.125 MHz using Gaussian Minimum Shift Keying (GMSK) modulation, which provides good compromise between speed and bandwidth. GMSK has no phase discontinuities and, therefore the side lobes of signal spectrum are reduced. It not only minimizes channel interference, but also provides efficient use of the spectrum and enables high efficiency. The AlfaCrux mission consists of a bidirectional, low-rate, short-message-based store-and-forward system between the users on the ground and the satellite. The system users can access, via internet, the data collected by the AlfaCrux sensors and also send information to the satellite. When the store-and-forward service is available, the satellite send a beacon which is received by a terrestrial user, which send the available information to the satellite. The satellite then can forward the information in real time to another user terminal or ground station in its area. This can be useful for different applications, such as, communication with weather stations in remote areas, environmental sensors, communication in areas affected by disasters, among others (Borges et al., 2022).

Although advantageous in the aforementioned situations, the narrowband SATCOM has the disadvantage of providing low-rate data transfer, due to the limited bandwidth. Besides that, trans-ionospheric signals transmitted in these bands are more susceptible to the effects of the ionosphere. In the case of the AlfaCrux mission, the satellite orbits at a height of around 500 km, and therefore its signals cross the peak of the F_2 layer of the ionosphere.

Brazil is located in the low latitudes, a region with different strong ionosphere features like the equatorial ionization anomaly (De Paula et al., 2003) or ionospheric plasma bubbles and irregularities (Sobral et al., 2002). Considering these conditions, the ionospheric impact on the AlfaCrux's signal propagation has to be treated carefully during the mission design. Since it orbits in LEO, it was expected for the satellite to have up to five contacts per day with the command station with less than 12 minutes duration each (Cristóbal & Emami, 2019). It is important to highlight, however, that the number of contacts in which the communication task can be satisfactorily performed may be influenced by the elevation angle, reducing even more the number of opportunities to perform the communication task. Due to those scarce opportunities for signal transmission, the understanding of the ionosphere impact on the signal propagation is essential for planning and efficient use of the communication channel. In this scenario, the next sections will investigate the impact of some of these effects on the satellite communication link, aiming at including them in the AlfaCrux link budget computation. More specifically, the Faraday rotation and ionospheric scintillation effects are investigated. In addition, this work proposes a new methodology to assess the risk of communication outage due to ionospheric scintillation, which can be an useful tool for the UHF SATCOM missions planning and design.

4.2 Faraday rotation

The antennas installed in the CubeSats can be either linearly or circularly polarized. In case of linearly polarized antennas, keeping the polarization of the signal across the propagation path is crucial in order to ensure its reception. In this context, the major problems in matching the transmitter and receiver antenna polarizations occur due to ionospheric effects, more specifically due to the Faraday rotation (Barbarić et al., 2018). This effect corresponds to a rotation of the polarization plane of linearly polarized radio-waves propagating in the ionospheric medium and exposed to the action of the geomagnetic field. The FR is inversely proportional to the squared frequency of the signal and may impact different applications (e.g. spaceborne synthetic aperture radar (SAR) systems, and microwave radiometers, Jehle et al., 2005; Singh & Bettenhausen, 2011). Figure 4.1 presents a schematic representation of the FR, in which a incident electromagnetic field E_i is rotated an angle θ_F, leading to a transmitted electromagnetic field E_t.

In addition to the frequency, the geomagnetic field and the electron density in the ionosphere are the geophysical quantities that influence the magnitude of FR angle. This effect

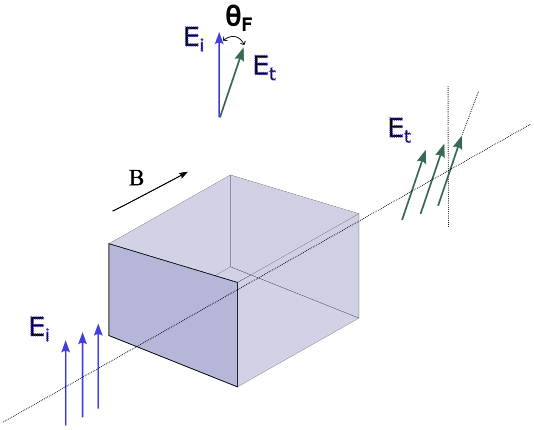

Figure 4.1 – Schematic representation of the Faraday rotation angle θ_F (after Suresh et al., 2020).

can be expressed as (Lawrence et al., 1964; Singh & Bettenhausen, 2011; Wright et al., 2003):

$$FR[radians] = \frac{e^3}{8\pi^2 m^2 c\varepsilon_0 f^2} \int N_e \, B \cos\psi \, ds, \tag{4.1}$$

where c is the free-space velocity of light, e is the electron charge, m is the electron mass, ε_0 is the permittivity of free space, f is the frequency of the signal, N_e is the electron density, B is the magnetic field. The angle ψ is the angle between the electromagnetic wave vector and Earth's magnetic field vector.

The integration in (4.1) is performed along the propagation path with line element ds. The calculations of the FR can be simplified if one neglects the finiteness of the Earth or ionospheric shell curvatures. Additionally to this, the refractive bending of the signal ray at high zenith angles, θ_o (see Figure 4.2), of a ground-based receiver is neglected (nadir angles of the communication satellite). One can express the slant path element in Equation (4.1) as $ds = \sec\theta_o dh$. Here, dh is the corresponding vertical line and the integration can be performed from altitude of the ground station, $h_r = 0$, up to the satellite altitude h_s (Wright et al., 2003).

Further simplification of Equation (4.1) is obtained if it is assumed that the external magnetic field B is constant. In this case, the angle of rotation is proportional to $\int N_e dh$, i.e., to the total electron content (TEC). Equation (4.1) can be approximated as:

$$FR[radians] = \frac{K}{f^2} \cdot B \cos\psi \sec\theta_0 \cdot TEC, \tag{4.2}$$

where the magnetic field factor K is obtained considering a constant height of 400 km, (Wright et al., 2003) and it is a constant of value 2.365x10^4[$\mathrm{A \cdot m^2/kg}$] in S.I. units.

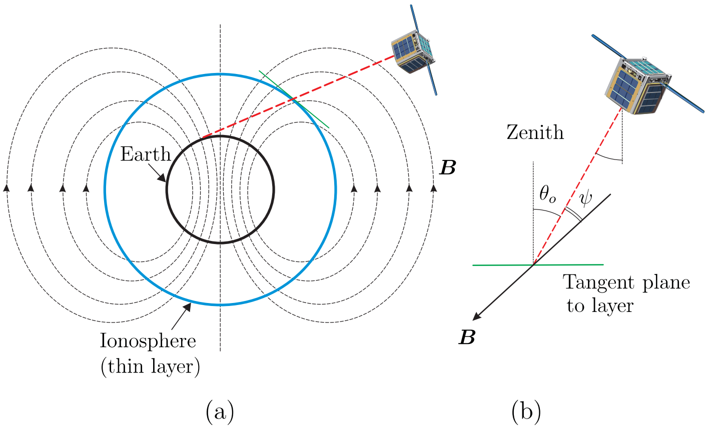

Figure 4.2 – Communication schematics with a CubeSat satellite (a). Under the assumption of small zenith angle θ_o of the receiver, the geometry presented in (b) can be applied for the derivation of (4.2). Here the zenith angle θ_o is constant along the communication link and it is assumed that the angle ψ is formed between the signal propagation direction and the direction of the magnetic field $\boldsymbol{B}$ (Ferreira et al., 2022).

4.2.1 Variability of Faraday rotation effect

For investigation of the temporal and seasonal variability of the FR, the location of Brasília, Brazil (15° 48′ S, 47° 51′ W) has been chosen and the FR effect for the years of 2015 and 2018 has been analyzed. These years correspond to the maximum and minimum periods of the solar cycle 24, respectively. The purpose of choosing two different periods is to illustrate the contribution of the solar cycle on the FR variation.

In order to account the attenuation due to the polarization effects, this work also considers the polarization loss factor (PLF) given by PLF$=\cos^2\theta$, where θ is the angle between the polarization vectors of the signal and the receiver (Galuscak & Hazdra, 2006). A PLF equals to zero corresponds to a complete misalignment of polarization planes of the sent and received signal. Figure 4.3, left panel, presents the results for the year of 2015. One can note clear seasonal and daily variability of the polarization loss factor. During the whole year it is observed a decreasing on the PLF on the afternoon-night hours (from around noon to 2:00 LT) from January to May and from October to December, indicating that during these periods a higher signal attenuation due to the depolarization is expected. From June to September, on the other hand, one can note a high PLF during the whole day, indicating that for this time of the year (which corresponds to the winter in the Brazilian region), a reduced attenuation due to the depolarization is expected.

In addition to this, one can note that the two periods of low PLF values (January to May and October to December) do not exhibit the same magnitude, with the first period having more impact on the signal attenuation than the second one. This might be related to the variation due to the solar cycle, which can lead to a lower level of ionization and, consequently, to a lower attenuation due to the FR effect.

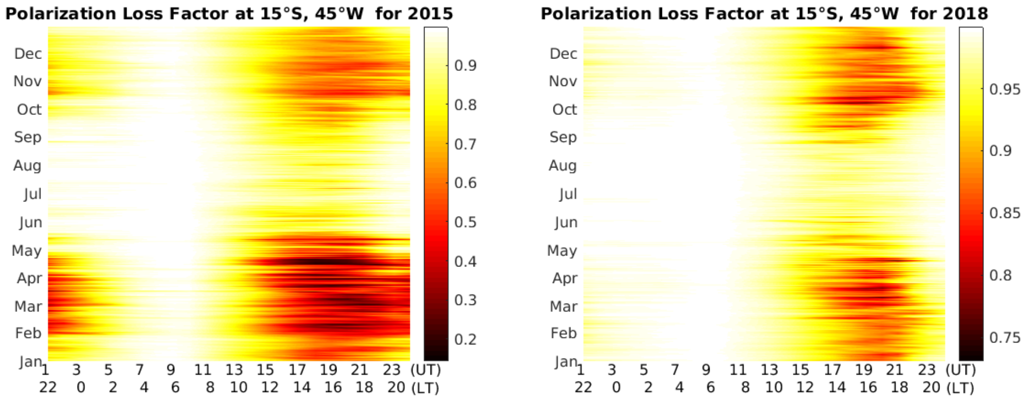

Figure 4.3 – Polarization loss factor at 15°S and 45°W for 2015 (left panel) and 2018 (right panel) (Ferreira et al., 2022).

Figure 4.3, right panel, shows the PLF for the year 2018. As mentioned above, the year 2018 corresponds to a solar cycle 24 minimum, and as a consequence one can expect a lower level of ionization of the ionosphere. By comparing both panels on Figure 4.3, one can clearly note a significant difference on the magnitude of the PLF. Although there are two peaks of low PLF in 2018 (from January to May and October to December, in the similar way as they appear in 2015), in this case the PLF does not reach values below 0.75. This means that the impact of the ionosphere on polarization is less severe for the year 2018 during the solar minimum in comparison to the year 2015 of the solar maximum. Also, the lower PLF values are concentrated in a considerably low interval during the day (from around 12:00 until 20:00 local time).

The median value of the Faraday rotation exhibits regular diurnal, seasonal and solar cyclical variations that can be predicted and, therefore, compensated by a manual adjustment of the polarization tilt angle at the ground station antennas. However, this regular behaviour can be significantly changed as a result of space weather events, such as Storm Enhanced Densities (SED) and Travelling Ionospheric Disturbances (TIDs, Oberoi & Lonsdale, 2012). Also, intermittent changes of FR angles of very-high frequency (VHF) signals have been associated with strong and fast scintillation occurring at locations near the crests of the Equatorial Ionization Anomaly (ITU, 2019). In order to analyze and to illustrate this influence, the geomagnetic event that occurred in the maximum phase of the solar cycle 24 has been chosen as a case study.

Figure 4.4 presents the FR and the PLF for the St. Patrick's day geomagnetic storm that took place on 17 March 2015. This event occurred during a solar maximum period and lead to significant FR levels. The maximum solar radio flux registered for this storm was around 138 solar flux units (sfu). The FR and PLF values are shown for a linearly polarized signal propagating in vertical direction to the ground (θ_o=0). As presented in Figure 4.4, right panel, the polarization orientation may change to the orthogonal one for some regions of the globe. Hence, in these regions the communication can be completely interrupted if the linearly polarized receiver antennas are used.

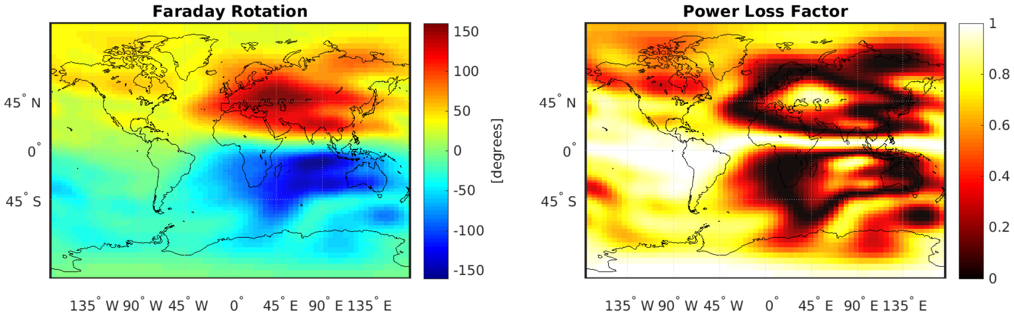

Figure 4.4 – Left panel: Faraday rotation at 12 UT for a 437 MHz signal frequency for St. Patrick's day storm (March 17, 2015), Right panel: PLF associated with the FR presented in the left panel (Ferreira et al., 2022).

4.2.2 Faraday rotation for slant propagation paths

The previous investigation considered primarily the situations when the signal approaches the ground receiver from near zenith direction. For example, Figure 4.4 is calculated for the case of vertical propagation of the signal ($\theta_o = 0$). For the zenith angles in the range $\theta_o \in [0°, 60°]$, one can use Equation (4.2) to estimate the FR for slant propagation paths. However, for higher values of the zenith angle one should account for the refractive bending of the signal radio rays caused by the ionospheric layer. Thus, one should use the general formula given in Equation (4.1) along with the proper ray-tracing algorithm for calculation of the bent propagation paths.

In this investigation the FR angle for slant communication links is visualized by mapping the calculated values on the sky plot for specified ground receiving stations. In this work four GNSS receiver ground stations located in Brazil are considered, namely BOAV (Boa Vista, 2°50′ N, 60°42′ W), BRAS (Brasília, 15° 47′ S, 47° 52′ W), CUIB (Cuiabá, 15°33′ S, 56°04′ W), and SALU (São Luís, 2°35′ S, 44° 12′ W). Figure 4.5, upper panel, shows the geographical locations of these stations together with possible ground tracks of the AlfaCrux satellite, whose instantaneous position is marked by a dot. The satellite trajectory has been calculated with the Keplerian elements adjusted to the parameters of the planned mission. Table 4.1 summarizes the principal orbit information included in the corresponding sample Two Lines Elements (TLE) used in the calculation. The mapped satellite trajectories serve for illustrative purpose of possible communication scenarios.

Figure 4.5, lower panel, shows the FR angle calculated using the Global Ionospheric Scintillation Model (GISM, Béniguel, 2019; Béniguel & Hamel, 2011) for the BOAV station

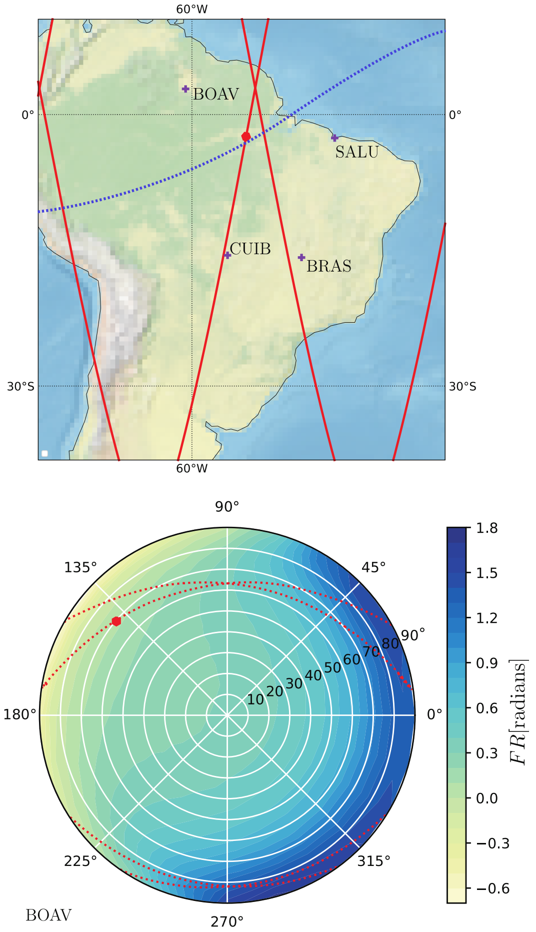

Figure 4.5 – Upper panel: locations of the ground stations BOAV, BRAS, CUIB, and SALU. The possible trajectories of the communication satellite calculated using the Keplerian elements from Table 4.1. The instantaneous position of the satellite at 01:30 UT, 7th of September 2017, is shown as the red dot. The approximated location of the geomagnetic equator is indicated by the dashed blue line. Lower panel: sky map for the BOAV station showing the distribution of Faraday rotation angle due to ionosphere. The dotted lines and the dot show possible trajectories and instantaneous position of the communication satellite as shown in the upper panel (Ferreira et al., 2022).

for the 7th of September 2017 at 01:30 UT. The GISM has a capability to calculate the FR for arbitrary communication links with the inclusion of ray bending effects. One can see that the FR is small for small and moderate zenith angles but can reach values greater than one radian when approaching the large zenith angles. In particular, for considered time and geographic location two regions of strong positive increment in polarization angle can be observed in the North-East and North-West directions, cf. Figure 4.5 (lower panel). This enhancement is due to the Earth's magnetic field direction and the ionization crest located over and northwards of the BOAV station. In the other part of the sky the zero or negative values of the FR angles can be seen close to the horizon. This is due to the smaller ionospheric electron density in the region of magnetic equator that is situated southwards of the BOAV station. It is worth to note that since the GISM is a climatological model, the calculated values of the FR

Table 4.1 – Elements of the TLE used for the orbit calculations. Some parameters such as the epoch have been adjusted to correspond to time of ionospheric conditions considered in this investigation.

Parameter	**Value**
Epoch	17241.99979167
Inclination	97.0000 (degrees)
RAAN	153.1430 (degrees)
Eccentricity	0.0003134
Argument of perigee	220.5360 (degrees)
Mean anomaly	108.0034 (degrees)
Mean motion	15.13104507 (revolutions per day)

are primarily applicable for quiet space weather conditions only and excludes the detailed analysis of the extreme events such as presented in Figure 4.4. In the present article, the storm condition is then incorporated by choosing the highest level for the solar radio flux of 140 sfu measured during this period. As the solar flux is the driving parameter of the GISM, the enhanced scintillation activity due to the storm is thus included in the following considerations. On the other hand, any consideration of storm-associated disturbances of the geomagnetic field is omitted.

In the simulation of the communication scenario between the BOAV station and the AlfaCrux satellite, one can see that in total four communication links could be established during this particular day with one passage during the time slot of interest. The instantaneous position of the satellite is shown as the red dot on the sky plot. During this satellite passage, the FR increment changes from negative to large positive value reaching northwards the region of disrupted communication channel if a linearly-polarized receiver antenna is used.

4.2.3 Mitigation of polarization loss factor

As presented in the previous section, the attenuation due to FR can be significantly high depending on the type of polarization used in the receiver and transmitter antennas. Therefore, power loss due to FR and associated depolarization has to be taken into account for the link budget computation. The latter is the comparison between the power given to the transmitter, the amount of power available in the receiver and the noise level at the same point of the receiver (Aguado-Agelet et al., 2019). In the case when the depolarization is well estimated, linearly polarized antennas may be employed on the ground station and adjusted to compensate the depolarization effect. Unfortunately, due to the short periods of satellites visibility (a few minutes at each passage), the FR must be quickly estimated, and the antenna must be quickly adjusted so the polarization losses may be reduced (Barbarić et al., 2018). This can be a challenging and costly task due to the high variability of the ionosphere in certain times and locations.

Based on the variability of the FR presented in this study, it was defined as the most suitable solution for dealing with the depolarization effects on the AlfaCrux mission the use of turnstile antenna with circular polarization on the satellite. At the ground station, two X-Quad antennas (2x18 elements) with gain of 14.95 dBi, being one right-hand circular polarized (RHCP) and the other left-hand circular polarized (LHCP) are used. In order to increase the link connection, the ground station was designed using a diversity scheme. The latter uses the two outputs of the antennas to obtain the signal from ever possible polarization of the incident wave (Aguado-Agelet et al., 2019; Vazquez-Álvarez et al., 2012). The polarization loss estimated with such approach is around 1 dB, which corresponds to 2 dB less than the maximum loss expected when using a circular polarized antenna at the satellite and a linear one at the ground station (Fernandez et al., 2020).

4.3 Ionospheric scintillation

The presence of ionospheric plasma irregularities, with scales varying from centimeter to hundred of kilometers, can cause fluctuations on the refractive index of the medium which lead to rapid random modulation of the amplitude and phase of trans-ionospheric signal. This phenomena, called scintillation, is one of the most severe disruptions on trans-ionospheric signals with frequency below 3 GHz (ITU, 2019) and is illustrated in Figure 4.6.

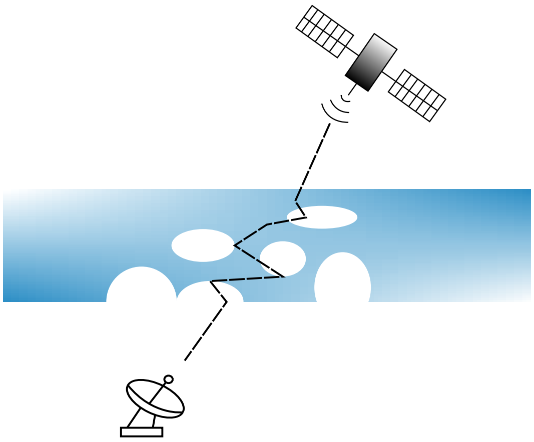

Figure 4.6 – Schematic representation of the ionospheric scintillation.

In the equatorial regions, it is well known that this phenomenon is likely to occur during the post-sunset hours with enhanced activity during equinoxes (Béniguel & Hamel, 2011). With this in mind, the purpose of this investigation is to quantify and characterize the average values of scintillation levels over the Brazilian region in order to support the mission and to propose a methodology for evaluating the risk of communication disruption during scintillation periods.

Two indices are usually employed to characterize the amplitude and phase scintillation levels: the S_4 and σ_ϕ indices, respectively. The former index is defined as the standard deviation of the normalized signal power over a determined period and usually can be classified in three levels: weak (S_4 <0.3), moderate ($0.3 \leq S_4 \leq 0.6$) and severe ($S_4 > 0.6$). For weak and moderate regimes, most observations in equatorial regions indicate that phase and intensity scintillation are strongly correlated (ITU, 2019). Therefore this study focus on the amplitude scintillation index S_4, which can be calculated according to:

$$S_4 = \sqrt{\frac{\langle I^2 \rangle - \langle I \rangle^2}{\langle I \rangle^2}}. \tag{4.3}$$

Here, I corresponds to the signal intensity (which is proportional to the square of the signal amplitude) and $\langle ... \rangle$ denotes either the ensemble or time averaging under the assumption that the received intensity is an ergodic random process (Guo et al., 2019; ITU, 2019).

In order to investigate the scintillation effects on UHF satellite communication systems, the GISM model has been also applied. This is the model recommended by the International Telecommunications Union (ITU) for ionospheric scintillation intensity prediction. The model has been validated in multiple studies and suits well for estimation of scintillation levels for navigation and telecommunication purposes. The ionosphere electron density at any point of the modeled medium is obtained from the NeQuick model (Radicella, 2009), which is also included in the GISM (Béniguel & Hamel, 2011). As the solar irradiance is one of the driving parameters of the NeQuick model, the scintillation indices calculated with the GISM are sensitive to this parameter as well.

In order to investigate the occurrence of scintillation over the Brazilian region, the CUIB and BOAV stations are used to perform the simulations using the GISM. These particular stations are selected due to their close location to the south and north crest of the Ionospheric Equatorial Anomaly (IEA), respectively, which are areas where one can expect the occurrence of the scintillation (Correia et al., 2018). The locations of these stations are shown in Figure 4.5, upper panel. They are a part of the Brazilian Network for Continuous Monitoring (RBMC) and maintained by the Brazilian Institute for Geography and Statistics.

For each one of the aforementioned locations, the S_4 index was calculated using the GISM for the year of 2017. Figure 4.7 (left panel) presents the scintillation index for the CUIB as a function of local time and day of the year. One can note that significant levels of the S_4 index are observed during the equinoxes. Also during these periods, one can observe that such levels can last up to 4:00 LT.

In order to verify the level of peak-to-peak fluctuations of the signal associated with the

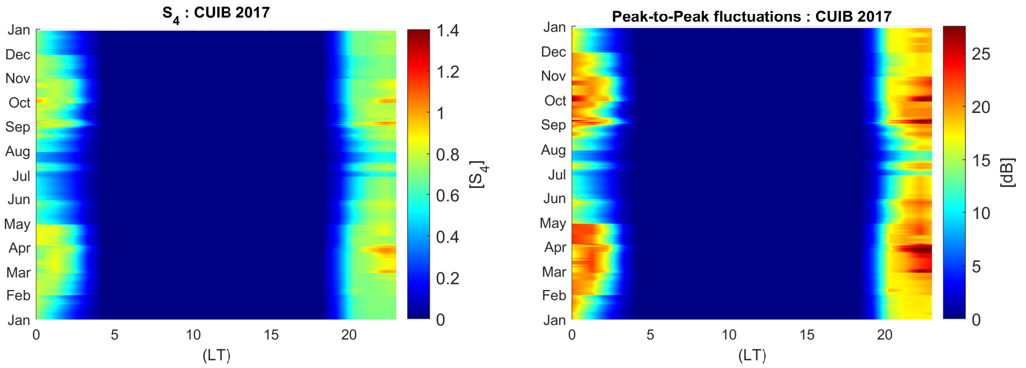

Figure 4.7 – S_4 scintillation index (left panel) and estimated signal peak-to-peak fluctuations (right panel) for the CUIB station during the year 2017 for a 437 MHz signal (Ferreira et al., 2022).

observed S_4 levels, one may use the following empirical relation (ITU, 2019):

$$\mathcal{P}_{fluc}[dB] = 27.5 S_4^{1.26}. \tag{4.4}$$

Based on this formula, the results for the CUIB station are computed and presented in Figure 4.7 (right panel), indicating significant levels of peak-to-peak fluctuation during the post-sunset hours, reaching values higher than 25 dB.

Figure 4.8 presents the level of scintillation throughout the day and how it varies seasonally for the CUIB location. It shows the frequency of occurrence of different scintillation levels for each season of the year 2017 as a function of local time. One can note that during all seasons, severe levels of scintillation are expected between 22:00 and 3:00 LT, with higher levels observed during summer and lower levels observed during the winter of 2017. Moderate values, on the other hand, are observed more frequently during the winter and less frequently during the summer. During the autumn and spring, similar frequencies of occurrence were observed with the slightly higher occurrence of severe scintillation during the autumn when compared to the spring.

Aiming at investigating the latitudinal variability of the scintillation over the Brazilian sector, similar analysis for the BOAV location has been conducted. Figure 4.9 (left panel) shows the S_4 index as a function of local time and day of the year. One can note that the S_4 levels for this location are significantly lower than the ones observed at CUIB. Moderate levels of scintillation, that are observed to occur up to 4:00 LT for the CUIB station, are in the case of the BOAV mostly restricted to the interval from 21:00 to 2:00 LT. The levels of peak-to-peak fluctuations presented in Figure 4.9 (right panel) exhibit notably lower values, when compared to the CUIB station, except for the some periods, such as the September 2017 events. From Figure 4.10 one can infer that severe levels of scintillation for this location are not very frequently observed, being mostly restricted to the interval from 22:00 and 2:00 LT and more often observed during winter and spring.

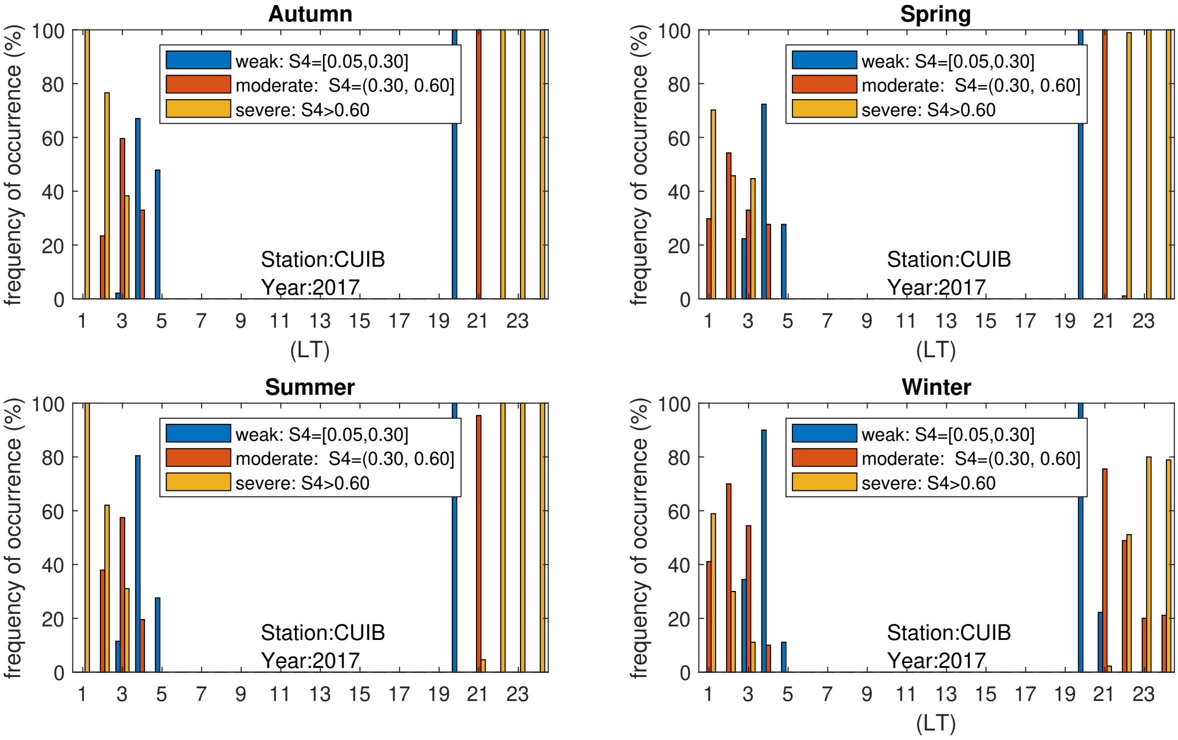

Figure 4.8 – Percentage of occurrence of the signal fluctuation levels for the CUIB station for different seasons of the year 2017 (Ferreira et al., 2022).

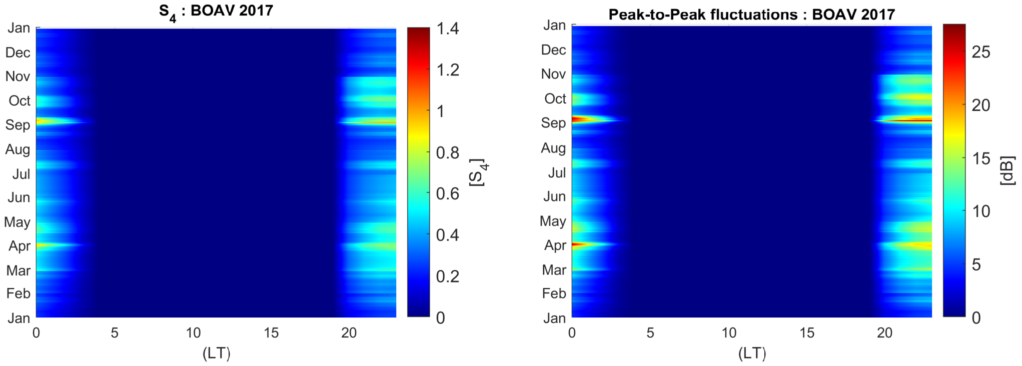

Figure 4.9 – S_4 scintillation index (left panel) and estimated signal peak-to-peak fluctuations (right panel) for the BOAV station during the year 2017 and for a 437 MHz signal (Ferreira et al., 2022).

The comparison of different regions of the Brazilian sector exhibits the variability of scintillation levels on the geographic location. Thus, such spatial variability has to be taken into consideration when designing a satellite communication service, such as the AlfaCrux mission. The analysis shows that considerable levels of peak-to-peak fluctuations due to scintillation for the signals on the frequency 437 MHz can occur. Such levels might compromise the communication reliability during the post-sunset hours, and, depending on the application, can jeopardize the communication tasks. Different cases illustrate situations in which the scintillation can compromise *narrowband* communication (Fernandez et al., 2020), leading to the complete interruption of the link in some extreme cases. An example

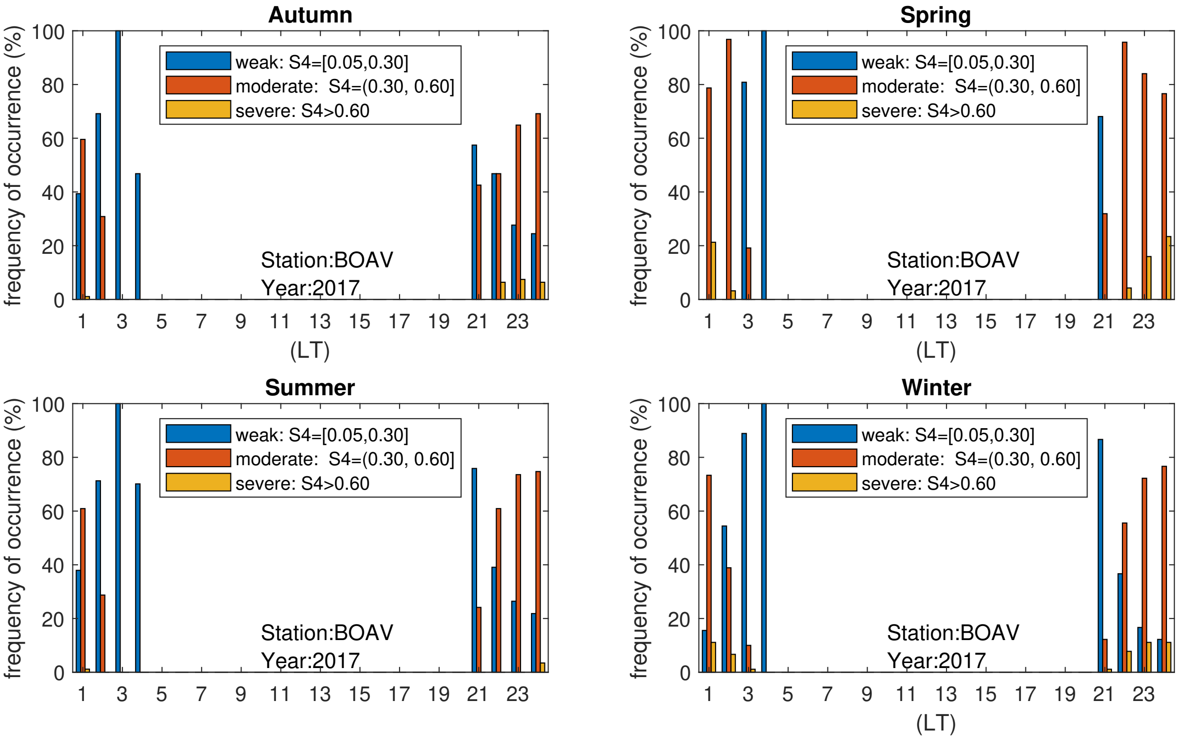

Figure 4.10 – Percentage of occurrence of the signal fluctuation levels for the BOAV station for different seasons of the year 2017 (Ferreira et al., 2022).

of such communication outage has been reported during the Anaconda operation (Kelly et al., 2014), when the tactical communication failed due to extensive scintillation and multipath effects. Therefore, for the mission planning of a communication satellite it is important to investigate quantitatively how such scintillation can impact the reliability and performance of the communication link. The next section presents the results on this regard.

4.4 Scintillation and communication resilience

The communication planning for the AlfaCrux mission takes into account the scintillation effects on the satellite signal by means of the S_4 index derived from the GISM. Based on the level of peak-to-peak fluctuation of the signal associated with the observed S_4 index, one can estimate the correspondent signal loss to be accounted in the link budget computation. The signal loss associated with scintillation can be expressed as

$$L_{fluc} = \frac{\mathcal{P}_{fluc}}{\sqrt{2}}, \tag{4.5}$$

where $\mathcal{P}_{fluc}$ is given by Equation (4.4) and correspond to the peak-to-peak fluctuation in dB (ITU, 2019; Reis, 2021).

Although the scintillation effects are intense in the equatorial regions, the impacts on the communication missions are frequently overlooked on the link budget computation (Kelly et al., 2014). Henceforth, it is necessary to develop a methodology for including the scintillation effects on the planing of the communication link of space missions. More specifically, the mapping of the communication channel availability in regions exposed to strong scintillation is of great practical importance in this case. Based on this, an assessment of the risk of communication loss caused by scintillation is proposed, which helps to identify the most favorable time intervals and regions for communication, even during periods of expected scintillation over the Brazilian sector.

4.4.1 Risk Analysis

The usage plan for the communication channel proposed in this work is based on the risk analysis from the decision theory (Koulouri et al., 2020; Oppe, 1988). In this context, given a specific activity (e.g. satellite-receiver communication), one can define the risk as the expected loss incurred to such activity. In order to estimate the risk it is necessary (Koulouri et al., 2020):

- to find features that describe the condition in with the activity is performed (e.g. S_4 level can describe communication under scintillation);
- to determine the frequency of occurrence of such features;
- to know how injurious the condition described by these features is for the successful outcome of activity.

Each of these requirements can be expressed by a feature vector, a probability and a loss function, respectively. Denoting random variables by capital letters and their realizations by lower-case letters, one can start with the measurable variable feature $Z \in \mathcal{Z}$, where $\mathcal{Z}$ represents the set of all possible feature vectors. In order to illustrate the concept, one can consider the indicator function (also called the loss function), given by

$$l(z; z_{thr}) = \begin{cases} 0, & \text{if} \quad z < z_{thr}, \\ 1, & \text{otherwise}, \end{cases} \tag{4.6}$$

which suggest that there is no loss when values of z are below a threshold value z_{thr}. In the case $z \geq z_{thr}$, losses are equally injurious (Koulouri et al., 2020). The risk $r(z_{thr})$ is defined as the expected value of the indicator function presented in Equation (4.6), and is given by

$$r(z_{thr}) = \langle l(z; z_{thr}) \rangle = \int_{\mathcal{Z}} l(z; z_{thr}) p(z) dz = \pi(Z \geq z_{thr}), \tag{4.7}$$

where $p(z)$ is the probability density function of the feature Z, and $\pi(Z)$ corresponds to the probability that Z assumes an injurious value. In such way, the risk has an interpretation in terms of the probability. Based on the risk concept, in combination with the analysis of the link budget, an investigation on how the scintillation might impact the communication activities is performed.

4.4.2 Link Budget

The link budget is estimated by comparing the power given to the transmitter to the power available at the receiver assuming that the transmitted signal is exposed to the noisy environment along the propagation link. For a communication satellite, there are two different link budgets, the uplink (from the ground station to the satellite) and the downlink (from the satellite to the ground station, Aguado-Agelet et al., 2019). The power received by a real antenna can be expressed as (Reis, 2021; Ulaby et al., 1981; Wertz & Larson, 1999):

$$P_r = \frac{P_t G_t G_r}{L_{t+r}} \quad \text{[W]}, \tag{4.8}$$

where G_t and G_r correspond to the transmitter and receiver antennas gains, P_t corresponds to the transmitted power and L_{t+r} represents all losses, including losses due to attenuation in the atmosphere, losses associated with the transmitting and receiving antenna, polarization and free-space path losses (Aguado-Agelet et al., 2019; Pratt & Allnutt, 2020; Reis, 2021; Saeed et al., 2020). In particular, the free-space loss depends on the propagation path length R as

$$\begin{aligned} L_{fs} &= (4\pi R/\lambda)^2, \qquad (4.9) \\ R &= \sqrt{(R_\oplus + H)^2 - R_\oplus^2 \sin^2\theta_o} - R_\oplus \cos\theta_o, \end{aligned}$$

where λ is the signal wavelength, $R_\oplus$ is the Earth radius and H is the satellite altitude (Reis, 2021). At large zenith angles θ_o the free space loss becomes considerable for possible communication outage.

At the same time, for simplicity, the dependence of tropospheric loss on zenith angle is not considered, since this loss level is considerably lower than the free-space one. This investigation considers the attenuation due to rain and foliage as the main tropospheric losses. In the former case, for the frequency of 437 MHz the attenuation estimated based on the recommendation ITU-R 837-7 (ITU, 2017) is lower than 0.001 dB only. For the latter, the attenuation estimates are obtained based on the model of attenuation due to foliage described in Hasirci et al. (2016), considering an average foliage depth of 5 meters (Hemadeh et al., 2018; Reis, 2021). Combined, both effects lead to losses of approximately 3.3 dB.

For disturbed ionosphere, the loss L_{t+r} includes also the fluctuating losses in addition

Table 4.2 – Parameters of the link budget calculation for an elevation angle of 30°.

Parameter	**Value**
Frequency	437 MHz
Data rate (R_b)	9600 bps
Cubesat antenna gain (G_t)	0.0 dBi
Ground station antenna gain (G_r)	14.95 dBi
Transmitted power (P_t)	1 W (0 dbW)
Free-space loss	144.43 dB
Tropospheric loss	3.3 dB
Polarization loss	1.04 dB
Noise temperature (T)	500 K
E_b/N_o	27.95 dB
Required E_b/N_o	8.4 dB
Margin	**19.56 dB**

to the aforementioned regular losses. The fluctuating losses are associated primarily with the ionospheric scintillation and are described by the quantity L_{fluc}, cf. Equation (4.5). The intermittent and intense space weather events also contribute to the enhancement of this contribution to the total loss budget.

The link budget, therefore, is a set of parameters that define the communication link in terms of power available for a reliable transmitter-receiver connection. Such link information is also useful to obtain the satellite-to-ground (downlink's) energy-per-bit to noise spectral density, which can be used to measure the reliability of the communication channel (Saeed et al., 2020). The energy-per-bit, E_b, to noise spectral density, N_o, at the ground station can be expressed as (Reis, 2021; Wertz & Larson, 1999)

$$\frac{E_b}{N_o} = \frac{P_t G_t G_r}{L_{t+r} k T R_b}, \tag{4.10}$$

where T is the system temperature noise, R_b is the target data rate and k is the Boltzmann constant ($k = -228.6$ dB(W/K/Hz)).

Based on the communication requirements for the AlfaCrux mission, the link budget has been computed and is presented in Table 4.2, and the E_b/N_o and margin are obtained. It is important mentioning that depending on the modulation scheme used in a system, various aspects of scintillation may affect differently the system performance (Fernandez et al., 2020; Yeh & H., 1982). The investigation of the performance of different schemes is, however, out of the scope of the work. This study focuses on the downlink for the AlfaCrux mission, since it provides a lower margin when compared to the uplink.

As presented in Table 4.2, the design of a satellite mission relies on the information of the required performance of the uplink and downlink, the propagation characteristics for the frequency band used, and the parameters of the satellite and the ground station. Sometimes, however, the complete information is not available and the designer must estimate values and generate tables of system performance based on assumed scenarios. Usually, the loss levels determined for the uplink and downlink depend on the signal frequency chosen by the designer, who in most cases shall also estimate the losses due to ionospheric attenuation on the link budget computation (Pratt & Allnutt, 2020). Fluctuating losses due to ionospheric scintillation often occur at UHF at the level of 2-3 dB peak-to-peak values, but can reach significant levels during occasions when steep ionospheric gradient densities are present. Such scintillation levels can reach as high as 27 dB (Basu et al., 1980; Kelly et al., 2014). The associated fluctuating losses are not included in the margin computation presented in Table 4.2, however they need to be taken into account for low latitude regions, since signal fades of approximately 10 dB or higher, combined with other effects such as multipath, are sufficient to cause communication outages (Kelly et al., 2014).

From the best of the author's knowledge, a systematic procedure aiming to optimize the planning of small satellite communication missions, such as AlfaCrux, is still missing, although some recent investigations on Positioning, Navigation, and Timing (PNT) low orbit satellites are ongoing, such as the investigations presented in Prol et al. (2022). In this regard, it is desirable to have a metric that allows one to assess the probability of success on the communication during post-sunset hours in equatorial regions when the severe fluctuating loss due to scintillation may occur. In this sense, this work proposes a methodology that takes into account the attenuation due to scintillation on the computation of the link margin. Combining the scintillation level information with the risk analysis presented in Section 4.4.1 one can derive the risk of communication outage. Similarly to Section 4.2.2, the simulated TLE for calculation of the satellite Keplerian parameters is used (see Table 4.1). Scintillation level information and the corresponding communication outage regions are convenient to present as the sky plots for specified receiving ground stations. Figure 4.12 shows such plots with the superimposed possible satellite trajectories for the BOAV and CUIB stations.

Scintillation indices S_4 in Figs. 4.12 (a), (c) are calculated using the GISM for the 7th of September 2017 at 1:30 UT. This time corresponds to the high scintillation activity in the Brazilian region. The ten centimeter solar radio flux with a value of 140 has been used as the driving parameter of the model. One can see that the scintillation index grows with the increase of the zenith angle, the effect associated with growing propagation path of the signal in the irregular ionosphere.

The calculations of S_4 index for the BOAV station show the region of high scintillation activity spreading northwards starting from the East up to the southwest direction, see Figure 4.12 (a). This maximum is related to one of the ionization crests that for specified time is located over and northwards of the station. In the southwards direction scintillation levels are comparable or even less than those at the region near the zenith. This effect is related with the location of the magnetic equator southwards of the station, which is the region with

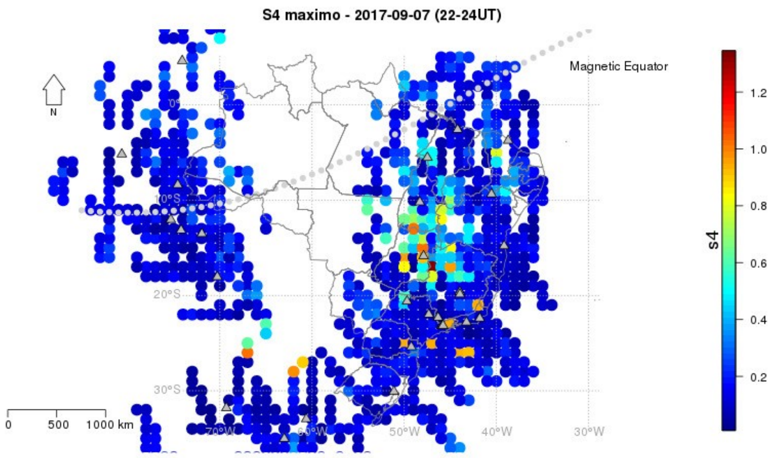

Figure 4.11 – Maximum S_4 index obtained from the ISMR Query Tool for the GPS frequencies for the period between 22-24 UT on September 7, 2017.

lower background electron density. The distribution of the scintillation index for this station can be compared with the map for the Faraday rotation in Figure 4.5 (b). In both cases the background electron density correlates with the values of the FR angle and of S_4.

Figure 4.12 (c) shows the analogous sky map of S_4 index for the CUIB station. In this case the station is located in the region of the south ionization crest, so the region of the enhanced scintillation activity is seen for slant propagation paths that cross the ionosphere within the region that located southwards of the station from North-East up to West directions. One can also observe the small region of large scintillation in North-West direction that corresponds to the north ionization crest. Similar increases can be found in Figure 4.11, which shows the S_4 for GNSS frequency range over the Brazilian region on from 22 to 24 UT on the 7th of September obtained from the ISMR Query Tool[2] (Vani et al., 2017). One can note an agreement on the location of enhanced scintillation, however with different amplitudes, given the different frequencies used on GNSS.

Figs. 4.12 (b) and (d) show the communication outage maps for the BOAV and CUIB stations. These maps are obtained after the inclusion in the link budget computation of the attenuation factor due to scintillation-associated fluctuating losses. In other words, based on the scintillation levels at each point of the sky maps in Figures 4.12 (a), (c), a new energy-per-bit to noise spectral density ratio, $(E_b/N_o)_{scint}$, is computed and compared to the required ratio $(E_b/N_o)_{req}$. The required energy-per-bit to noise spectral density ratio is set by the mission requirements, whereas the ratio $(E_b/N_o)_{scint}$ is obtained from Equation (4.10) with the inclusion of the signal loss factor given by Equation (4.5). In the case when $(E_b/N_o)_{scint} < (E_b/N_o)_{req}$, an outage event is assumed to occur and corresponds to the *yes* region in Figures 4.12 (b), (d). On the other hand, regions where the scintillation does not reduce E_b/N_o below the required levels are marked as *no* regions corresponding to

---

[2] https://ismrquerytool.fct.unesp.br/is/

no communication outage due to scintillation.

It can be observed that the regions of communication outage appear primarily at large zenith angles. The extension of these regions is closely related with the location of the ionization crests relative to the ground station at specified time. Another observation is that the communication outage is present at time of high scintillation activity for all azimuth angles if the zenith angle is greater than $80°$. This is the cumulative effect of strong scintillation-associated loss and purely free-space loss. The latter depends on the length of the slant propagation path, that in turn becomes large for large zenith angles, see (4.9). This suggests to apply the masking angle of $10°$ for ground observers in the communication mission for AlfaCrux satellite for times of high scintillation activity. It can be seen that the fixed mask angle of $30°$ could, theoretically, eliminate the outage possibility completely. However, the choice of such angle might significantly reduce the possibility of establishing communication with satellite. This is well illustrated in Figure 4.12 (b), where the satellite, which instantaneous position is shown with the dot, could establish short communication link, which will be discarded if the ground station is operated with the masking angle fixed to $30°$. It is thus advantageous to use the variable adaptive mask angle that can be defined using the boundary between *yes* and *no* regions on the communication outage maps similar to those of Figure 4.12 (b), (d).

4.4.3 Risk of communication outage associated with scintillation

The scintillation-associated condition $(E_b/N_o)_{scint} < (E_b/N_o)_{req}$ for communication outage considered above can be utilized for the definition of the threshold value z_{thr} used in the risk analysis as outlined in Section 4.4.1. For that the following random variable is defined

$$z = |I - \langle I \rangle| / \langle I \rangle, \tag{4.11}$$

which is the normalized error for received signal intensity. The average intensity here can be calculated, for example, by accumulating measurements during some short time interval. Then the threshold z_{thr} is the maximal tolerable value of this quantity for which the communication is still possible. As this threshold is a number, one can interpret it as the minimally tolerable scintillation index S_4 (Koulouri et al., 2020).

By using Equation (4.6), the loss function $l(z; z_{thr})$ is defined, which after averaging yields the required risk function of the communication outage $r_{outage} = \langle l(x; x_{thr}) \rangle$. The values of the risk function lie in the range $[0, 1]$ with the highest risk value equal to one. This formula can be implemented in simulation programs as follows: scintillation simulating models are usually using the single- or multiple-phase screen algorithm. The idea behind this technique is that the properly generated phase screen placed within the ionospheric layer and along the propagation of a signal wave introduces random modulation of the phase of the

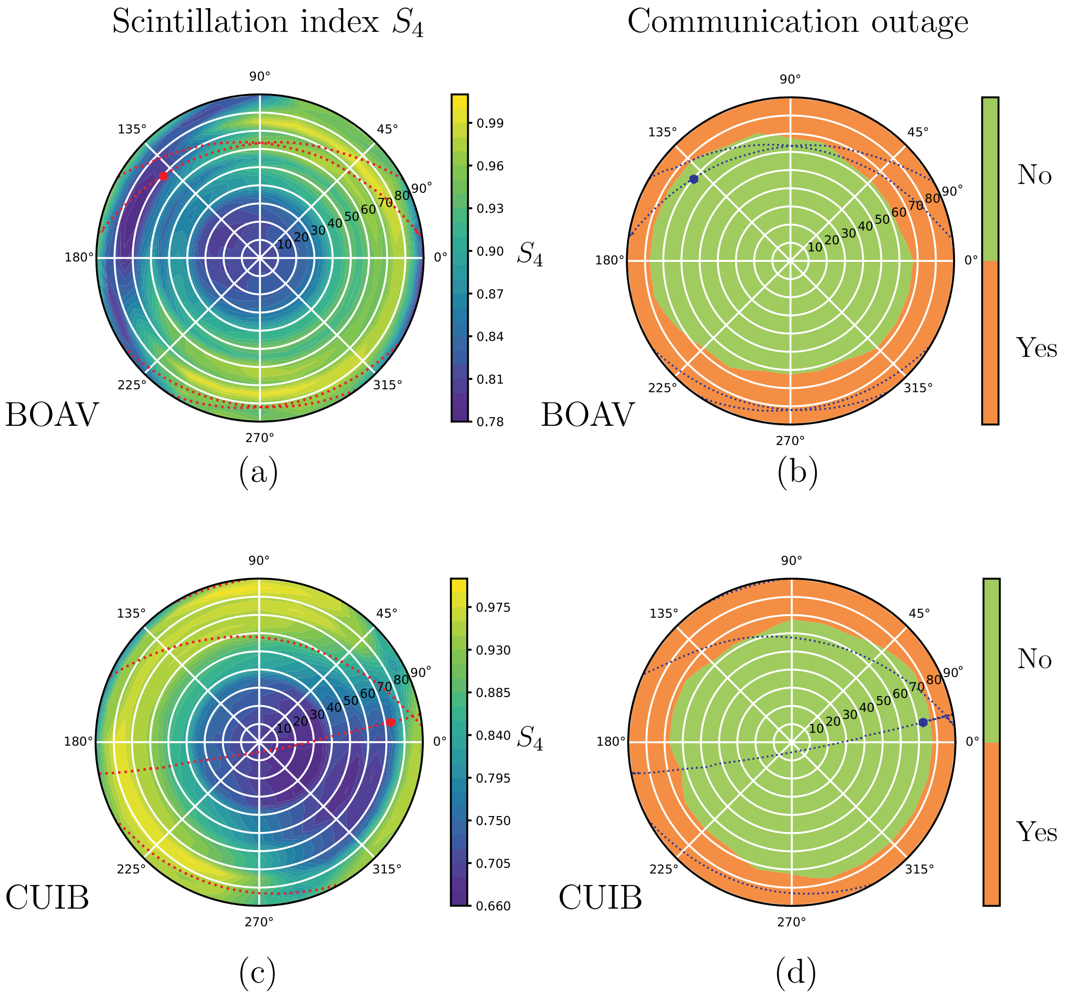

Figure 4.12 – Scintillation S_4 indices (a), (c) and the associated communication outage maps (b), (d) mapped to the sky plots for the BOAV and CUIB ground stations. The maps are calculated for the period of high scintillation activity over the Brazilian region on 7th of September 2017 at 01:30 UT. The sample satellite passages during one day are also shown (dashed lines) with the instantaneous position of the satellite at 01:30 UT marked by a dot (Ferreira et al., 2022).

latter. These gained random phase increments result in the formation of complex diffraction pattern on the ground and in uneven distribution of received intensity. The single realization of the variable z corresponds to a single generation of a set of random phase screens along the propagation path. For the same communication geometry one then generate the set of random phase screens multiple number of times, then calculates the loss function $l(z; z_{thr})$ for each realization and perform the averaging in order to estimate the risk function.

Algorithm 1 Risk of scintillation impact on low-latitude SATCOM (adapted from Reis, 2021)

```
    Input: $S_4$ index
    Output: Risk of communication outage
if -20°N $\leq$ Geomagnetic latitude $\leq$ 20°N and post-sunset LT then
    Compute the $S_4$ index for the area of interest;
    $P_{fluc} = 27.5 S_4^{1.26}$;
    $L_p = \frac{1}{\sqrt{2}} P_{fluc}$;
    Include attenuation due to scint. ($L_p$) in the link budget;
    Compute $(E_b/N_o)_{new}$;
    if $(E_b/N_o)_{new} > (E_b/N_o)_{req}$ then
        Satisfactory link margin
        Communication channel available
    else
        Communication channel not available;
    end if
    Compute risk: The ratio of the interest region (sky plot) with communication outage to the total area
else
    Low risk of scintillation impact on the channel (channel available)
end if
```

In the view that the scintillation simulation programs, such as the GISM, provide just the interface for calculating the scintillation index S_4 alone, it is reasonable to adjust the aforementioned calculation procedure. The empirical relation shown in Equation (4.4) is then used, along with Equation (4.5), for the estimation of the communication outage risks. In particular, the calculated fluctuating loss presented in Equation (4.5) is used in the total loss budget L_{t+r} and then the ratio shown in Equation (4.10) is calculated. This estimated energy-per-bit to noise spectral density ratio $(E_b/N_o)_{scint}$ is compared with the required value $(E_b/N_o)_{req}$ and the communication outage map is constructed in the similar manner as shown in Figure 4.12 (b) and (c). The evaluation of the risk function shown in Equation (4.7) is performed then by geometric interpretation of the communication outage frequency as the ratio of sky map region with communication outage (orange area in Figures 4.12 (b) and (d)) to the total area (orange and green areas in Figures 4.12 (b) and (d)).

The Algorithm 1, which is an extension from the methodology presented in Reis (2021), summarizes the procedure for doing this estimation. Differently from the algorithm pre-

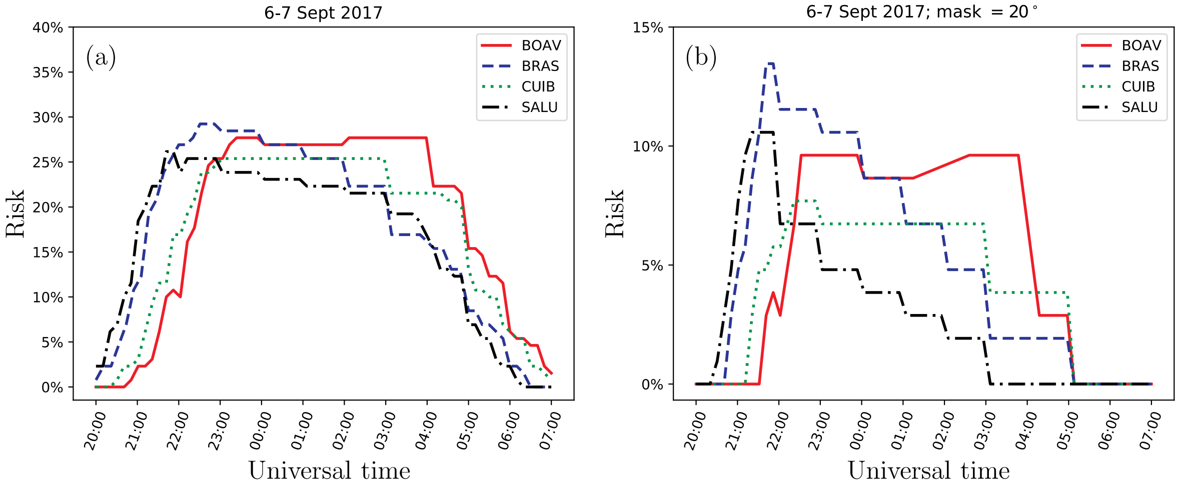

Figure 4.13 – Risk of communication outage due to scintillation for the AlfaCrux mission for the cases when the ground stations establish communication without (a) and with (b) applying the mask angle of 20°. The curves are calculated for the equivalent isotropic radiated power of 1 W and the required energy-per-bit to noise spectral density ratio $(E_b/N_o)_{req} = 8.4$ dB (Ferreira et al., 2022).

sented in Reis (2021), in the proposed methodology the whole field of view is considered in the analysis, and not only the station coordinates. In addition, the risk analysis from decision theory is included in order to compute the risk of communication outage.

Figure 4.13 presents the calculated risk for the BOAV, BRAS, CUIB, and SALU receiver stations as a function of the universal time for the night of 6-7th of September 2017. Figure 4.13 (a) shows the risk if the whole sky hemisphere is used in the calculation, whereas Figure 4.13 (b) show the risk curves if the mask angle of 20° is applied by ground stations. Since the zenith angles in the latter case are restricted to the range $[0°, 70°]$, the estimated risk is clearly lower, however, in the expense of discarding some portions of sky where communication might be still possible.

Inspecting Figure 4.13 one can note the dependence of shape and definition domain of the risk curves on the geographical location of the stations. The onset of the growing risk of communication outage for the BRAS and SALU stations is earlier than for the BOAV and CUIB stations since the former are located eastwards from the latter ones, following the evolution of the EIA depicted from the GISM. Thus, the day/night terminator and the resulting onset of scintillation activity reaches the stations BRAS and SALU earlier than the BOAV and CUIB locations, cf. Figure 4.5. The apparent skewness of the risk distribution for the SALU and the BRAS station is related with the time evolution of the ionization crests at these longitudes.

Finally, it is important to note that the risk calculated for the whole sky hemisphere, as presented in Figure 4.13 (a), can be considered as the worst-case scenario risk estimation. As already mentioned, for the case study presented in Figures 4.12 (b) and (d), using a 20°

mask angle for post sunset times of high scintillation activity in the risk computation would reduce the value of the risk estimate (see Figure 4.13 (b)). It is preferable, however, to consider a more conservative risk analysis with no mask angle included. The considered here worst-case scenario provides some extra margin for possibility of space-weather-related signal disruptions in communication scenarios with finite mask angles of the ground receivers.

4.4.4 Scenarios evaluation

In this section different case studies are presented in order to demonstrate the capabilities of the proposed methodology to serve as a tool for the planning and operation of satellite communications in regions with high scintillation activity. In this set of simulations, the required values of $(E_b/N_o)_{req}$ are varied between 5 dB and 10 dB, and different values of transmitted power are chosen (1 W and 1.5 W). The reason for considering different values of transmitted power is motivated by the adaptive power control solution, in which the power of the transmitted signal is increased in order to compensate the attenuation along the signal propagation path. Similar kind of approach has been used in the GPS satellites in order to increase signal protection against jamming (Esenbuğa et al., 2023). In such a case, under the favourable communication conditions, the transmitted power can be reduced, and when conditions deteriorate, transmitted power levels can be increased (Glover, 2017; Reis, 2021).

The results depicted in Figure 4.14 show how the methodology can be used on the mission planning for the selection of the suitable transmitted signal power for the required E_b/N_o in order to reduce the probability of outage. These figures are calculated for the whole sky map coverage, i.e., zero mask angle, and can be considered as the worst case scenario. Figure 4.14 (a) and (c) can be compared with Figure 4.13 (a) as plots for transmitter antenna with the same equivalent radiated power of 1 W but with different values of the threshold value of $(E_b/N_o)_{req}$. It can be seen that lowering the level of the required energy-per-bit to noise spectral density decreases the communication risk. Clearly, this dependence is because the level of the tolerable noise in the channel is accepted to be large.

On the other hand, if one compares the Figures 4.14 (a) and (b), or (c) and (d), the increase of the equivalent radiated power from 1 W to 1.5 W reduced the risk of communication outage. This is because the received energy P_r and, hence, the associated total energy-per-bit spectral density E_b are proportional to the antenna power P_t at the transmitter side (Reis, 2021), cf. Equations (4.8) and (4.10). The increase of these quantities relative to the fixed required value $(E_b/N_o)_{req}$ enlarges the threshold for channel loss level that can be tolerated and, therefore, reduces the associated communication risks. It is also important to note that, since such small satellite missions such as AlfaCrux have restriction on the payload weight and are thus limited in antenna transmitting power, the designers have to find an optimal compromise between the transmitted power and the acceptable communication performance.

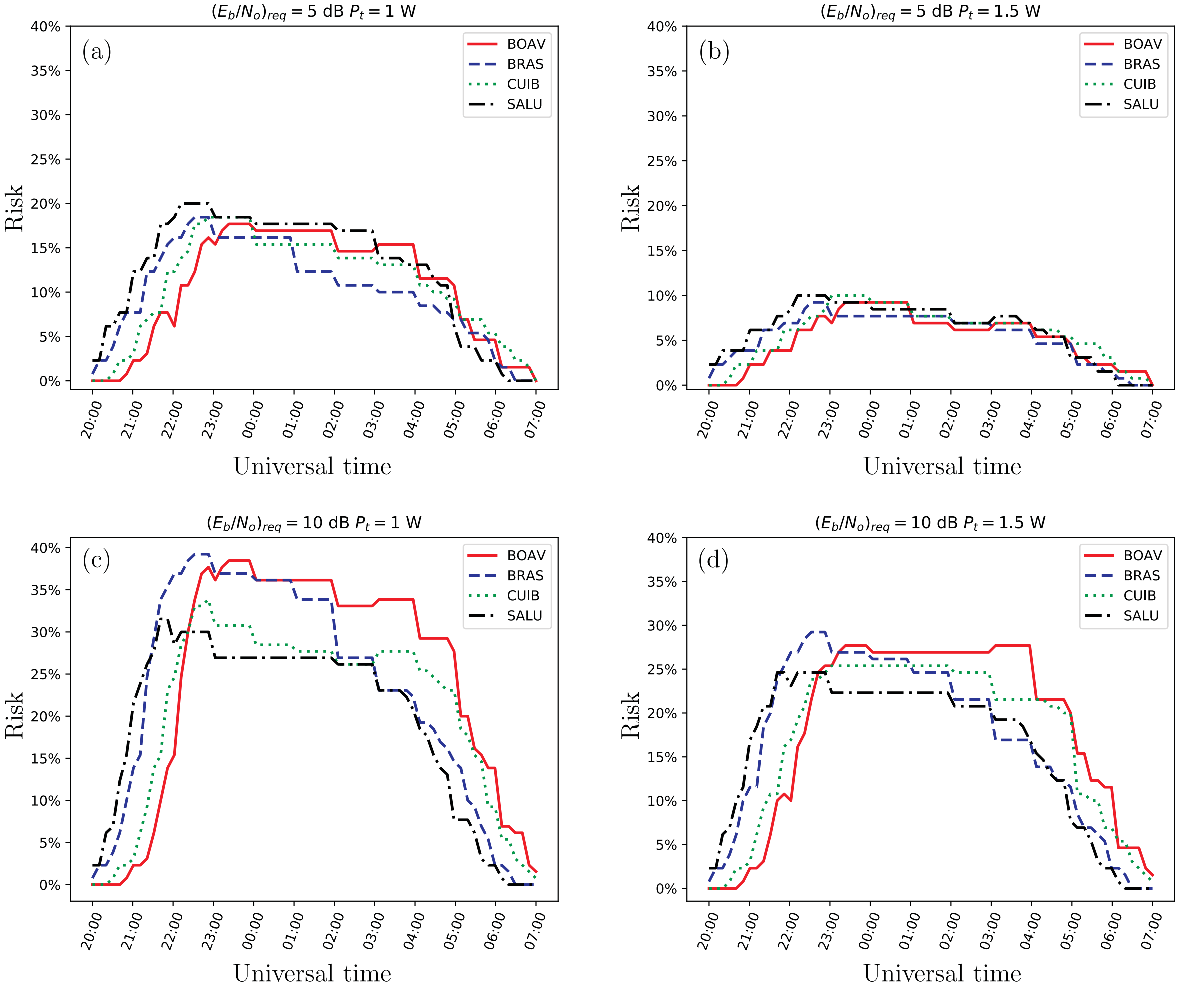

Figure 4.14 – Evolution in time of the communication risk estimates for various values of the required threshold ratio $(E_b/N_o)_{req}$ and the power of the transmitter antenna. The calculations are performed for the night from 6th to 7th of September 2017 using the solar radio flux daytime value of 140 sfu (Ferreira et al., 2022).

4.5 Summary

This work analyzes the effect of the ionosphere on the UHF satellite communication systems and take the AlfaCrux UHF CubeSat mission as a case study. The level of absorbed solar ultraviolet energy by the atmosphere drives the ionization processes in the ionospheric layer. The resulting ionization levels have primarily twofold effect on the radio communication systems operating in the lower UHF band.

Firstly, the propagating linearly-polarized signal from satellite experiences the action of the geomagnetic field. The latter rotates the polarization plane, the effect known as the Faraday rotation. The angle of rotation depends on the total electron content along the propagation path and, hence, on the background ionization level. If the linearly-polarized antenna is used for receiving the signal, the misalignment of the antenna polarization with the rotated polarization plane of the signal results into reduction or complete loss of the detected signal. For the AlfaCrux mission, the solution adopted to mitigate this problem consists on the use of a turnstile antenna with circular polarization on the satellite and a set of two X-Quad antennas for RCHP and LHCP at the ground station.

Secondly, the plasma that is lifted during the daytime diffuses downwards along the magnetic field lines forming two ionization crests situated on both sides of magnetic equator. At post-sunset hours, this process is accompanied by the formation of ionospheric instabilities, regions of depleted plasma and strong electron density gradients. The latter effects impact the phase and amplitude of the propagating signal wave in random manner, the phenomenon known as ionospheric scintillation. Similarly to the Faraday rotation effect, the strength of scintillation is related to the ionization levels, i.e., to the solar energy deposited in the ionosphere.

Based on these impacts, this work analyzed the morphology of the Faraday rotation angle, associated with it polarization loss factor, and the amplitude scintillation index for UHF communication band. In particular, this chapter investigates the variability of these quantities with the daytime, season, and geographic position for periods of low and high solar activity. For this task the vertical communication link geometry that corresponds to the satellite position in zenith of ground-based receiver was considered. In order to include the slant path effects in the analysis of communication disruptions, sky plots for specified ground stations in the Brazilian region were used. Such maps show the Faraday rotation angle and the scintillation index as functions of receiver's zenith and azimuth angles, incorporate the slant path effects and the refractive bending of signal rays, and show the trajectories and instantaneous position of the flying-by CubeSat satellite. Additionally to this, the communication outage regions can be identified from such maps, which are useful for optimization of communication activity. For example, the border of communication outage region can be used for definition of the mask angle of the ground station in an adaptive way such that the communication link is closed if the satellite elevation angle is smaller than the determined mask angle.

This work also presents a new methodology to assess the risk of communication outage due to ionospheric scintillation for the AlfaCrux mission. Such methodology can be used directly for different space missions operating in the UHF band. Given the lack of scintillation measurements on the UHF frequency band of the AlfaCrux mission, one can make use of already validated scintillation models for retrieving ionospheric scintillation information. Although climatological models are not able to reproduce some transient events due to geomagnetic storms, they have the advantages of allowing the investigation of different frequencies and providing good spatial coverage. Using the climatological scintillation models such as the GISM one can evaluate in advance the communication risks due to scintillation for specified receiver station and optimize the communication protocol. The risk level as a function of time, which in this work has been derived from risk analysis of decision theory, serves well to this purpose. The dependence of such risks on the mission design parameters, such as the power or gain of transmitter antenna or the level of tolerable losses, gives an useful insight in the possible performance of communication satellite mission.

5 Conclusions and Recommendations

5.1 Conclusions

This dissertation presents the results on the analysis of the SWe events and some of their impacts on satellite communication systems. Different SWe effects are investigated: the substorms (by means of the AE index), the Travelling Ionospheric Disturbances generated during geomagnetic storms and the effect of Faraday Rotation and Scintillation on satellites operating in the UHF communication band. A summary description of the current results for these studies are presented in the sequel.

The first analysis consists on the investigation of LSTIDs excited during geomagnetic storms. It is divided in two sections:

- The first section shows an analysis of the geomagnetic storms and LSTIDs observed during the descending phase of the SC 24 (from 2015 to 2019). In this investigation the LSTIDs amplitudes are automatically detected based on a 2D FFT spectrum analysis, and their statistics are presented. The results show that most of the disturbances excited during the period have amplitudes below 1 TECU and they are in majority excited during daytime, which may be associated to TIDs generated due to passage of the solar terminator. In addition, the amplitude of the daytime disturbances are in general lower than the ones observed during nighttime which may be related to the expansion of the auroral oval, but also to the ion drag effect, which may attenuate the amplitude of such disturbances.
- In the second section, the LSTIDs excited during the 7-8th September 2017 event are investigated. GNSS data from ground-based stations have been used in this study to identify the LSTIDs and their different characteristics in amplitude, period and phase speed. The investigation suggests that Joule heating due to the dissipation of Pedersen currents is the main contributor to the excitation of the observed LSTID. In addition, an investigation on potential GNSS based indices that can serve as precursors for the occurrence of LSTIDs is presented. The AATR index and ionospheric gradients are found to be promising precursors for the LSTIDs occurrence that may support real-time monitoring of such disturbances.

In the second part of this work, investigations on the prediction of space weather events based on solar wind measurements are presented. Two main events are analysed here: the substorms (by means of the AE index) and the LSTIDs. The results obtained for each task are:

- For the first task different arrangements of feed-forward ANNs have been analyzed. The different arrangements include distinct information related to the IMF, solar wind velocity and solar cycle (diurnal and seasonal variations) for the forecasting of the hourly-averaged AE index. The model was tested and presented a good correlation with the reference AE values. The results also suggested an absence of solar cycle influence (assessed herein by means of the $F_{10.7}$ index) on the estimates. In addition, it has evidenced that although the IMF and solar wind velocity provide better performance when combined, the IMF information is dominant when compared to the solar wind velocity for the estimation of the AE index, which is not often highlighted in the discussions of the solar wind forcing of the auroral electrojets. One can observe that although the results show good correlation, the ANN model using only IMF and solar wind velocity as input was not able to reproduce strong variations, mostly underestimating them, which indicates that information of the internal magnetotail state should be included in the input. In order to have better quantitative predictions it is necessary to include information from the dynamics of the magnetosphere, such as historical AE values to account for the loading-unloading processes, which may impose challenges for operational prediction purposes, since the index takes several days to be released by its providers. The results show that the inclusion of the temporal information provided an improvement of up to about 10% on the model performance.

- The second task was to predict LSTIDs activity over mid-latitude Europe during geomagnetic storms events. In this case, the TID activity index has been presented and good correlation between the maximum of the index and the maximum of some geophysical parameters (e.g. Kan-Lee merging electric field and the AE index) has been found. The good correlation with the solar wind parameters indicates that the magnitude of the global solar-wind energy input into the Earth's MIT system is the most relevant for the LSTID generation. Based on this, different approaches for the prediction of the index using solar wind measurements obtained from Lagrangian point L1 were developed and tested. The approaches include a linear regression based model, a MLP neural network and multi-model ensemble, which are compared to the predictions obtained from the persistence model. The proposed approaches presented higher performance than the persistence model for predictions beyond one hour, and shows the potential of predicting LSTIDs from solar wind measurement. The results presented in this work contribute to the monitoring and prediction capabilities of LSTIDs activities and to the better understanding of the LSTIDs' drivers.

The third part of this study is devoted to investigate the effects of Faraday rotation and ionospheric scintillation on the UHF communication systems, taking the AlfaCrux mission as a case study. For the first phenomenon, this investigation shows its impact on the signal attenuation during quiet and disturbed periods. This analysis confirms that for systems using linearly polarized signals, the FR can lead to strong attenuation on the UHF signals during SWe events and even during quiet time periods. Due to these impacts, the AlfaCrux mission employs circular polarized waves in one of the ends of the communication link. This solution leads to an attenuation of 50% on the signal power, which can be compensated at the station level. Despite the attenuation, this solution has the advantage of not requiring to deal with the antennas pointing during the mission operation, which can reduce the complexity of the attitude determination and control system. Regarding the scintillation effects, based on the estimates provided by the GISM, the variability of the scintillation effects in two different regions in Brazil has been presented. The results show a higher level of scintillation during equinoxes. Also, higher levels of scintillation can be expected in the south crest of the EIA. In addition, in this analysis a new methodology to estimate the risk of communication outage for an UHF satellite mission due to ionospheric scintillation has been proposed. The proposed methodology is based on the risk analysis from the decision theory and allows to compute the risk of communication outage taking into account the whole field of view of the ground receiver. Based on this methodology, one can evaluate during the planing of a satellite mission, the risk of communication outage and optimize the communication protocol.

5.2 Recommendations

As presented in the previous sections, the investigations presented in this manuscript can support activities of monitoring and prediction of SWe events, as well the impact of ionospheric scintillation in SATCOM systems. There are still, however, room for improvement in the proposed strategies and models. The investigation on the precursors for the occurrence of LSTIDs during geomagnetic storms revealed the potential of AATR and TEC gradients for this purpose. It is recommended a comprehensive statistical investigation using both indices in order to obtain a quantitative relationship between the magnitude of each precursor and the excited LSTIDs. The investigation of the models for predicting LSTIDs occurrence over mid-latitude Europe have shown that the proposed model can be a valuable tool for such activity. In this case, efforts on making this model operational may also be beneficial for scientific community. In addition, the prediction of 2-dimensional maps of the TID activity index may also extend the applicability of the model and a help to develop better understanding of the excitation mechanisms of the LSTIDs. The proposed methodology for assessing the risk of communication outage due to ionospheric scintillation was developed using simulations from the GISM as the source of S_4 index. Since GISM is a climatological model, some small scale features may not be well represented in the model. The use of real S_4 index measurements on the lower UHF frequency range may be very helpful to improve the performance of the methodology. In this case, the onset of the irregularities and their evolution could be better represented, allowing better estimations of the risk of communication outage.

BIBLIOGRAPHY

Aa, E., Zou, S., Ridley, A., Zhang, S., Coster, A. J., Erickson, E. J., Liu, S., & Ren, J. (2019). Merging of storm time midlatitude traveling ionospheric disturbances and equatorial plasma bubbles. *Space Weather*, *17*, 1–14.

Aguado-Agelet, F., Villa, E. A., Arias-Acuña, M., & Díaz-Otero, F. J. (2019). AOCS Requirements and practical limitations for high-speed communications on small satellites. *International Journal of Aerospace Engineering*, *2019*(5079738), 1–16.

Akasofu, S. (2018). A review on the current understanding in the study of geomagnetic storms. *International Journal of Earth Science and Geophysics*, *4*, 1–13.

Altadill, D., Segarra, A., Blanch, E., Juan, J. M., Paznukhov, V. V., Buresova, D., Galkin, I., Reinisch, B. W., & Belehaki, A. (2020). A method for real-time identification and tracking of traveling ionospheric disturbances using ionosonde data: First results. *Journal of Space Weather and Space Climate*, *10*(2), 1–11.

Amm, O. (1997). Ionospheric elementary current systems in spherical coordinates and their application. *Journal of Geomagnetism and Geoelectricity*, *49*(7), 947–955.

Amm, O., & Viljanen, A. (1999). Ionospheric disturbance magnetic field continuation from the ground to the ionosphere using spherical elementary current systems. *Earth, Planets and Space*, *51*, 431–440.

Ayala Solares, J. R., Wei, H., Boynton, R. J., Walker, S. N., & Billings, S. A. (2016). Modeling and prediction of global magnetic disturbance in near-Earth space: A case study for Kp index using NARX models. *Space Weather*, *14*(10), 899–916.

Bala, R., & Reiff, P. (2012). Improvements in short-term forecasting of geomagnetic activity. *Space Weather*, *10*, 1–11.

Barbarić, D., Vuković, J., & Babić, D. (2018). Link budget analysis for a proposed Cubesat Earth observation mission. *41st International Convention on Information and Communication Technology, Electronics and Microelectronics (MIPRO)*, 0133–0138.

Basu, S., McClure, J. P., Basu, S., Hanson, W. B., & Aarons, J. (1980). Coordinated study of equatorial scintillation and in situ and radar observations of nighttime F region irregularities. *Journal of Geophysical Research: Space Physics*, *85*(A10), 5119–5130.

Basu, S. (2013). The peculiar solar cycle 24 – where do we stand? *Journal of Physics: Conference Series*, *440*, 012001.

Baumjohann, W., & Treumann, R. A. (2012). *Basic space plasma physics* (2nd). Imperial College Press.

Becker, E., & Vadas, S. L. (2020). Explicit global simulation of gravity waves in the thermosphere. *Journal of Geophysical Research: Space Physics*, *125*(10), 1–47.

Belahaki, A., Tsagouri, I., Altadill, D., Blanch, E., Borries, C., Buresova, D., Chum, J., Galkin, I., Juan, J. M., Segarra, A., Timoté, C. C., Tziotziou, K., Verhulst, T. G. W.,

& Watermann, J. (2020). An overview of methodologies for real-time detection, characterisation and tracking of traveling ionospheric disturbances developed in the TechTIDE project. *Journal of Space Weather and Space Climate*, *10*(42), 1–18.

Belehaki, A., Galkin, I., Borries, C., Pintor, P., Altadill, D., Sanz, J., Juan, J. M., Buresova, D., Verhulst, T., Mielich, J., Katamzi-Joseph, Z., Watermann, J., Haralambous, H., & Unger, S. (2019, March). TechTIDE: Warning and mitigation technologies for travelling ionospheric disturbances effects. In Y. Berbers & W. Zwaenepoel (Eds.), *URSI Asia-Pacific Radio Science Conference* (p. 1). URSI.

Béniguel, Y. (2019). Ionospheric scintillations: Indices and modeling. *Radio Science*, *54*(7), 618–632.

Béniguel, Y., & Hamel, P. (2011). A global ionosphere scintillation propagation model for equatorial regions. *Journal of Space Weather and Space Climate*, *1*(1), A04p1–A04p8.

Berdermann, J., Kriegel, M., Banyś, D., Heymann, F., Hoque, M. M., Wilken, V., Borries, C., Heßelbarth, A., & Jakowski, N. (2018). Ionospheric response to the X9.3 flare on 6 September 2017 and its implication for navigation services over Europe. *Space Weather*, *16*(10), 1604–1615.

Blanch, E., Altadill, D., Boška, J., Buresšová, D., & Hernández-Pajares, M. (2005). November 2003 event: Effects on the Earth's ionosphere observed from ground-based ionosonde and GPS data. *Annales Geophysicae*, *23*, 3027–3034.

Bloomfield, D. S., Higgins, P. A., McAtter, R. T. J., & Gallagher, P. T. (2012). Toward reliable benchmarking of solar flare forecasting methods. *The Astrophysical Journal Letters*, *747*(L41), 1–7.

Bobra, M. G., & Couvidat, S. (2015). Solar flare prediction using SDO/HMI vector magnetic field data with a machine-learning algorithm. *The Astrophysical Journal*, *798*(2), 135.

Borges, R. A., Dos Santos, A. C., Reis, W. S., Aguayo, L., Borges, G. A., Karam, M. M., De Sousa, R. B., García, B. F., Botelho, V. M. d. S., Fernández-Carrillo, J. M., Lago Agra, J. M., Aguado-Agelet, F., Borges, J. V. Q. S., Oliveira, A. C. A., Mello, B. T., Avelino, Y. d. C. F., Modesto, V. F., & Brenag, E. C. (2022). The AlfaCrux CubeSat mission description and early results. *Applied Sciences*, *12*(9764), 1–24.

Borries, C., Berdermann, J., Jakowski, N., & Wilken, V. (2015). Ionospheric storms: A challenge for empirical forecast of the total electron content. *Journal of Geophysical Research: Space Physics*, *120*(4), 3175–3186.

Borries, C., Ferreira, A. A., Nykiel, G., & Borges, R. A. (2023). A new index for statistical analyses and prediction of traveling ionospheric disturbances. *Journal of Atmospheric and Solar-Terrestrial Physics*, *247*(106069), 1–13.

Borries, C., Jakowski, N., Kauristie, K., Amm, O., Mielich, J., & Kouba, D. (2017a). On the dynamics of large-scale traveling ionospheric disturbances over Europe on 20 November 2003. *Journal of Geophysical Research: Space Physics*, *122*(1), 1199–1211.

Borries, C., Jakowski, N., Kauristie, K., Amm, O., Mielich, J., & Kouba, D. (2017b). On the dynamics of large-scale traveling ionospheric disturbances over Europe on 20 November 2003. *Journal of Geophysical Research: Space Physics*, *122*(1), 1199–1211.

Borries, C., Jakowski, N., & Wilken, V. (2009). Storm induced large scale TIDs observed in GPS derived TEC. *Annales Geophysicae*, *27*, 1605–1612.

Borries, C., Mahrous, A. M., Ellahouny, N. M., & Badeke, R. (2016a). Multiple ionospheric perturbations during the Saint Patrick's Day storm 2015 in the European-African sector. *Journal of Geophysical Research: Space Physics*, *121*(11), 11, 333–11, 345.

Borries, C., Mahrous, A. M., Ellahouny, N. M., & Badeke, R. (2016b). Multiple ionospheric perturbations during the Saint Patrick's Day storm 2015 in the European-African sector [2016JA023178]. *Journal of Geophysical Research: Space Physics*, *121*(11), 11, 333–11, 345.

Bothmer, W., & Daglis, J. A. (2007). *Space weather: Physics and effects* (1st). Springer-Verlag Berlin Heidelberg.

Bowman, G. G., & Mortimer, I. K. (2011). Some aspects of large-scale travelling ionospheric disturbances which originate at conjugate locations in auroral zones, cross the equator and sometimes encircle the Earth. *Annales Geophysicae*, *29*(12), 2203–2210.

Boynton, R. J., Balikhin, M. A., Billings, S. A., Sharma, A. S., & Amariutei, O. A. (2011). Data derived NARMAX Dst model. *Annales Geophysicae*, *29*, 965–971.

Brittain, J. E. (2010). Electrical Engineering Hall of Fame: Edward V. Appleton [Scanning Our Past]. *Proceedings of the IEEE*, *98*(9), 1681–1682.

Cade, W. B. (2013). The first space weather prediction. *Space Weather*, *11*(6), 330–332.

Cade, W. B., & Chan-Park, C. (2015). The origin of space weather. *Space Weather*, *13*(2), 99–103.

Calais, E., & Minster, J. B. (1995). GPS detection of ionospheric perturbations following the January 17, 1994, Northridge Earthquake. *Geophysical Research Letters*, *22*(9), 1045–1048.

Camporeale, E. (2019a). The challenge of machine learning in space weather: Nowcasting and forecasting. *Space Weather*, *17*(8), 1166–1207.

Camporeale, E. (2019b). The challenge of machine learning in space weather: Nowcasting and forecasting. *Space Weather*, 1166–1207.

Cander, L. R. (2019). *Ionospheric space weather* (1st). Springer.

Cesaroni, C., Spogli, L., Alfonsi, L., De Francesci, G., Ciraolo, L., Monico, J. F. G., Scotto, C., Romano, V., Aquino, M., & Bougard, B. (2015). L-band scintillations and calibrated total electron content gradients over Brazil during the last solar minimum. *Journal of Space Weather and Space Climate*, *5*(A36), 1–11.

Chen, G., Zhou, C., Liu, Y., Zhao, J., Tang, Q., Wang, X., & Zhao, Z. (2019). A statistical analysis of medium-scale traveling ionospheric disturbances during 2014–2017 using the Hong Kong CORS network. *Earth, Planets and Space*, *71*(52), 1–14.

Cherniak, I., & Zakharenkova, I. (2015). Dependence of the high-latitude plasma irregularities on the auroral activity indices: a case study of 17 March 2015 geomagnetic storm. *Earth, Planets and Space*, *67*(151), 1–12.

Cherniak, I., & Zakharenkova, I. (2018a). Large-scale traveling ionospheric disturbances origin and propagation: Case study of the December 2015 geomagnetic storm. *Space Weather*, *16*, 1377–1395.

Cherniak, I., & Zakharenkova, I. (2018b). Large-scale traveling ionospheric disturbances origin and propagation: Case study of the December 2015 geomagnetic storm. *Space Weather*, *16*(9), 1377–1395.

Cherniak, I., Krankowski, A., & Zakharenkova, I. (2018). ROTI Maps: a new IGS ionospheric product characterizing the ionospheric irregularities occurrence. *GPS Solutions*, *22*(69), 1–12.

Chou, M.-Y., Pedatella, N. M., Wu, Q., Huba, J. D., Lin, C. C. H., Schreiner, W. S., Braun, J. J., Eastes, R. W., & Yue, J. (2020). Observation and simulation of the development of equatorial plasma bubbles: Post-sunset rise or upwelling growth? *Journal of Geophysical Research: Space Physics*, *125*(12), 1–14.

Chum, J., & Podolská, K. (2018). 3D Analysis of GW propagation in the ionosphere. *Geophysical Research Letters*, *45*(21), 11, 562–11, 571.

Ciraolo, L., Azpilicueta, F., Brunini, C., Meza, A., & Radicella, S. M. (2007). Calibration errors on experimental slant total electron content (TEC) determined with GPS. *Journal of Geodesy*, *81*(2), 111–120.

Correia, E., Muella, M. T. A. H., Alfonsi, L., Prol, F. S. P., & Camargo, P. O. (2018). GPS Scintillations and total electron content climatology in the Southern American sector. In *Accuracy of GNSS methods*. IntechOpen.

Cristóbal, N. P., & Emami, M. R. (2019). CubeSat mission: from design to operation. *Applied Sciences*, *9*(15), 1–24.

Curto, J. J., Marsal, S., Blanch, E., & Altadill, D. (2018). Analysis of the solar flare effects of 6 September 2017 in the ionosphere and in the Earth's magnetic field using spherical elementary current systems. *Space Weather*, *16*(11), 1709–1720.

Davis, T. N., & Sugiura, M. (1966). Auroral Electrojet activity index AE and its universal time variations. *Journal of Geophysical Research: Space Physics*, *71*, 785–801.

De Paula, E. R., Rodrigues, F. S., Iyer, K. N., Kantor, I. J., Abdu, M. A., Kintner, P. M., Ledvina, B. M., & Kil, H. (2003). Equatorial anomaly effects on GPS scintillations in Brazil. *Advances in Space Research*, *31*(3), 749–754.

Detman, T., & Joselyn, J. (1999). Real-time Kp predictions from ACE real time solar wind. *AIP Conference Proceedings*, *471*(1), 729–732.

Devos, A., Verbeeck, C., & Robbrecht, E. (2014). Verification of space weather forecasting at the Regional Warning Center in Belgium. *Journal of Space Weather and Space Climate*, *4*(A29), 1–15.

Dimmock, A. P., Rosenqvist, L., Hall, J.-O., Viljanen, A., Yordanova, E., Honkonen, I., André, M., & Sjöberg, E. C. (2019). The GIC and geomagnetic response over Fennoscandia to the 7-–8 September 2017 geomagnetic storm. *Space Weather*, *17*(7).

Dungey, J. W. (1961). Interplanetary magnetic field and the auroral zones. *Physical Review Letters*, *6*(2), 47–48.

Eastes, R. W., Solomon, S. C., Daniell, R. E., Anderson, D. N., Burns, A. G., England, S. L., Martinis, C. R., & McClintock, W. E. (2019). Global-scale observations of the Equatorial Ionization Anomaly. *Geophysical Research Letters*, *46*(16), 9318–9326.

Erickson, G. M., Spiro, R. W., & Wolf, R. A. (1991). The physics of the Harang discontinuity. *Journal of Geophysical Research: Space Physics*, *96*(A2), 1633–1645.

ESA. *The structure of the sun: Cesar's booklet.* Booklet. https://cesar.esa.int/upload/201809/booklet_the_suns_structure.pdf, 2023.

Esenbuğa, O., Hauschild, A., & Steigenberger, P. (2023). Recent fex power changes. *GPS Solutions*, *27*(104), 1–14.

Fernandez, L., Ruiz-De-Azua, J. A., Calveras, A., & Camps, A. (2020). Assessing LoRa for satellite-to-Earth communications considering the impact of ionospheric scintillation. *IEEE Access*, *8*, 165570–165582.

Ferreira, A. A., & Borges, R. A. (2021, March). Performance analysis of distinct feed-forward neural networks structures on the AE index prediction. In *Proceedings of the IEEE Aerospace Conference 2021* (pp. 1–7). IEEE.

Ferreira, A. A., Borges, R. A., Reis, L. R., Borries, C., & Vasylyev, D. (2022). Investigation of ionospheric effects in the planning of the AlfaCrux UHF satellite communication system. *IEEE Access*, *10*, 65744–65759.

Ferreira, A. A., Borries, C., Xiong, C., Borges, R. A., Mielich, J., & Kouba, D. (2020). Identification of potential precursors for the occurrence of Large-Scale Traveling Ionospheric Disturbances in a case study during September 2017. *Journal of Space Weather and Space Climate*, *10*, 32.

Figueiredo, C. A. O. B., Wrasse, C. M., Takahashi, H., Otsuka, Y., Shiokawa, K., & Barros, D. (2017). Large-scale traveling ionospheric disturbances observed by GPS dTEC maps over North and South America on Saint Patrick's Day storm in 2015. *Journal of Geophysical Research: Space Physics*, *122*, 4755–4763.

Foster, J. C., & Vo, H. B. (2002). Average characteristics and activity dependence of the subauroral polarization stream. *Journal of Geophysical Research: Space Physics*, *107*(A12), SIA 16-1-SIA 16–10.

Galkin, I., & Reinisch, B. (2008). The new ARTIST 5 for all digisondes. *Ionosonde Network Advisory Group Bulletin*, *69*, 1–8.

Galuscak, R., & Hazdra, P. (2006). Circular polarization and polarization losses. *DuBus*, 8–23.

Gamache, R. R., & Reinisch, B. W. (1990). *Ionospheric characteristics for archiving at the world data centers* (tech. rep.). Center for Atmospheric Research, University of Lowell.

Gerrard, T. L., Davis, A. J., Hammond, J., & Sears, S. R. (1998). The ACE Science Center. *Space Science Reviews*, *86*, 649–663.

Ghosh, P., Otsuka, Y., Mani, S., & Shinagawa, H. (2020). Day-to-day variation of pre-reversal enhancement in the equatorial ionosphere based on GAIA model simulations. *Earth, Planets and Space*, *72*(1), 1–8.

Gleisner, H., & Lundstedt, H. (1997). Response of the auroral electrojets to the solar wind modeled with neural networks. *Journal of Geophysical Research*, *102*(A7), 14269–14278.

Glover, D. R. (2017). Satellite radio communications fundamentals and link budgets. In J. N. Pelton, S. Madry, & S. Camacho-Lara (Eds.), *Handbook of satellite applications* (2nd, pp. 431–462). Springer.

Gonzales, W. D., Joselyn, J. A., Kamide, Y., Kroehl, H. W., Rostoker, G., Tsurutani, B. T., & Vasyliunas, V. M. (1994). What is a geomagnetic storm? *Journal of Geophysical Research*, *99*(A4), 5771–5792.

Goodman, J. M. (2005). *Space weather & telecommunications* (1st). Springer US.

Goossens, M. (2003). *An introduction to plasma astrophysics and magnetohydrodynamics* (1st). Springer Dordrecht.

Gu, Y., Wei, H., Boynton, R. J., Walker, S. N., & Balikhin, M. A. (2019). System identification and data-driven forecasting of AE index and prediction uncertainty analysis using a new cloud-NARX model. *Journal of Geophysical Research : Space Physics*, *124*, 248–263.

Gündüzham, E., & Brown, K. D. (2015). Narrowband satellite communications: Challenges and emerging solutions [Available: https://www.jhuapl.edu/Content/techdigest/pdf/V33-N01/33-01-Gunduzhan.pdf]. *Johns Hopkins APL Technical Digest*, *33*(1), 52–56.

Guo, K., Aquino, M., & Vadakke Veettil, S. (2019). Ionospheric scintillation intensity fading characteristics and GPS receiver tracking performance at low latitudes. *GPS Solutions*, *23*(43), 1–12.

Habarulema, J. B., Katamzi, Z. T., Yizengaw, E., Yamazaki, Y., & Seemala, G. (2016). Simultaneous storm time equatorward and poleward large-scale TIDs on a global scale. *Geophysical Research Letters*, *43*(13), 6678–6686.

Habarulema, J. B., McKinnell, L. A., & Opperman, B. D. L. (2011). Regional GPS TEC modeling; Attempted spatial and temporal extrapolation of TEC using neural networks. *Journal of Geophysical Research*, *116*(A04314), 1–14.

Hagan, M. T., & Menhaj, M. B. (1994). Training feedforward networks with the Marquardt algorithm. *IEEE Transactions on Neural Networks*, *5*(6), 989–993.

Hargreaves, J. (1992). *The solar-terrestrial environment* (21st). Cambridge University Press.

Hasirci, Z., Cavdar, I. H., & Ozturk, M. (2016). Single tree vegetation depth estimation tool for satellite services link design. *Radioengineering*, *25*(1), 140–147.

Haykin, S. (2009). *Neural networks and learning machines* (3rd). Pearson.

He, M., Vogt, J., Lühr, H., & Sorbalo, E. (2014). Local time resolved dynamics of field-aligned currents and their response to solar wind variability. *Journal of Geophysical Research: Space Physics*, *119*(7), 5305–5315.

Heilig, B., & Lühr, H. (2013). New plasmasphere model derived from CHAMP field-aligned current signatures. *Annales Geophysicae*, *31*(3), 529–539.

Hemadeh, I. A., Satyanarayana, K., El-Hajjar, M., & Hanzo, L. (2018). Millimeter-wave communications: Physical channel models, design considerations, antenna constructions, and link-budget. *IEEE Communications Surveys & Tutorials*, *20*(2), 870–913.

Hernández-Pajares, M., Juan, J. M., Sanz, J., Aragń-Àngel, À., Garcá-Rigo, A., Salazar, D., & Escudero, M. (2011). The ionosphere: effects, GPS modeling and the benefits for space geodetic techniques. *Journal of Geodesy*, *85*(1432-1394), 887–907.

Hernández-Pajares, M., Juan, M., & Sanz, J. (2006). Medium-scale traveling ionospheric disturbances affecting GPS measurements: Spatial and temporal analysis. *Journal of Geophysical Research*, *111*(A07S11), 1–13.

Hines, C. O. (1960). Internal atmospheric gravity waves at ionospheric heights. *Canadian Journal of Physics*, *38*, 1441–1481.

Hocke, K., & Schlegel, K. (1996). A review of atmospheric gravity waves and travelling ionospheric disturbances: 1982-1995. *Annales Geophysicae*, *14*, 917–940.

Hoque, M. M., & Jakowski, N. (2012). Ionospheric propagation effects on GNSS Signals and new correction approaches. In S. Jin (Ed.), *Global navigation satellite systems*. IntechOpen.

Hunsucker, R. D. (1982). Atmospheric gravity waves generated in the high-latitude ionosphere: A review. *Reviews of Geophysics*, *20*(2), 239–315.

ITU. (2017). *Recommendation ITU-R P.837-7: Characteristics of precipitation for propagation modelling* (tech. rep.). International Telecommunications Union. Geneva.

ITU. (2019). *Recommendation ITU-R P.531-14: Ionospheric propagation data and prediction methods required for the design of satellite networks and systems* (tech. rep.). International Telecommunications Union. Geneva.

Jacobsen, K. S. (2014). The impact of different sampling rates and calculation time intervals on ROTI values. *Journal of Space Weather and Space Climate*, *4*(A33), 1–9.

Jacobsen, K. S., & Dähnn, M. (2014). Statistics of ionospheric disturbances and their correlation with GNSS positioning errors at high latitudes. *Journal of Space Weather and Space Climate*, *4*(A27), 1–10.

Jakowski, N. (1996). TEC Monitoring by using satellite positioning systems. In H. Kohl, R. Rüster, & K. Schlegel (Eds.), *Modern ionospheric science* (1st ed., pp. 371–390). European Geophysical Society.

Jakowski, N., Béniguel, Y., Franceschi, G. D., Hernandez-Pajares, M., Jacobsen, K. S., Stanislawska, I., Tomasik, L., Warnant, R., & Wautelet, G. (2012). Monitoring, tracking and forecasting ionospheric perturbations using GNSS techniques. *Journal of Space Weather and Space Climate*, *2*(A22), 1–14.

Jehle, M., Rüegg, M., Small, D., Meier, E., & Nüesch, D. (2005). Estimation of ionospheric TEC and Faraday rotation for L-band SAR. In K. Schäfer, A. T. Comerón, J. R. Slusser, R. Picard, M. R. Carleer, & N. Sifakis (Eds.), *Remote Sensing of Clouds and the Atmosphere X* (pp. 252–260, Vol. 5979). International Society for Optics; Photonics.

Jin, H., Zou, S., Chen, G., Yan, C., Zhang, S., & Yang, G. (2018). Formation and evolution of low-latitude f region field-aligned irregularities during the 7-8 September 2017 Storm: Hainan coherent scatter phased array radar and digisonde observations. *Space Weather*, *16*(6), 648–659.

Johnstone, A. (2020). *Cubesat develop specification rev. 14*. California Polytechnic State University. California, USA.

Juan, J. M., Aragon–Angel, A., Sanz, J., González–Casado, G., & Rovira-Garcia, A. (2017). A method for scintillation characterization using geodetic receivers operating at 1 Hz. *Journal of Geodesy*, *91*, 1383–1397.

Juan, J. M., Sanz, J., Rovira-Garcia, A., González-Casado, G., Ibáñez, D., & Orus Perez, R. (2018). AATR an ionospheric activity indicator specifically based on GNSS measurements. *Journal of Space Weather and Space Climate*, *8*(A14), 1–11.

Kelley, M. C. (2009). *The Earth's ionosphere: Plasmas physics & electrodynamics* (2nd). Academic Press.

Kelley, M. C. (2011). On the origin of mesoscale TIDs at midlatitudes. *Annales Geophysicae*, *29*(2), 361–366.

Kelly, M. A., Comberiate, J. M., Miller, E. S., & Paxton, L. J. (2014). Progress toward forecasting of space weather effects on UHF SATCOM after Operation Anaconda. *Space Weather*, *12*(10), 601–611.

Kim, J., Kwak, Y., YongHa, K., Su-In, M., Se-Heon, J., & Yun, J. (2021). Potential of regional ionosphere prediction using a long short-term memory deep learning algorithm specialized for geomagnetic storm period. *19*, 1–20.

Kirchengast, G. (1996). Elucidation of the physics of the gravity wave-TID relationship with the aid of theoretical simulation. *Journal of Geophysical Research*, *101*(A6), 13353–13368.

Kirchengast, G., Hocke, K., & Schlegel, K. (1996). The gravity wave-TID relationship: Insight via theoretical model-EISCAT data comparison. *Journal of Atmospheric and Terrestrial Physics*, *58*(1–4), 233–243.

Kotake, N., Otsuka, Y., Ogawa, T., Tsugawa, T., & Saito, A. (2007). Statistical study of medium-scale traveling ionospheric disturbances observed with the GPS networks in Southern California. *Earth Planets Space*, *59*, 95–102.

Kotake, N., Otsuka, Y., Tsugawa, T., Ogawa, T., & Saito, A. (2006). Climatological study of GPS total electron content variations caused by medium-scale traveling ionospheric disturbances. *Journal of Geophysical Research: Space Physics*, *111*, A04306.

Koulouri, A., Smith, N. D., Vani, B. C., Rimpiläinen, V., Astin, I., & Forte, B. (2020). Methodology to estimate ionospheric scintillation risk and their contribution to position dilution of precision on the ground. *Journal of Geodesy*, *94*(22), 1–22.

Krall, J., Huba, J. D., Ossakow, S. L., Joyce, G., Makela, J. J., Miller, E. S., & Kelley, M. C. (2011). Modeling of equatorial plasma bubbles triggered by non-equatorial traveling ionospheric disturbances. *Geophysical Research Letters*, *38*(8).

Lawrence, R. S., Little, C. G., & Chivers, H. J. A. (1964). A survey of ionospheric effects upon Earth-space radio propagation. *Proceedings of the IEEE*, *52*(1), 4–27.

Lepping, R., Acũna, M. H., Burlage, L. F., Farrell, W. M., Slavin, J. A., Schatten, K. H., Mariani, F., Ness, N. F., M., N. F., Whang, Y. C., Byrnes, J. B., Kennon, R. S., Panetta, P. V., Scheifele, J., & Worley, E. M. (1995). The WIND magnetic field investigation. *Space Science Reviews*, *71*, 207–229.

Liu, J., Zhang, D., Coster, A. J., Zhang, S., Ma, G., Hao, Y., & Xiao, Z. (2019). A case study of the large-scale traveling ionospheric disturbances in the eastern Asian sector during the 2015 St. Patrick's Day geomagnetic storm. *Annales Geophysicae*, *37*, 673–687.

LODESTAR. (2022). *The AlfaCrux mission*. Retrieved November 1, 2022, from https://lodestar.aerospace.unb.br/projects/alfacrux

Lopez, R., Bhattarai, S., Bruntz, R., Pham, K., Wiltberger, M., Lyon, J., Deng, Y., & Huang, Y. (2012). The role of dayside merging in generating the ionospheric potential during the whole heliospheric interval. *Journal of Atmospheric and Solar-Terrestrial Physics*, *83*, 63–69.

Lu, G., Zakharenkova, I., Cherniak, I., & Dang, T. (2020). Large-scale ionospheric disturbances during the 17 March 2015 storm: A model-data comparative study. *Journal of Geophysical Research: Space Physics*, *125*(5).

Lühr, H., Warnecke, J. F., & Rother, M. K. A. (1996). An algorithm for estimating field-aligned currents from single spacecraft magnetic field measurements: a diagnostic tool applied to Freja satellite data. *IEEE Transactions on Geoscience and Remote Sensing*, *34*(6), 1369–1376.

Maimaiti, M., Kunduri, B., Ruohoniemi, J. M., Baker, J. B. H., & House, L. L. (2019). A deep learning-based approach to forecast the onset of magnetic substorms. *Space Weather*, *17*(11), 1534–1552.

Mavromichalaki, H., Gerontidou, M., Paschalis, P., Paouris, E., Tezari, A., Sgouropoulos, C., Crosby, N., & Dierckxsens, M. (2018). Real-time detection of the ground level enhancement on 10 September 2017 by A.Ne.Mo.S.: System report. *Space Weather*, *16*(11), 1797–1805.

Mayer, C., Belabbas, B., Jakowski, N., & Meurer, M. (2009, September). Ionosphere threat space model assessment for GBAS. In *Proceedings of the 22nd International Technical Meeting of the Satellite Division of The Institute of Navigation* (pp. 1091–1099). ION GNSS+.

Mayer, C., Jakowski, N., Borries, C., Pannowitsch, T., & Belabbas, B. (2008, December). Extreme ionospheric conditions over Europe observed during the last solar cycle. In *4th ESA Workshop on Satellite Navigation User Equipment Technologies, ESTEC*. ESA.

Mendillo, M. (2006). Storms in the ionosphere: Patterns and processes for total electron content. *Reviews of Geophysics*, *44*(4), 1–47.

Milan, S., Clausen, L. B. N., Coxon, J. C., Carter, J. A., Walach, M.-T., Laundal, K., Østegaard, N., Tenfjord, P., Reistad, J., Snekvik, K., Korth, H., & Anderson, B. (2017). Overview of solar wind-magnetosphere-ionosphere-atmosphere coupling and the generation of magnetospheric currents. *Space Science Reviews*, *206*, 547–579.

Mishev, A. L., & Usoskin, I. G. (2018). Assessment of the radiation environment at commercial jet-flight altitudes during GLE 72 on 10 September 2017 using neutron monitor data. *Space Weather*, *16*(12), 1921–1929.

Mosna, Z., Kouba, D., Knizova, P. K., Buresova, D., Chum, J., Sindelarova, T., Urbar, J., Boska, J., & Saxonbergova–Jankovicova, D. (2020). Ionospheric storm of September 2017 observed at ionospheric station Pruhonice, the Czech Republic. *Advances in Space Research*, *65*(1).

Mukhopadhyay, A., Welling, D. T., Liemohn, M. W., Ridley, A. J., Chakraborty, S., & Anderson, B. J. (2020). Conductance model for extreme events: Impact of auroral conductance on space weather forecasts. *Space Weather*, *18*(11), 1–27.

Murray, S. A. (2018). The importance of ensemble techniques for operational space weather forecasting. *Space Weather*, *16*(7), 777–783.

Negale, M. R., Taylor, M. J., Nicolls, M. J., Vadas, S. L., Nielsen, K., & Heinselman, C. J. (2018). Seasonal propagation characteristics of MSTIDs observed at high latitudes over central Alaska Using the Poker Flat incoherent scatter radar. *Journal of Geophysical Research: Space Physics*, *123*(7), 5717–5737.

Newell, P. T., Sotirelis, T., Liou, K., Meng, C.-I., & Rich, F. J. (2007). A nearly universal solar wind-magnetosphere coupling function inferred from 10 magnetospheric state variables. *Journal of Geophysical Research: Space Physics*, *112*(A1), 1–16.

NOAA. (2021). Geomagnetic storms [Accessed: 2021-02-04].

Obana, Y., Maruyama, N., Shinbori, A., Hashimoto, K. K., Fedrizzi, M., Nosé, M., Otsuka, Y., Nishitani, N., Hori, T., Kumamoto, A., Tsuchiya, F., Matsuda, S., Matsuoka, A., Kasahara, A., Y.and Yoshikawa, Miyoshi, Y., & Shinohara, I. (2019). Response of the ionosphere-plasmasphere coupling to the September 2017 storm: What erodes the plasmasphere so severely? *Space Weather*, *17*(6), 861–876.

Oberoi, D., & Lonsdale, C. J. (2012). Media responsible for Faraday rotation: A review. *Radio Science*, *47*(6), 1–11.

Oppe, S. (1988). The concept of risk: A decision theoretic approach. *Ergonomics*, *31*(4), 435–440.

Otsuka, Y., Suzuki, K., Nakagawa, S., Nishioka, M., Shiokawa, K., & Tsugawa, T. (2013). GPS observations of medium-scale traveling ionospheric disturbances over Europe. *Annales Geophysicae*, *31*, 163–172.

Pallocchia, G., Amata, E., Consolini, G., Marcucci, M. F., & Bertello, I. (2008). AE index forecast at different time scales through an ANN algorithm based on L1 IMF and plasma measurements. *Journal of Atmospheric and Solar-Terrestrial Physics*, *70*, 663–668.

Paulescu, M., Paulescu, E., & Badescu, V. (2021). Chapter 9 - nowcasting solar irradiance for effective solar power plants operation and smart grid management. In R. Deo, P. Samui, & S. S. Roy (Eds.), *Predictive modelling for energy management and power systems engineering* (pp. 249–270). Elsevier.

Paznukhov, V. V., Altadill, D., & Reinisch, B. W. (2009). Experimental evidence for the role of the neutral wind in the development of ionospheric storms in midlatitudes. *Journal of Geophysical Research*, *114*(A12319), 1–13.

Pelton, J. N. (2017). History of satellite communications. In J. N. Pelton, S. Madry, & S. Camacho-Lara (Eds.), *Handbook of satellite applications* (2nd, pp. 31–72). Springer Nature.

Pelton, J. N., & Madry, S. (2017). Glossary of terms. In J. N. Pelton, S. Madry, & S. Camacho-Lara (Eds.), *Handbook of satellite applications* (2nd, pp. 1481–1519). Springer Nature.

Pi, X., Mannucci, A. J., Lindqwister, U. J., & Ho, C. M. (1997). Monitoring of global ionospheric irregularities using the worldwide GPS network. *Geophysical Research Letters*, *24*(18), 2283–2286.

Piggott, W., & Rawer, K. (1972). *U.R.S.I. handbook of ionogram interpretation and reduction* (2nd). WDC-A for STP, NOAA.

Pokhotelov, D., Mitchell, C. N., Spencer, P. S. J., Hairston, M. R., & Heelis, R. A. (2008). Ionospheric storm time dynamics as seen by GPS tomography and in situ spacecraft observations. *Journal of Geophysical Research*, *113*(A00A16), 1–7.

Poniatowski, M., & Nykiel, G. (2020). Degradation of Kinematic PPP of GNSS stations in central Europe caused by medium-scale traveling ionospheric disturbances during the St. Patrick's Day 2015 geomagnetic storm. *Remote Sensing*, *12*(21), 1–15.

Popescu, O., Harris, J. S., & Popescu, D. C. (2016). Designing the communication subsystem for nanosatellite CubeSat missions: Operational and implementation perspectives. *SoutheastCon 2016*, 1–5.

Pradipta, R., & Doherty, P. H. (2015). Assessing the occurrence pattern of large ionospheric TEC gradients over the Brazilian airspace. *Navigation: Journal of The Institute of Navigation*, *63*(3), 335–343.

Pratt, T., & Allnutt, J. (2020). *Satellite communications* (3rd). Wiley.

Prol, F. S. (2019). *IonMAP: Data assimilation system for three-dimensional imaging of the ionosphere in Brazil* [Doctoral dissertation, São Paulo State University].

Prol, F. S., Ferre, R. M., Saleem, Z., Välisuo, P., Pinell, C., Lohan, E. S., Elsanhoury, M., Elmusrati, M., Islam, S., Çelikbilek, K., Selvan, K., Yliaho, J., Rutledge, K., Ojala, A., Ferranti, L., Praks, J., Bhuiyan, M. Z. H., Kaasalainen, S., & Kuusniemi, H. (2022). Positioning, navigation, and timing (pnt) through low earth orbit (leo) satellites: A survey on current status, challenges and opportunities. *IEEE Access*, *10*, 83971–84002.

Prölss, G. W. (2006). Characterising the ionosphere. Ionospheric F-region storms: unsolved problems. In *Meeting Proceedings RTO-MP-IST-056* (pp. 10-1 –10-20).

Pulkkinen, A., Amm, O., & Viljanen, A. (2003). Ionospheric equivalent current distributions determined with the method of spherical elementary current systems. *Journal of Geophysical Research: Space Physics*, *108*(A2), 1–9.

Pulkkinen, T. (2007). Space weather: Terrestrial perspective. *Living Reviews in Solar Physics*, *4*, 1–60.

Radicella, S. M. (2009). The NeQuick model genesis, uses and evolution. *Annals of Geophysics*, *52*(3-4), 417–422.

Redmon, R. J., Denig, W. F., Kilcommons, L. M., & Knipp, D. J. (2017). New DMSP database of precipitating auroral electrons and ions. *Journal of Geophysical Research: Space Physics*, *122*(8), 9056–9067.

Reikard, G. (2018a). Forecasting space weather over short horizons: Revised and updated estimates. *New Astronomy*, 62–69.

Reikard, G. (2018b). Forecasting space weather over short horizons: Revised and updated estimates. *New Astronomy*, *62*, 62–69.

Reinisch, B., Galkin, I., Belehaki, A., Paznukhov, V., Huang, X., Altadill, D., Buresova, D., Mielich, J., Verhulst, T., Stankov, S., Blanch, E., Kouba, D., Hamel, R., Kozlov, A., Tsagouri, I., Mouzakis, A., Messerotti, M., Parkinson, M., & Ishii, M. (2018). Pilot ionosonde network for identification of traveling ionospheric disturbances. *Radio Science*, *53*(3), 365–378.

Reinisch, B., & Galkin, L. (2011). Global Ionospheric Radio Observatory (GIRO). *Earth, Planets and Space*, *63*, 377–381.

Reis, L. R. (2021). *Análise de fenômenos ionosféricos no planejamento de enlaces de comunicação em missões espaciais* [Master's thesis, University of Brasília].

Reis, L. R., Borges, R. A., Leite, J. P., Cappelleti, C., & Battistini, S. (2020, January). An overview of the AlfaCrux CubeSat mission for narrowband communication. In *Proceedings of the 5th IAA Conference on University Satellite Missions and CubeSat Workshop 2020*. International Academy of Astronautics (IAA).

Richmond, A. D. (1995). Ionospheric electrodynamics using magnetic Apex coordinates. *Journal of Geomagnetism and Geoelectricity*, *47*(2), 191–212.

Ritter, P., Lühr, H., & Rauberg, J. (2013). Determining field-aligned currents with the Swarm constellation mission. *Earth, Planets and Space*, *65*(9), 1285–1294.

Rostoker, G., Akasofu, S. I., Baumjohann, W., Kamide, Y., & McPherron, R. L. (1988). The roles of direct input of energy from the solar wind and unloading of stored magnetotail energy in driving magnetospheric substorms. *Space Science Reviews*, *46*, 93–111.

Saeed, N., Elzanaty, A., Almorad, H., Dahrouj, H., Al–Naffouri, T. Y., & Alouini, M.-S. (2020). CubeSat communications: Recent advances and future challenges. *IEEE Communications Surveys & Tutorials*, *22*(3), 1839–1862.

Sato, H., Jakowski, N., Berdermann, J., Jiricka, K., Heßelbarth, A., Banyś, D., & Wilken, V. (2019). Solar radio burst events on 6 September 2017 and its impact on GNSS signal frequencies. *Space Weather*, *17*(6), 816–826.

Savastano, G., Komjathy, A., Verkhoglyadova, O., A., M., Crespi, M., Wei, Y., & Mannucci, A. J. (2017). Real-Time detection of tsunami ionospheric disturbances with a stand-alone GNSS receiver: A preliminary feasibility demonstration. *Scientific Reports*, *7*(46607), 1–10.

Schrijver, J. C., Kauristie, K., D.Aylward, A., Denardini, C. M., Gibson, S. E., Glover, A., Gopalswamy, N., Grande, M., Hapgood, M., Heynderickx, D., Jakowski, N., Kalegaev, V. V., Lapenta, G., Linker, J. A., Liu, S., Mandrini, C. H., Mann, I. R., Nagatsuma, T., Nandy, D., … Vilmer, N. (2015). Understanding space weather to shield society: A global road map for 2015–2025 commissioned by COSPAR and ILWS. *Advances in Space Research*, *55*(12), 2745–2807.

Shimeis, A., Borries, C., Amory-Mazaudier, C., Fleury, R., Mahrous, A., Hassan, A., & Nawar, S. (2015). TEC variations along an East Euro-African chain during 5th April 2010 geomagnetic storm. *Advances in Space Research*, *55*(9), 2239–2247.

Shiokawa, K., Otsuka, Y., & Ogawa, T. (2009). Propagation characteristics of nighttime mesospheric and thermospheric waves observed by optical mesosphere thermosphere imagers at middle and low latitudes. *Earth, Planets and Space*, *61*, 479–491.

Singh, M., & Bettenhausen, M. H. (2011). An accurate and efficient algorithm for Faraday rotation corrections for spaceborne microwave radiometers. *Radio Science*, *46*(4), 1–16.

Sobral, J. H., Abdu, M. A., Takahashi, H., Taylor, M. J., de Paula, E. R., Zamlutti, C. J., de Aquino, M. G., & Borba, G. L. (2002). Ionospheric plasma bubble climatology over Brazil based on 22 years (1977–1998) of 630nm airglow observations. *Journal of Atmospheric and Solar-Terrestrial Physics*, *64*(12-14), 1517–1524.

Song, Q., Ding, F., Wan, W., Ning, B., & Liu, L. (2012). Global propagation features of large-scale traveling ionospheric disturbances during the magnetic storm of 7-10 November 2004. *Annales Geophysicae*, *30*, 683–694.

Song, Q., Ding, F., Wan, W., Ning, B., Liu, L., Zhao, B., Li, Q., & Zhang, R. (2013). Statistical study of large-scale traveling ionospheric disturbances generated by the solar terminator over China. *Journal of Geophysical Research: Space Physics*, *118*(7), 4583–4593.

Stix, M. (2002). *The Sun: An Introduction* (2nd). Springer Berlin.

Suresh, V., Pinsolle, E., Lupien, C., Martz-Oberlander, T. J., Lilly, M. P., Reno, J. L., Gervais, G., Szkopek, T., & Reulet, B. (2020). Quantitative measurement of giant and quantized microwave faraday rotation. *Phys. Rev. B*, *102*, 085302.

Takahashi, H., Wrasse, C. M., Figueiredo, C. A. O. B., Barros, D., Abdu, M. A., Otsuka, Y., & Shiokawa, K. (2018). Equatorial plasma bubble seeding by MSTIDs in the ionosphere. *Progress in Earth and Planetary Science*, *5*(32), 1–13.

Takalo, J., & Timonen, J. (1997). Neural network prediction of AE data. *Geophysical Research Letters*, *24*, 2403–2406.

Tapping, K. F. (2013). The 10.7cm solar radio flux (F10.7). *Space Weather*, *11*(7), 394–406.

Thaganyana, G. P., Habarulema, J. B., Ngwira, C., & Azeem, I. (2022). Equatorward medium to large-scale traveling ionospheric disturbances of high latitude origin during quiet conditions. *Journal of Geophysical Research: Space Physics*, *127*(3), 1–15.

Tsugawa, T., Otsuka, Y., Coster, A. J., & Saito, A. (2007). Medium-scale traveling ionospheric disturbances detected with dense and wide TEC maps over North America. *Geophysical Research Letters*, *34*(22), 1–5.

Tsugawa, T., Saito, A., & Otsuka, Y. (2004). A statistical study of large-scale traveling ionospheric disturbances using the GPS network in Japan. *Journal of Geophysical Research: Space Physics*, *109*(A6), 1–11.

Tsugawa, T., Saito, A., Otsuka, Y., & Yamamoto, M. (2003). Damping of large-scale traveling ionospheric disturbances detected with GPS networks during the geomagnetic storm. *Journal of Geophysical Research*, *108*(A3), 1–14.

Tsurutani, B. T., & Gonzales, W. D. (1995). The efficiency of viscous interaction between the solar wind and the magnetosphere during intense northward IMF events. *Geophysical Research Letters*, *22*(6), 663–666.

Ulaby, F. T., Moore, R. K., & Fung, A. K. (1981). *Microwave remote sensing. Active and passive* (1st, Vol. 1). Addison-Wesley Publishing Company.

Van der Kamp, M., Pokhotelov, D., & Kauristie, K. (2014). TID characterised using joint effort of incoherent scatter radar and GPS. *Ann. Geophys.*, *32*, 1511–1532.

Vani, B. C., Shimabukuro, M. H., & Galera Monico, J. F. (2017). Visual exploration and analysis of ionospheric scintillation monitoring data: The ISMR Query Tool. *Computers & Geosciences*, *104*, 125–134.

Vazquez-Álvarez, A. J., Tubío-Pardavila, R., Gonzalez-Muiño, A., Aguado-Agelet, F., Arias-Acuna, M., & Vilan-Vilán, J. A. (2012). Design of a polarization diversity system for ground stations of CubeSat space systems. *IEEE Antennas and Wireless Propagation Letters*, *11*, 917–920.

Verkhoglyadova, O., Meng, X., Mannucci, A. J., Shim, J.-S., & McGranaghan, R. (2020). Evaluation of total electron content prediction using three ionosphere-thermosphere models. *Space Weather*, *18*(9), 1–19.

Viall, N. M., & Borovsky, J. E. (2020). Nine outstanding questions of solar wind physics. *Journal of Geophysical Research: Space Physics*, *125*(7), 1–35.

Vlasov, A., Kauristie, K., van de Kamp, M., Luntama, J.-P., & Pogoreltsev, A. (2011). A study of traveling ionospheric disturbances and atmospheric gravity waves using EISCAT Svalbard radar IPY-data. *Annales Geophysicae*, *29*(11), 2101–2116.

Waldock, J. A., & Jones, T. B. (1986). HF Doppler observations of medium-scale travelling ionospheric disturbances at mid-latitudes. *Journal of Atmospheric and Terrestrial Physics*, *48*(3), 245–260.

Wanliss, J. A., & Showalter, K. M. (2006). High-resolution global storm index: Dst versus sym-h. *Journal of Geophysical Research: Space Physics*, *111*(A2), 1–10.

WDC KYOTO. (2001). *Provisional Auroral Electrojet (AE) indices. Data Book no 26* (tech. rep.). World Data Center for Geomagnetism, Kyoto.
available at: https://wdc.kugi.kyoto-u.ac.jp/wdc/publi.html.

WDC KYOTO. (2009). *Mid-latitude geomagnetic indices ASY and SYM for 2009 (provisional)* (tech. rep.). World Data Center for Geomagnetism, Kyoto.
available at: https://wdc.kugi.kyoto-u.ac.jp/aeasy/asy.pdf.

Welling, D. T., Ngwira, C. M., Opgenoorth, H., Haiducek, J. D., Savani, N. P., Morley, S. K., Cid, C., Weigel, R., Weygand, J. M., Woodroffe, J. R., Singer, H., Rosenqvist, L., & Liemohn, M. (2018). Recommendations for next-generation ground magnetic perturbation validation. *Space Weather*, *16*(12), 1912–1920.

Wertz, J. R., & Larson, W. J. (1999). *Space Mission analysis and design* (3rd ed.). Kluwer Academic Publishers.

Wilder, F. D., Crowley, G., Anderson, B. J., & Richmond, A. D. (2012). Intense dayside Joule heating during the 5 April 2010 geomagnetic storm recovery phase observed by AMIE and AMPERE. *Journal of Geophysical Research: Space Physics*, *117*(A5), A05207.

Wright, P. A., Quegan, S., Wheadon, N. S., & Hall, C. D. (2003). Faraday rotation effects on L-band spaceborne SAR data. *IEEE Transactions on Geoscience and Remote Sensing*, *41*(12), 2735–2744.

Xiong, C., Lühr, H., Wang, H., & Johnsen, M. G. (2014). Determining the boundaries of the auroral oval from CHAMP field-aligned current signatures - Part 1. *Annales Geophysicae*, *32*(6), 609–622.

Yamauchi, M., Sergienko, T., Enell, C.-F., Schillings, A., Slapak, R., Johnsen, M. G., Tjulin, A., & Nilsson, H. (2018). Ionospheric Response Observed by EISCAT During the 6–8 September 2017 Space Weather Event: Overview. *Space Weather*, *16*(9), 1437–1450.

Yeh, K. C., & H., L. C. (1982). Radio wave scintillations in the ionosphere. *Proceeding of the IEEE*, *70*(4), 324–360.

Zakharenkova, I., Astafyeva, E., & Cherniak, I. (2016). GPS & GLONASS observations of large-scale traveling ionospheric disturbances during the 2015 St. Patrick's Day storm. *Journal of Geophysical Research: Space Physics*, *121*(12), 12, 138–12, 156.

Zhang, J., Richardson, G., Webb, D. F., Gopalswamy, N., Huttunen, E., Kasper, J. C., Nitta, N. V., Poomvises, W., Thompson, B. J., Wu, C.-C., Yashiro, S., & Zhukov, A. N. (2007). Solar and interplanetary sources of major geomagnetic storms (Dst $\leq$ -100 nT) during 1996-2005. *Journal of Geophysical Research*, 1–19.

Zhang, S., Coster, A., Erickson, P., Goncharenko, L., Rideout, W., & Vierinen, J. (2019). Traveling ionospheric disturbances and ionospheric perturbations associated with solar flares in September 2017. *Journal of Geophysical Research: Space Physics*, *124*, 5894–5917.

Zhang, S., Erickson, P. J., Coster, A. J., Rideout, W., Vierinen, J., Jonah, O., & Goncharenko, L. P. (2019). Subauroral and polar traveling ionospheric disturbances during the 7–9 September 2017 storms. *Space Weather*, *17*(12), 1748–1764.

Zheng, Y., Li, X., & Wang, X. (2019). Solar flare prediction with the hybrid deep convolutional neural network. *The Astrophysical Journal*, *885*(73), 1–14.

Zhou, Z. (2012). *Ensemble methods: Foundations and algorithms* (1st). Chapman & Hall/CRC Machine Learning & Pattern Recognition Series.

APPENDIX

A List of Publications

A.1 Journal publications

Borries, C. ; **Ferreira, A. A.**; Nikyel, G. ; Borges, R. A . A new index for statistical analyses and prediction of traveling ionospheric disturbances. Journal of Atmospheric and Solar-Terrestrial Physics, v. 247, p. 1-13, 2023, doi:10.1016/j.jastp.2023.106069.

Ferreira, A. A.; Borges, R. A. ; Reis, L. R. ; Borries, C. ; Vasylyev, D. ; . Investigation of Ionospheric Efects in the Planning of the AlfaCrux UHF Satellite Communication System. IEEE ACCESS, v. 10, p. 65744-65759, 2022, doi:10.1109/ACCESS.2022.3183152.

Ferreira, A. A.; Borries, C.; Xiong, C.; Borges, R. A.; Mielich, J.; Kouba, D. . Identification of potential precursors for the occurrence of Large-Scale Traveling Ionospheric Disturbances in a case study during September 2017. Journal of Space Weather and Space Climate, v. 10, p. 1/10-17, 2020, doi:10.1051/swsc/2020029.

Dos Santos Prol, F. ; Hoque, M. ; **Ferreira, A. A.** . Plasmasphere and Topside Ionosphere Reconstruction using METOP Satellite Data during Geomagnetic Storms. Journal of Space Weather and Space Climate, v. 11, p. 5, 2020, doi:10.1051/swsc/2020076.

Borries, C.; Wilken, V.; Jacobsen, K. S.; García-Rigo, A.; Dziak J. B.; Kervalishvili, G.; Jakowski, N.; Tsagouri, I.; Hernández-Pajares, M.; **Ferreira, A. A.**; Hoque, M. M. Assessment of the capabilities and applicability of ionospheric perturbation indices provided in Europe. Advances in Space Research, v. 66, p. 546-562, 2020, doi:10.1016/j.asr.2020.04.013.

A.2 Conference publications

A.2.1 Full-length papers

Ferreira, A. A.; Borges, R. A.; Performance Analysis of Distinct Feed-forward Neural Networks Structures on the AE Index Prediction. In: 2021 IEEE Aerospace Conference (50100), Big Sky, MT, USA, 2021, pp. 1-7, doi:10.1109/AERO50100.2021.9438504.

A.2.2 Abstracts

Ferreira, A. A.; Borries, C.; Borges, R. A . Investigation on the prediction of Large Scale Traveling Ionospheric Disturbances over Europe. In: Proceedings of the International Workshop on GNSS Ionosphere, Neustrelitz, 2022.

Ferreira, A. A.; Borries, C.; Borges, R. A . Artificial neural network based prediction of Large Scale Travelling Ionospheric Disturbances. In: Proceedings of the 1st Workshop on Data Science for GNSS Remote Sensing (D4G), Potsdam, 2022.

Borries, C.; **Ferreira, A. A.**; Borges, R. A . Statistical analysis and predictability of large scale travelling ionospheric disturbances over Europe. In: Proceedings of the SCOSTEP 15th Quadrennial Solar-Terrestrial Physics Symposium (STP-15), Online, 2022.

Borries, C.; **Ferreira, A. A.** . The diversity of ionospheric storm disturbances caused by strong perturbations in the solar wind. In: Proceedings of the 43rd COSPAR Scientific Assembly, 2021, Sydney, 2021.

Borries, C.; **Ferreira, A. A.** ; Xiong, C.; Borges, R. A.; Mielich, J.; Kouba, D. . Properties and Generation of Large Scale Travelling Ionospheric Disturbances during 8 September 2017. In: Proceedings of EGU General Assembly, Geophysical Research Abstracts, Online, 2020.

Ferreira, A. A.; Borries, C.; Borges, R. A . Large-Scale Travelling Ionospheric Disturbances occurrence during the Space Weather Events of September 7-8th, 2017. In: Proceedings of the EGU General Assembly, Geophysical Research Abstracts, Viena, 2019.

Ferreira, A. A.; Borries, C.; Borges, R. A . Analysis of precursors for Large-Scale Travelling Ionospheric Disturbances. In: Proceedings of the International Workshop on GNSS Ionosphere, 2019.

B List of Geomagnetic Storms 1

This Appendix presents the list of the geomagnetic storms from which the LSTIDs' features are extracted (see Section 2.1.4).

Table B.1 – List of the geomagnetic storms from which the LSTIDs amplitudes are extracted (Section 2.1.4).

id	Sudden Storm Commencement (UT)	time of minimum symH (UT)	minimum symH (nT)
0	2015-Jan-02 10:20:00	2015-Jan-03 01:40:00	-55
1	2015-Jan-07 07:20:00	2015-Jan-07 11:00:00	-134
2	2015-Jan-25 21:35:00	2015-Jan-26 10:25:00	-53
3	2015-Feb-16 23:55:00	2015-Feb-17 23:55:00	-70
4	2015-Feb-23 03:45:00	2015-Feb-24 03:30:00	-75
5	2015-Feb-28 06:30:00	2015-Mar-01 06:25:00	-53
6	2015-Mar-17 05:10:00	2015-Mar-17 09:35:00	-99
7	2015-Apr-09 21:50:00	2015-Apr-10 04:35:00	-70
8	2015-May-10 03:55:00	2015-May-11 03:55:00	-56
9	2015-May-18 10:15:00	2015-May-19 02:55:00	-64
10	2015-Jun-07 13:45:00	2015-Jun-08 07:45:00	-104
11	2015-Jun-22 18:35:00	2015-Jun-23 04:25:00	-207
12	2015-Jun-27 06:55:00	2015-Jun-28 06:25:00	-62
13	2015-Jul-04 16:00:00	2015-Jul-05 04:50:00	-86
14	2015-Jul-13 01:40:00	2015-Jul-13 10:55:00	-71
15	2015-Jul-22 14:20:00	2015-Jul-23 07:30:00	-83
16	2015-Jul-30 16:10:00	2015-Jul-31 03:00:00	-52
17	2015-Aug-15 08:35:00	2015-Aug-15 12:30:00	-74
18	2015-Aug-23 02:40:00	2015-Aug-23 08:30:00	-59
19	2015-Aug-25 16:10:00	2015-Aug-26 09:25:00	-56
20	2015-Sep-07 01:45:00	2015-Sep-08 01:45:00	-90
21	2015-Sep-20 02:30:00	2015-Sep-20 11:05:00	-84
22	2015-Oct-03 13:40:00	2015-Oct-07 09:15:00	-87
23	2015-Nov-03 07:40:00	2015-Nov-03 12:50:00	-59
24	2015-Nov-06 18:40:00	2015-Nov-07 06:05:00	-106
25	2015-Dec-14 15:10:00	2015-Dec-14 19:05:00	-56
26	2015-Dec-19 23:05:00	2015-Dec-20 22:50:00	-169
27	2015-Dec-31 00:55:00	2015-Dec-31 14:10:00	-54
28	2016-Jan-20 03:10:00	2016-Jan-20 17:05:00	-95
29	2016-Jan-31 08:40:00	2016-Feb-03 02:50:00	-59

id	Sudden Storm Commencement (UT)	time of minimum symH (UT)	minimum symH (nT)
30	2016-Feb-16 08:30:00	2016-Feb-16 19:40:00	-56
31	2016-Mar-06 10:25:00	2016-Mar-06 21:20:00	-109
32	2016-Mar-14 18:45:00	2016-Mar-15 07:20:00	-62
33	2016-Apr-02 14:35:00	2016-Apr-02 22:50:00	-65
34	2016-Apr-07 17:15:00	2016-Apr-08 00:25:00	-67
35	2016-Apr-12 17:00:00	2016-Apr-13 01:10:00	-69
36	2016-May-01 10:55:00	2016-May-02 03:15:00	-55
37	2016-May-08 01:00:00	2016-May-08 08:15:00	-103
38	2016-Jun-05 07:50:00	2016-Jun-06 02:30:00	-52
39	2016-Jul-24 22:20:00	2016-Jul-25 17:15:00	-51
40	2016-Aug-02 20:55:00	2016-Aug-03 06:45:00	-62
41	2016-Aug-23 11:30:00	2016-Aug-23 21:10:00	-82
42	2016-Aug-31 10:25:00	2016-Sep-01 09:30:00	-57
43	2016-Oct-03 17:35:00	2016-Oct-04 04:15:00	-56
44	2016-Oct-13 02:05:00	2016-Oct-13 23:45:00	-114
45	2016-Oct-24 19:05:00	2016-Oct-25 08:00:00	-51
46	2016-Nov-09 21:10:00	2016-Nov-10 15:20:00	-55
47	2016-Nov-24 08:50:00	2016-Nov-25 06:30:00	-52
48	2016-Dec-21 09:20:00	2016-Dec-21 15:40:00	-52
49	2017-Mar-01 07:10:00	2017-Mar-01 22:15:00	-73
50	2017-Apr-21 16:20:00	2017-Apr-22 04:25:00	-51
51	2017-May-27 21:30:00	2017-May-28 07:10:00	-141
52	2017-Sep-07 01:35:00	2017-Sep-08 01:05:00	-144
53	2017-Sep-12 20:10:00	2017-Sep-13 00:10:00	-64
54	2017-Sep-27 05:30:00	2017-Sep-27 22:15:00	-52
55	2017-Oct-13 09:20:00	2017-Oct-13 19:25:00	-59
56	2017-Nov-07 04:30:00	2017-Nov-07 11:25:00	-52
57	2017-Nov-20 17:05:00	2017-Nov-21 06:50:00	-60
58	2018-Feb-26 18:45:00	2018-Feb-27 13:00:00	-58
59	2018-Mar-17 22:45:00	2018-Mar-18 21:40:00	-52
60	2018-Apr-20 00:25:00	2018-Apr-20 06:05:00	-55

id	Sudden Storm Commencement (UT)	time of minimum symH (UT)	minimum symH (nT)
61	2018-May-05 14:20:00	2018-May-06 02:30:00	-66
62	2018-Aug-25 08:30:00	2018-Aug-26 07:10:00	-205
63	2018-Sep-10 10:35:00	2018-Sep-10 23:10:00	-57
64	2018-Oct-07 10:40:00	2018-Oct-07 19:55:00	-55
65	2018-Nov-04 07:45:00	2018-Nov-05 06:00:00	-65

C List of Geomagnetic Storms 2

This Appendix presents the list of the geomagnetic storms used to perform the cross correlation studies presented in Section 3.2.

Table C.1 – List of the geomagnetic storm events used on the statistical analysis presented in Section 3.2.

id	Date	minimum Dst (nT)	id	Date	minimum Dst (nT)
1	31-Jan-2001	-45.00	31	24-Aug-2005	-216.00
2	27-Mar-2001	-51.00	32	09-Sep-2005	-38.00
3	31-Mar-2001	-387.00	33	11-Sep-2005	-147.00
4	08-Apr-2001	-59.00	34	07-Aug-2006	-43.00
5	18-Apr-2001	-114.00	35	14-Dec-2006	-41.00
6	18-Jun-2001	-61.00	36	17-Dec-2007	-36.00
7	17-Aug-2001	-105.00	37	26-Sep-2011	-101.00
8	25-Sep-2001	-53.00	38	25-Oct-2011	-132.00
9	11-Oct-2001	-70.00	39	09-Mar-2012	-131.00
10	05-Nov-2001	-55.00	40	24-Apr-2012	-108.00
11	06-Nov-2001	-292.00	41	15-Jul-2012	-127.00
12	24-Nov-2001	-221.00	42	101-Oct-2012	-119.00
13	17-Apr-2002	-98.00	43	17-Mar-2013	-132.00
14	11-May-2002	-110.00	44	01-Jun-2013	-119.00
15	23-May-2002	-109.00	45	19-Feb-2014	-112.00
16	01-Aug-2002	-51.00	46	07-Jan-2015	-99.00
17	21-Nov-2002	-128.00	47	17-Mar-2015	-223.00
18	24-Oct-2003	-44.00	48	07-Oct-2015	-124.00
19	29-Oct-2003	-350.00	49	03-Nov-2015	-55.00
20	30-Oct-2003	-383.00	50	20-Dec-2015	-155.00
21	04-Nov-2003	-69.00	51	02-Apr-2016	-56.00
22	20-Nov-2003	-422.00	52	13-Oct-2016	-104.00
23	22-Jan-2004	-149.00	53	01-Mar-2017	-61.00
24	26-Jul-2004	-197.00	54	27-Mar-2017	-70.00
25	07-Nov-2004	-373.00	55	28-May-2017	-125.00
26	12-Nov-2004	-115.00	56	16-Jul-2017	-72.00
27	05-Dec-2004	-18.00	57	31-Aug-2017	-51.00
28	21-Dec-2004	-29.00	58	08-Sep-2017	-122.00
29	21-Jan-2005	-99.00	59	14-Sep-2017	-33.00
30	15-May-2005	-263.00	60	07-Nov-2017	-71.00